Interfacial Tuning of Multifunctional Composites and Bio-Inspired Materials with Atomic Layer Deposition

by

Robin E. Rodríguez

A dissertation submitted in partial fulfillment
of the requirements for the degree of
Doctor of Philosophy
(Mechanical Engineering)
in the University of Michigan
2021

Doctoral Committee:

Associate Professor Neil P. Dasgupta, Chair
Research Associate Professor Mihaela Banu
Professor Henry A. Sodano
Professor M. D. Thouless

Robin E. Rodríguez

robinrod@umich.edu

ORCID iD: 0000-0003-0182-0601

This dissertation is dedicated to my parents. Thank you for being unwavering pillars of support, and for always believing in my capabilities and in encouraging me every step along the way, even throughout the most difficult of times. The work and dedication you put into improving the lives of the disadvantaged communities of Puerto Rico inspire me every day. Your influence and vision were my motivation to pursue a career in science and engineering that not only contributes to scientific advancements, but also to societal improvements.

ACKNOWLEDGEMENTS

I would like to begin by expressing my sincere gratitude to my advisor Professor Neil P. Dasgupta. Thank you for the amount of time and support you dedicate to your students. Your commitment, not only to the pursuit of scientific knowledge and advancements, but also to the development and professional success of your students are fantastic qualities of a teacher and mentor. I am grateful to you for your guidance, mentorship, and patience throughout the endeavors of this journey that have led to both my professional and personal growth.

I would also like to thank my committee members for their knowledge, insight, and expertise. In particular, Professor Michael Thouless and Professor Mihaela Banu for meeting with me on a weekly basis to discuss and analyze the experimental results and to analyze and understand the mechanisms and phenomena behind the data.

Thank you to the many lab members from our group - Eric Kazyak, Yuxin Chen, Tae Cho, Sneha Agarwal, Will LePage, Andrew Gayle, Ashley Bielinski, Orlando Trejo, Adrian Sanchez, Jing Wang, Julia Lenef, and Kevin Wood - for having helped and for having provided insight on many aspects of my work. I would also like to thank members from other lab groups - in particular Mohammad Ravandi and Tae Hwa Lee - whom have collaborated and patiently trained me in new techniques outside the normal scope of our group.

I would also like to thank the undergraduate students from the University of Michigan - Tae Cho, Xhulja Biraku, and Claire Huang - whom assisted in this research. I enjoyed the opportunity to mentor these brilliant students. It was a joy for me when Tae Cho announced he would be staying in our group as a Ph.D. student and I wish him success.

Thanks to all of my friends, new and old, for their friendship and for being a fundamental part of my support group throughout this process. I would also like to thank my best friend and wonderful girlfriend Allison for her love, support, and incredible patience in having endured a long-distance relationship for almost seven years. I am beyond excited to finally begin our lives together.

Lastly, I would like to acknowledge the several funding sources that have supported the work presented in this dissertation. The Rackham Graduate fellowship provided by the University of Michigan provided funding for two years of my Ph.D. studies. The works from

Chapters 4 and Chapters 5 were supported by the Air Force Office of Scientific Research (AFOSR) under Grant FA9550-16-1-0313. This material is based upon work supported by the National Science Foundation under Grant No. 1751590. I would also like to acknowledge the financial support of the University of Michigan College of Engineering and NSF Grant DMR-9871177 and technical support from the Michigan Center for Materials Characterization and the Lurie Nanofabrication Facility.

I would like to acknowledge the support from the University of Michigan–Shanghai Jiao Tong University Collaboration on Nanotechnology for Energy and Biomedical Applications. The work from Chapter 6 was possible thanks to the collaborations with Professor Tao Deng, Professor Wen Shang, and Shun An from the State Key Laboratory of Metal Matrix Composites, within the School of Materials Science and Engineering of Shanghai Jiao Tong University. The work was partially supported by the Air Force Office of Scientific Research (AFOSR) under Grant FA9550-16-1-0313. Collaborator Dr. Eric Kazyak acknowledges that this material is based upon work supported by a National Science Foundation Graduate Research Fellowship under Grant DGE 1256260. This research used resources of the University of Michigan Electron Microbeam Analysis Laboratory, including instruments supported by National Science Foundation Grants DMR-0320740 and DMR-0420785.

Table of Contents

List of Figures

Figure

List of Tables

Table

List of Abbreviations

1-D one-dimensional

3-D three-dimensional

ALD atomic layer deposition

AZO aluminum-doped zinc oxide

CMC ceramic-matrix composite

CNT carbon nanotube

CVD chemical vapor deposition

DEZ diethylzinc

DI deionized

EDS energy dispersive x-ray spectroscopy

FIB focused ion beam

FDTD finite-difference time-domain

FEA finite element analysis

FRC fiber-reinforced composite

IR infrared

MLD molecular-layer deposition

MWCNT multi-walled carbon nanotube

PMC polymer-matrix composite

PMMA polymethyl methacrylate

PV photovoltaic

PVD physical vapor deposition

SEM scanning electron microscopy

SERS surface-enhanced Raman spectroscopy

SiC silicon carbide

TDMAT tetrakis(dimethylamido)titanium

TOF turnover frequency

UV ultraviolet

VARTM vacuum-assisted resin transfer molding

XPS x-ray photoelectron spectroscopy

XRD x-ray diffraction

Abstract

Surface and interfacial modification processes have the potential to address several of the performance limitations in the fields of structural materials, energy conversion, and energy storage, among others. Hence, there has been a need to integrate reliable surface and interfacial modification techniques into materials processing. In this dissertation, atomic layer deposition (ALD) was utilized to impart multifunctionality onto composites and biotemplate surfaces and demonstrate its potential to enable the development of transformative materials.

Accurate temperature monitoring and control of temperature distribution is necessary in order to obtain ideal and uniform ALD growth. The work in Chapter 3 assessed how inaccuracies in temperature monitoring and temperature control of the reactor can lead to nonuniform deposition. The implementation of an improved heater and thermal monitoring design drastically improved uniform ALD thickness across the reaction chamber. This study highlighted the need of properly designed ALD systems that can control and monitor the temperature of the reactor with accuracy and precision. This is especially important as new ALD precursors emerge that have narrower temperature windows for ideal deposition conditions.

To explore the capabilities of ALD to impart multifunctional properties into structural composites, we first studied the effects these coatings have on their interfacial properties, which directly affect the bulk strength and toughness of the composite. In Chapter 4, we utilized ALD as a method to conformally coat structural fibers with various materials and studied the impact of these interlayers on their mechanical adhesion to polymer matrix

materials. It was observed that the mechanical force required for debonding of the polymer droplet from the coated fiber surfaces depended on the composition and thickness of the coating. The ability to tune the interfacial properties presents an opportunity to develop engineered structural composite materials designed with specific macroscopic mechanical properties. Additionally, ALD of ZnO was demonstrated to prevent fiber degradation from ultraviolet radiation and high-temperature thermal treatments, demonstrating a pathway towards multifunctional composite interphase engineering by ALD.

Expanding upon this work, ALD coatings were utilized to impart multifunctionality. Imparting electrical conductivity into polymer-matrix composites (PMCs) is an important step in enabling multifunctionality, while maintaining mechanical stiffness and strength. In the work presented in Chapter 5, electrically conductive PMCs were fabricated by conformally coating Kevlar® 49 woven fabrics with aluminum-doped zinc oxide using ALD. This work demonstrates a new pathway for scalable and tunable incorporation of electrical conductivity into fiber-reinforced composites without significantly changing their density or load-bearing capabilities.

Lastly, the versatility of ALD was demonstrated in Chapter 6 by imparting multifunctional properties onto *Morpho* sulkowskyi butterfly wings. The wings contain high aspect ratio nanostructures, which make them ideal templates for applications in solar energy and photocatalysis. This study demonstrated the ability to precisely tune the natural structural coloration while also integrating multifunctionality by imparting photocatalytic activity onto fully intact *Morpho* wings. These structurally colored photocatalysts exhibited an optimal coating thickness to maximize photocatalytic activity, which was attributed to trade-offs between light absorption and catalytic quantum yield with increasing coating thickness. These multifunctional photocatalysts present a new approach to integrating solar energy harvesting into visually attractive surfaces that can be integrated into building facades or other macroscopic structures to impart aesthetic appeal.

In summary, ALD has been demonstrated as a method to impart multifunctional prop-

erties onto a variety of materials that require precise control of thickness and uniformity.

Chapter 1

Introduction

1.1 Surfaces and Interfaces in Materials Engineering

The combination of two or more materials with different but synergistic properties can have significant impacts in materials design across a multitude of applications. For example, batteries[1,2] combine multiple materials with different electronic and ionically conductive properties that function together to store energy. Another example is that of structural composite materials,[3,4] which incorporate reinforcements and fillers into a matrix material composed of polymers, ceramics, or metals to obtain material properties not previously achievable in the individual materials.

While the examples presented above are typically used for very different applications, they both have one thing in common: their performance highly depend on the surface and interfacial properties of their material constituents. In some cases, the performance limitations of materials can occur at surfaces and interfaces. Often, these limitations can be addressed by intentionally modifying the surface and interfacial chemistry of the materials. For example, one might want to tailor interfacial adhesion,[5] surface wetting,[6,7] and electronic properties,[8,9] among others, in order to obtain a desired function. One method to tailor these properties is through the application of thin coatings. Coating methods with precise compositional control and thickness resolution are thus critical in order to obtain the desired properties.

In this work we utilize ALD as a method to tune surface and interfacial properties of composite materials and biological substrates, with the overall intention of imparting new multifunctional capabilities. Details about ALD and the motivation behind multifunctional materials are discussed in Sections 2.1 and 1.2, respectively.

1.2 Multifunctional Materials

Often, design of materials tends to focus on improving a specific physical property for a given application. This is a lost opportunity to design materials that can achieved this targeted property, while also imparting additional useful functionality. Around the early 2000's, DARPA (The Defense Advanced Research Projects Agency) introduced the Synthetic Multifunctional Materials program. This program aimed to transform "parasitic" structural materials, which occupy mass and volume but do not contribute to additional system performance, by imparting an additional non-structural, system-enhancing functionality. These materials are often referred to as multifunctional materials, and have subsequently represented a significant topic in the field of materials science.

Materials with transformational levels of performance can be obtained by designing them in a manner that considers their potential for multifunctionality. For example, structural batteries[10,11] can have significant implications for vehicle systems, as they could incorporate the energy storage capabilities into the interior panels of a vehicle, reducing the volume and weight taken up by traditional battery packs. Other examples of multifunctional materials include self-healing materials,[12–14] wearable electronics,[15–17] damage-detecting materials,[18,19] and electromagnetic shielding properties.[20–22]

Integration of additional material components is often needed in order to bring about these system modifications. Multifunctional integration can occur at various spatial levels, including the macro, micro, meso, and/or nanoscale. The most common methods to incorporate multifunctional properties are through macroscale material integration.[23] While

these methods often benefit from simplicity in their processing, they usually come at the expense of the structural integrity of the final product. Furthermore, they can significantly increase the weight of the material, which is often not desired. Thus, over the past several decades, research in the area of multifunctional materials has focused on imparting, tuning, and tailoring non-structural properties through microscale and nanoscale material integration.[24]

Much of this research has been performed on fiber composites, textiles, foams, and other porous structures.[25] One common challenge present among all of these material systems is the incorporation of additives or coatings without significantly affecting the mechanical properties or structural integrity of the material being modified. Furthermore, nonuniform distribution of additives or inconsistent thickness control of the coatings can result in inhomogenous properties. Thus, there has been an increasing need for conformal and uniform distribution of these components to obtain precise desired properties.

A thorough understanding of the material properties and interactions between the main constituents and additives is necessary to tailor and design specific performance metrics. By understanding the process-structure-property relationships associated with the fillers and/or coatings in these systems, multifunctional materials with the desired optimal properties can be rationally designed. Lastly, multifunctional composites can provide significant contributions to energy savings, reduction of emissions, and/or more efficient use of materials. In Chapter 5, a method to incorporate interfacial coatings into composite materials and impart multifunctionality via ALD is presented. A brief introduction to the principles of fiber-reinforced composites can be found in Section 2.2.

1.3 Biological Nanostructures

Many engineered nanostructures have drawn inspiration from nanoscale architectures found in nature, which have been optimized to serve specific functions over the course

of billions of years of evolution.[26–29] Many of the nanoarchitectures found in these biotemplates have demonstrated technological potential applications in areas including advanced optoelectronic devices,[30,31] sensors,[32] catalysis,[33,34] energy conversion and storage,,[35–38] and bactericidal and antifouling applications.[39] Several attempts have been made to mimic or replicate biological nanostructures artificially. The two main approaches to accomplish this can be categorized as biomimicry and biotemplating. Biomimicry attempts to artificially replicate the natural material architecture, using a combination of top-down and bottom-up processing for patterning (often with multiple lithography and/or self-assembly steps, in combination with etching and deposition processes).[40–42] These methods present geometric challenges, particularly when attempting to replicate complex three-dimensional (3D) nanostructures composed of heterogeneous material systems. Thus, artificial biomimetic materials fall short of the structural complexity and precision found in nature. Additionally, many of these fabrication processes are generally energy-intensive and require costly cleanroom techniques that produce large material waste streams. This limits the scalability and environmental sustainability of biomimetic nanomanufacturing.

In contrast, biotemplating utilizes existing structures found in nature as a scaffold for bottom-up additive manufacturing.[42] This allows for efficient use of raw materials and reduces energy and cost inputs. The structural information and embodied manufacturing energy are provided by nature, and the templates are compostable. Existing natural waste streams of biological materials, including insect wings, feathers, and shells, possess unique optical properties and high-aspect-ratio surfaces. This presents an opportunity for a wide range of applications that benefit from nanostructuring.

However, moving beyond simple replication of the geometry requires integration of functional materials onto biological surfaces. This can present a challenge for traditional coating processes such as sol–gel, physical vapor deposition, and chemical vapor deposition, which are limited in their ability to deposit conformal films on complex 3D surfaces with high aspect ratios that may contain mixtures of convex and concave surface features.

In Chapter 6, a method is presented that integrates functional materials via ALD, enabling deposition of conformal thin-films onto 3-D surfaces while precisely maintaining the structural form of the underlying template.

1.4 Outline

Chapter 2 provides a summary of the background and principles related to processes, materials, and devices presented throughout this work. It briefly touches upon the basic concepts of ALD, continuous fiber-reinforced composites, and photocatalysis.

Chapter 3 presents a systematic study of the temperature dependence of ALD growth. We demonstrate that uniform temperature control and accurate temperature monitoring across the reactor become increasingly important as new ALD processes with stringent requirements in temperature control emerge. To address this need, we implemented an improved heater design, along with accurate and precise thermal monitoring to improve uniform ALD thickness across the reaction chamber. The lessons learned from this study were utilized to build a larger ALD reactor in our laboratory that is capable of coating larger substrates such as woven fabrics, which enabled the work presented in Chapter 5.

Chapter 4 explores the effects that ALD coatings have on the interfacial mechanical properties between structural fibers and polymers. The microbond test method, which is a modified form of the fiber pullout test, was used to quantify the interfacial mechanical properties between the polymer matrix and ALD-coated structural fibers. Two fiber-polymer material systems were used in this study: Kevlar®/PMMA and carbon fiber/epoxy. Furthermore, ZnO coatings were shown to prevent damage from high-temperature and ultraviolet (UV) light exposure, demonstrating other potential benefits of the coatings.

The potential of ALD coatings to impart multifunctionality is further explored in Chapter 5. This work demonstrates that electrically conductive properties can be imparted to PMCs that are normally electrically insulating through interfacial modification by ALD.

The interfacial coating material used in this study was AZO. The influence of the coating thickness on the electrical properties through individual fibers, tows, and fabrics was studied. The degree of percolation through a fiber network depended on the number of bridged connections. Consequently, the number of bridged connections increased with AZO thickness. Tensile tests were performed to evaluate the coupled mechanical properties and electrical response of the composite. The electrical response as a function of strain was observed to vary with the thickness of the coating. Lastly, a thin-film fracture mechanics model was considered to explain the thickness-dependent behavior.

Chapter 6 demonstrates a bottom-up biotemplating approach by coating *Morpho* butterfly wings with multifunctional ALD coatings. It was demonstrated that low-temperature ALD can impart photocatalytic properties onto *Morpho* sulkowskyi butterfly wings by depositing nanocrystalline ZnO. The hierarchical nanostructures that naturally occur in *Morpho* sulkowskyi wings produce structural color, which can be tuned by precisely controlling the coating thickness. The photocatalytic performance was optimized by controlling the thickness of the ZnO coating. Optical spectroscopy and finite-difference time-domain numerical modeling were used to elucidate the competing effects between light absorption and catalytic quantum yield as a function of coating thickness. Additionally, this study showed we can maintain the macroscopic structure of a biological template over large areas, which could enable the expanded use of biological materials in multifunctional applications.

Chapter 7 concludes the work presented in this dissertation and presents directions for future work.

1.5 Individual and Group Research Statement

The work presented in this research would not have been possible without the collaborative efforts, guidance, and expertise from others. The contributions from the collaborators are

presented below.

The work in Chapter 3 spurred from a collaboration with engineers from Watlow Electric Manufacturing Co. to develop heating and temperature sensing solutions for precise control and uniformity of temperature. The 3-D computer-aided design of the reactor and finite element analysis (FEA) were implemented by Robin E. Rodríguez. The ALD of TiO_2 on Si substrates was performed by Robin E. Rodríguez. Spectroscopic ellipsometry data were measured by Ashley R. Bielinski. Infrared (IR) imaging was performed by William S. LePage. A systematic design of experiments (DOE) method was implemented by Robin E. Rodríguez, with guidance from Watlow, Co. engineers Patrick Margavio and Peter Hwang. The new reactor was built and assembled by Robin E. Rodríguez. Neil P. Dasgupta provided guidance and support.

Chapter 4 was adapted from Rodríguez, et al. 2020. Robin E. Rodríguez developed the procedure for coating single fibers by ALD. Robin E. Rodríguez and Tae H. Cho developed a method to add PMMA microdroplets onto single Kevlar® fibers. Robin E. Rodríguez and Mohammad Ravandi developed the method to add epoxy microdroplets onto single carbon fibers. The microvise design and assembly were designed and built by Tae H. Cho, Mohammad Ravandi, and Robin E. Rodríguez. The microbond test setup and procedure was developed by Mohammad Ravandi and optimized by Robin E. Rodríguez. SEM and EDS mapping were performed by Robin E. Rodríguez. Cross-sectional SEM images were obtained by Eric Kazyak. William S. LePage helped to produce the box plot figures and provided general feedback on the microbond method. Mihaela Banu, M. D. Thouless and Neil P. Dasgupta assisted with writing and revising the conference proceedings manuscript and provided guidance and support.

Chapter 5 was adapted from a manuscript that has been submitted for publication. The procedure for preparing and coating single fibers, single tows, and woven Kevlar® fabrics by ALD was developed by Robin E. Rodríguez. Tae H. Cho assisted with some of these coating procedures. Tae H. Cho and Julia Lenef helped perform spectroscopic ellipsometry

measurements. William S. Lepage designed and built the four-point probe assembly. The methods for measuring the electrical properties and calculating the effective electrical resistivity of the samples was developed by Robin E. Rodríguez. Tae Hwa Lee implemented and trained Robin E. Rodríguez on the vacuum-assisted resin transfer molding (VARTM) method for fiber-reinforced composites (FRCs) manufacturing, which was later modified by Robin E. Rodríguez to fabricate electrically conductive FRCs. Yuxin Chen helped to prepare fabrics that were used for VARTM. Robin E. Rodríguez developed the methods for sample preparation and testing of the electrically conductive composites, with input and feeback from Tae Hwa Lee. Custom made grips for tensile tests were designed and built by Robin E. Rodríguez, with input from Andrea Poli. Claire Huang helped continue sample preparation and testing. Erik Kazyak took the SEM-FIB images presented. M. D. Thouless provided insight into the fracture mechanisms of the ALD coatings. Mihaela Banu, M. D. Thouless, and Neil P. Dasgupta assisted with writing and revising the manuscript and provided guidance and support.

Chapter 6 was adapted from Rodríguez, et al. (2018). Robin E. Rodríguez, Sneha P. Agarwal, and Debashree Das developed the methods for preparing and coating the *Morpho* butterfly substrates by ALD. Debashree Das and Sneha P. Agarwal developed the dye-degradation process and aliquot absorption intensity measurements (using a UV-vis spectrophotometer), with modifications from Robin E. Rodríguez. Robin E. Rodríguez and Sneha P. Agarwal acquired the data for this work. Robin E. Rodríguez interpreted the results and identified the underlying mechanisms of the observed behavior. The finite-difference time-domain (FDTD) model and simulations were developed by Shun An. Wen Shang, Tao Deng, and Neil P. Dasgupta assisted with writing and revising the manuscript and provided guidance and support.

Chapter 2

Background

2.1 Basics of Atomic Layer Deposition

Recent technological advances have led to the successful commercialization of nanotechnology in the semiconductor industry, and have enabled advances in a range of applications including electronics, medical devices, energy conversion, and energy storage. Advances in nanofabrication have allowed these devices to incorporate features with reduced dimensions and increasingly efficient performance. However, traditional nanofabrication techniques have presented several limitations as devices are pushed to smaller scales. Many industrially-relevant nanofabrication processes lack consistency and uniformity at the single nanometer and sub-nanometer lengths scales, which can lead to inhomogeneous material addition and/or subtraction. Furthermore, as advanced materials and device engineering has pushed to increasingly complex three-dimensional architectures, the ability to conformally deposit materials on high-aspect ratio structures without gradients or pinholes has become increasingly challenging.

Atomic layer deposition (ALD) has become an enabling deposition technique in the semiconductor industry owing to its ability to control film thicknesses with angstrom scale precision while achieving highly conformal coverage on high-aspect ratio substrates (>2000:1).[43,44] Furthermore, ALD is a scalable process as it is not line-of-sight dependent, and does not require high vacuum levels or temperatures. As a result of these beneficial

qualities ALD is currently used widely in both front-end and back-end processing in semiconductor manufacturing. A recent study reported a compound annual growth rate in the global ALD equipment of 26.4% from 2020 to 2026, and projections expect it to reach $1,335.3 million by the end of 2026,[45] cementing ALD's rising importance in the field of nanodevices.

Atomic Layer Deposition (ALD) is a vapor-phase deposition technique that has demonstrated the ability to manufacture thin films with atomically-precise control of thickness and composition.[46] ALD is a modified Chemical Vapor Deposition (CVD) process, and typically occurs in two steps (Figure 2.1). The first step consists of a precursor gas that is pulsed into a chamber, reacts with the substrate in a self-limiting manner, and is then purged with an inert gas. A second step pulses a different precursor gas that reacts in a self-limiting manner with the adsorbed layer of the first precursor. The chamber is then purged once more with an inert gas. The culmination of both half-reactions results in the deposition of one "ALD cycle", with typical thickness control ranging from 0.1-3 Å/cycle. This process is repeated in a cyclic manner to deposit additional layers until thin-film of the desired thickness is formed.

The ideal conditions for reproducible control in ALD processes are strongly affected by the temperature profile across the substrate surface. The temperature range for which these ideal conditions are met is known as the ALD window (Figure 2.2). Within the ALD window, the film growth displays the repeatable self-limiting behavior characteristic of ALD. Temperatures outside the ALD window cause deviations from the ideal ALD process such as precursor condensation, decomposition, or desorption, or kinetically limited surface reactions. These deleterious effects result in non-conformal or uncontrolled film deposition. Therefore, precise spatial control of the temperature in the reaction chamber is essential for successful ALD processes.

Non-ideal growth behavior during the initial cycles may still occur even when the conditions for self-limiting ALD processes are met. For example, slower ALD film growth can

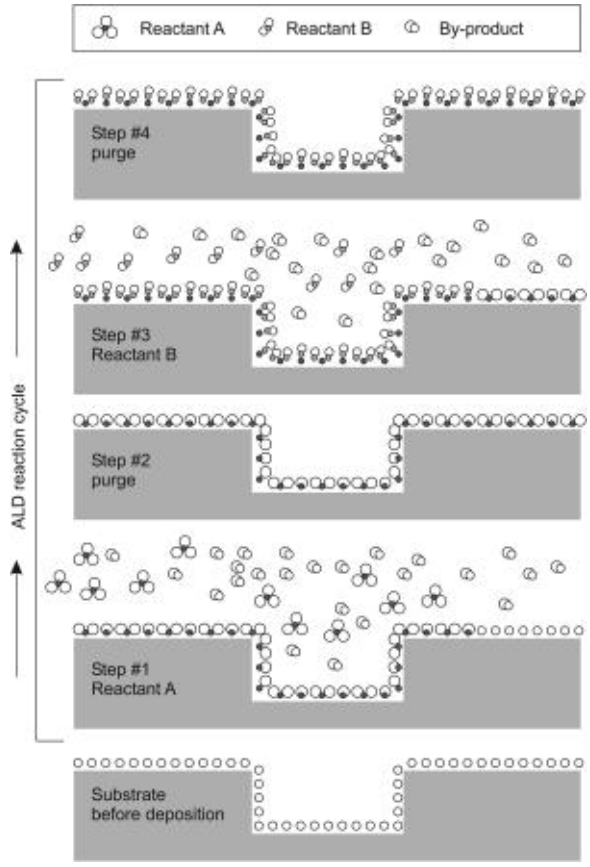

Figure 2.1: *Schematic illustration of one ALD reaction cycle. [Reprinted with permission from Puurunen, R. L. Surface chemistry of atomic layer deposition: A case study for the trimethylaluminum/water process. J. Appl. Phys. 2005,* ***97****, 121301. Copyright 2005 AIP Publishing LLC]*

take place due to delayed nucleation of the film or steric hindrances between the precursor molecules.[47–50] Nucleation delay often occurs on surfaces that are inherently chemically inert, due to a lack of functional species on the surface for the precursor to react with. As a result, the growth rate will initially be slow, and the precursor will react with only a few surface sites. During the following ALD cycle, the precursor will tend to react preferentially with the existing ALD material instead of the inert substrate. This results in the formation of *islands* during the initial cycles, instead of a continuous film. As the neighboring islands grow, they eventually merge to form a continuous film and a steady growth rate is attained.

A similar behavior is observed in cases where steric hindrance occurs. Steric hindrance is possible even when active sites for precursor chemisorption is highly favorable. Pre-

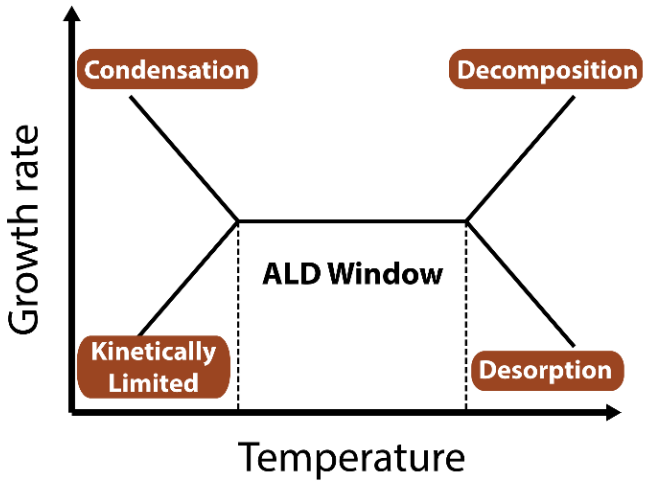

Figure 2.2: *ALD window*

cursor molecules that have already chemisorbed or adsorbed on the substrate surface have remaining ligands that can potentially block the reaction on nearby sites. A similar delay in the formation of a continuous film is initially observed, but a steady growth rate is obtained once the film is fully formed. In conclusion, the growth behavior of ALD films are highly dependent on precursor chemistry, substrate surface chemistry, substrate temperature, and precursor dosage, and thus the control of process parameters are necessary to obtain the full characteristics of ideal ALD.

When the ideal conditions are met, ALD can be a powerful platform for a wide range of applications ranging from energy conversion and storage to nanocomposites and interfacial mechanics. This diverse set of technology areas requires a wide range of functional materials that can be tuned with atomic-scale control that can be enabled by ALD.

2.2 Basics of Fiber-Reinforced Composites

The need for lightweight materials has become increasingly important as the demand to reduce fuel use and carbon emissions continues to be of critical significance. To this end, fiber-reinforced composites (FRCs) are lightweight structural materials that are of great

interest to the aerospace industry and to high-performance vehicle manufacturers because of their high values of specific strength and toughness compared to metal structures. FRCs are able to obtain these desirable properties through the implementation of high-modulus and low-weight fibers into a polymer matrix. A few examples of fibers commonly utilized in FRCs include glass fibers, carbon fibers, and aramid fibers. The following sections will briefly discuss the basic principles of continuous FRCs.

2.2.1 Macromechanical Stress-Strain Relationships of Orthotropic Laminae

First, we will discuss the macroscopical properties of a continuous FRCs lamina, assuming linear-elastic behavior. There are nine stress components (σ_{ij}) that describe the 3-D state of stress of a material (Figure 2.3), where i and j denote the axes directions in a 3-D coordinate system. The coordinate system is composed of three perpendicular coordinate axes. The stress state can be described by three normal stress components ($i = j$) and six shear stress components ($i \neq j$). However, given certain conditions of symmetry ($\sigma_{ij} = \sigma_{ji}$), the total components of shear stress can be simplified down to three. Thus, the 3-D state of stress can be described with just six total stress components (i.e. three normal and three shear). The strain state of the material (ε_{ij}) can also be reduced to six total components following this same logic.

In materials design, it is necessary to understand the stress-strain relationships of the system. Each stress component can be expressed as a function of all the strain components by the utilization of Hooke's Law. A simplified matrix form can be used to describe all of the relationships relating stresses to strains. This is referred to as the stiffness matrix [C], which is a fully populated matrix of stiffness constants that relate the stress to the strain for these particular components. The full relationship can be expressed as:

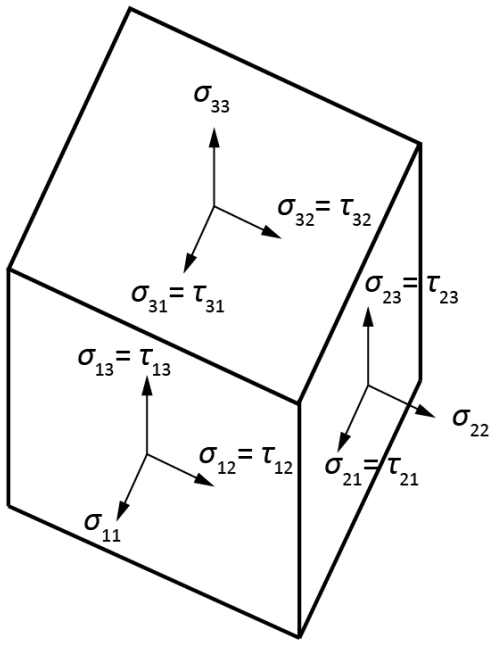

Figure 2.3: *3-D state of stress*

$$\begin{pmatrix} \sigma_{11} \\ \sigma_{22} \\ \sigma_{33} \\ \sigma_{23} = \tau_{23} \\ \sigma_{31} = \tau_{31} \\ \sigma_{12} = \tau_{12} \end{pmatrix} = \begin{bmatrix} C_{11} & C_{12} & C_{13} & C_{14} & C_{15} & C_{16} \\ C_{21} & C_{22} & C_{23} & C_{24} & C_{25} & C_{26} \\ C_{31} & C_{32} & C_{33} & C_{34} & C_{35} & C_{36} \\ C_{41} & C_{42} & C_{43} & C_{44} & C_{45} & C_{46} \\ C_{51} & C_{52} & C_{53} & C_{54} & C_{55} & C_{56} \\ C_{61} & C_{62} & C_{63} & C_{64} & C_{65} & C_{66} \end{bmatrix} \begin{pmatrix} \varepsilon_{11} \\ \varepsilon_{22} \\ \varepsilon_{33} \\ \varepsilon_{23} = \frac{\gamma_{23}}{2} \\ \varepsilon_{31} = \frac{\gamma_{31}}{2} \\ \varepsilon_{12} = \frac{\gamma_{12}}{2} \end{pmatrix} \tag{2.1}$$

where γ_{ij} is the engineering strain and τ_{ij} is the shear stress. Similarly, strain components can be expressed as a function of all the stresses that can fully be described by the compliance matrix [*S*], which is also the inverse of the compliance matrix (or $[C]^{-1}$). The full relationship here becomes:

$$\begin{pmatrix} \varepsilon_{11} \\ \varepsilon_{22} \\ \varepsilon_{33} \\ \varepsilon_{23} = \frac{\gamma_{23}}{2} \\ \varepsilon_{31} = \frac{\gamma_{31}}{2} \\ \varepsilon_{12} = \frac{\gamma_{12}}{2} \end{pmatrix} = \begin{bmatrix} S_{11} & S_{12} & S_{13} & S_{14} & S_{15} & S_{16} \\ S_{21} & S_{22} & S_{23} & S_{24} & S_{25} & S_{26} \\ S_{31} & S_{32} & S_{33} & S_{34} & S_{35} & S_{36} \\ S_{41} & S_{42} & S_{43} & S_{44} & S_{45} & S_{46} \\ S_{51} & S_{52} & S_{53} & S_{54} & S_{55} & S_{56} \\ S_{61} & S_{62} & S_{63} & S_{64} & S_{65} & S_{66} \end{bmatrix} \begin{pmatrix} \sigma_{11} \\ \sigma_{22} \\ \sigma_{33} \\ \sigma_{23} = \tau_{23} \\ \sigma_{31} = \tau_{31} \\ \sigma_{12} = \tau_{12} \end{pmatrix} \tag{2.2}$$

For purposes of simplification, the following discussion will focus on the stress-strain relationships specific to unidirectional and continuous FRCs. Often, a single lamina is referred to as a *specially orthotropic* material that is under plane stress (2-D state of stress) conditions. Under these assumptions, the out-of-plane properties need not be considered (i.e. $\sigma_{33} = \tau_{23} = \tau_{31} = 0$). Furthermore, if the direction of the fibers are aligned with one of the coordinate axes, then there will exist two orthogonal planes of symmetry. In this situation, there will not exist any interactions between the normal strains and shear strains nor between the shear stresses in different planes. Thus, the strain-stress relationship can be simplified to:

$$\begin{pmatrix} \varepsilon_{11} \\ \varepsilon_{22} \\ \gamma_{12} \end{pmatrix} = \begin{bmatrix} S_{11} & S_{12} & 0 \\ S_{21} & S_{22} & 0 \\ 0 & 0 & S_{66} \end{bmatrix} \begin{pmatrix} \sigma_{11} \\ \sigma_{22} \\ \tau_{12} \end{pmatrix} \tag{2.3}$$

Finally, after substituting the orthotropic engineering constants into the simplified compliance matrix, the general strain-stress relationship for a continuous and unidirectional fiber-reinforced lamina becomes:

$$\begin{pmatrix} \varepsilon_{11} \\ \varepsilon_{22} \\ \gamma_{12} \end{pmatrix} = \begin{bmatrix} \frac{1}{E_1 1} & \frac{-v_{21}}{E_2 2} & 0 \\ \frac{-v_{12}}{E_1 1} & \frac{1}{E_2 2} & 0 \\ 0 & 0 & \frac{1}{G_{12}} \end{bmatrix} \begin{pmatrix} \sigma_{11} \\ \sigma_{22} \\ \tau_{12} \end{pmatrix} \tag{2.4}$$

where in this particular case, E_{11} and E_{22} are the Young's moduli of the composite in the longitudinal (parallel to the fibers) and transverse (perpendicular to the fibers) directions, respectively, G_{12} is the shear modulus, and v_{ij} is the Poisson's ratio ($v_{ij} = -\varepsilon_{jj}/\varepsilon_{ii}$).

2.2.2 Micromechanical Relationships of Fiber-Reinforced Composites

In the previous section, we reviewed the stress-strain relationships of a unidirectional fiber-reinforced lamina, which were expressed as a function of its effective material properties (i.e. E_{11}, E_{22}, G_{12}, v_{12}, and v_{21}). Here, we will briefly review the basic principles to estimate these effective properties.

First, the Young's modulus and the Poisson's ratio of each constituent need to be known as well as the fiber volume fraction. For continuous fiber composites, the cross-sectional fiber volume fraction is often assumed to be constant along the longitudinal direction. The fiber volume fraction (V_f) can thus be expressed as:

$$V_f = \frac{A_f}{A_c} = \frac{A_f}{A_f + A_m} \tag{2.5}$$

where A_c is the total cross-sectional area of the composite, A_f is the cross-sectional area of the fibers, and A_m is the cross-sectional area of the matrix. Accurate measurements of the fiber volume fraction are essential to estimate the longitudinal and transverse moduli (E_{11} and E_{22}, respectively).

When a tensile force is applied in the longitudinal direction, the fiber reinforcements and matrix behave in a manner analogous to springs connected in parallel. In this case, the strain of the matrix ($\varepsilon_{m_{11}}$) and the strain of the fibers ($\varepsilon_{f_{11}}$) are assumed to be equal to the strain of the composite ($\varepsilon_{c_{11}} = \varepsilon_{m_{11}} = \varepsilon_{f_{11}}$). The stress, however, is not uniform across the cross-section, and is highly depend on the modulus of the constituents. Static equilibrium equations help reveal the impact of the modulus on stress.

$$T_{c_{11}} = T_{m_{11}} + T_{f_{11}} \tag{2.6}$$

where $T_{c_{11}}$ is the total tensile force applied on the composite system and $T_{m_{11}}$ and $T_{f_{11}}$ are the tensile forces on the matrix and fibers, respectively. To obtain this equation expressed in terms of the moduli, the following equations are needed:

$$T_{c_{11}} = \overline{\sigma}_{c_{11}} A_c \; ; \; T_{m_{11}} = \overline{\sigma}_{m_{11}} A_m \; ; \; T_{f_{11}} = \overline{\sigma}_{f_{11}} A_f \tag{2.7}$$

where $\overline{\sigma}_{c_{11}}$, $\overline{\sigma}_{m_{11}}$, and $\overline{\sigma}_{f_{11}}$ are the average tensile stresses of the composite, matrix, and fibers, respectively. Substituting Equation 2.7 into Equation 2.6 yields:

$$\overline{\sigma}_{c_{11}} A_c = \overline{\sigma}_{m_{11}} A_m + \overline{\sigma}_{f_{11}} A_f \tag{2.8}$$

which can be expressed as a function of the fiber volume fraction by substituting Equation 2.5 into Equation 2.8:

$$\overline{\sigma}_{c_{11}} = \overline{\sigma}_{m_{11}} (1 - V_f) + \overline{\sigma}_{f_{11}} V_f \tag{2.9}$$

Lastly, assuming all constituents follow the one-dimensional (1-D) Hooke's Law, the modulus of the constituents can be inserted into Equation 2.9:

$$E_{c_{11}} \varepsilon_{c_{11}} = E_{m_{11}} \varepsilon_{m_{11}} (1 - V_f) + E_{f_{11}} \varepsilon_{f_{11}} V_f \tag{2.10}$$

and can be simplified further because the strain of the composite is the same as the strain in the matrix and the strain in the fiber:

$$E_{c_{11}} = E_{m_{11}} (1 - V_f) + E_{f_{11}} V_f \tag{2.11}$$

where $E_{c_{11}}$ is the *effective modulus* of the composite, $E_{m_{11}}$ is the modulus of the matrix, and

$E_{f_{11}}$ is the modulus of the fibers. This equation is known as the rule of mixtures, and can provide an estimate of the effective longitudinal modulus of a FRC

The transverse modulus however, behaves contrary to the longitudinal modulus, in the sense that when pulled in the transverse direction, the fiber reinforcements and matrix behave analogous to springs connected in series. Thus, the strain of the individual constituents are no longer considered to be equal. Instead, the total displacement of the composite needs to be equal to the sum of the displacements of the individual constituents. This can be expressed using the following equation:

$$\delta_{c_{22}} = \delta_{m_{22}} + \delta_{f_{22}} \tag{2.12}$$

where $\delta_{c_{22}}$ is the total displacement of the composite, $\delta_{m_{22}}$ is the total displacement of the matrix, and $\delta_{f_{22}}$ is the total displacement of the fabric.

Following similar method of equation substitutions, we eventually arrive with an equation that describes the effective transverse modulus ($E_{c_{22}}$):

$$E_{c_{22}} = \frac{E_{m_{22}} E_{f_{22}}}{(1 - V_f) E_{m_{22}} + V_f E_{f_{22}}} \tag{2.13}$$

where ($E_{m_{22}}$) and ($E_{f_{22}}$) are the transverse moduli of the matrix and the fibers, respectively. The resulting equation is known as the inverse rule of mixtures. This method predicts the correct trend relative to the fiber volume fraction; however, it is generally considered to not be an accurate estimate of the effective transverse modulus of the composite.

Finally, the Poisson's ratio of the composite (ν_{12}) and the shear modulus (G_{12}) can also be estimated. The Poisson's ratio follows the rule of mixtures, whereas the shear modulus follows the inverse rule of mixtures. Similarly, the rule of mixtures provides an accurate estimate, but the inverse rule of mixtures does not.

2.2.3 Interfaces of Fiber-Reinforced Composites

A key area of research for the development of high-performance FRCs lies in the study of mechanical properties at the fiber-matrix interface. Control of the mechanical properties at the fiber-matrix interface is critical in the design of composite systems. The desired mechanical properties of this interface vary for different types of FRCs. For fiber-reinforced PMCs, strong fiber-polymer interfaces are desired to maximize load transfer to the fiber because the polymer-matrix has relatively low stiffness and strength. In contrast, for fiber-reinforced ceramic-matrix composites (CMCs), weaker interfaces are generally desired. Typical ceramic matrices such as silicon carbide (SiC) are relatively stiff and strong, but brittle. Therefore, fibers can increase toughness by providing a weak fiber-matrix interface that promotes crack deflection and dissipates energy.[51,52] Therefore, the ability to tune and tailor the adhesion at the fiber-matrix interface enables control of the bulk mechanical properties of the composite.

Because the desired interfacial properties vary among composite material systems, new pathways to precisely modify the fiber-matrix interface present opportunities for rational design of material properties of FRCs. The two main methods to tune the interfacial properties of composites are done through chemical modification and through physical modification of the fiber surface. The work presented throughout this dissertation will primarily focus on the chemical modification of aramid fiber and carbon fiber surfaces.

Carbon fibers and Kevlar® aramid fibers are known to have smooth and chemically inert surfaces, which can result in poor compatibility and adhesion between the polymer matrix and the structural fibers.[53–56] PMCs that utilize these fibers rely on strong adhesion at the interface between these materials to fully benefit from the strength-enhancing benefits of the fiber reinforcements. Therefore, researchers have looked into incorporating surface treatments on the fibers to introduce additional active functional groups on the surface, which promote stronger adhesion to the polymer matrix.

Some of the surface treatments commonly used include electrochemical oxidation,[57,58]

plasma treatments,[59–66] acidic and basic solution treatments,[67–72] among others. These treatments increase the content of surface functional groups that enhance the interfacial bonding strength.[73] However, intense surface functionalization treatments can also sometimes reduce the tensile strength of the fibers due to excessive oxidation and damage to its exterior.[67,70,74] Thus, these applications require controlled but sufficient exposure in order to provide sufficient functionalization on the fiber surface, while minimizing detrimental effects of the fiber's tensile properties.

Another way to modify the fiber-matrix interface, without affecting the tensile strength of the fiber, is by adding an intermediate layer onto the fiber surfaces before incorporating them into the matrix. Sizing layers are frequently added to fibers for protection during manufacturing.[75] Sizings influence the strength and toughness at the fiber-matrix interface, which can be modified by changing the surface chemistry or morphology.[76–79] For example, previous surface modification of fibers has explored the addition of graphene oxide sheets[80] or carbon nanotubes (CNTs) to fiber surfaces[81,82] to strengthen the interface of PMCs. Chemical vapor deposition (CVD)[82,83] has also been used to coat glass fibers and carbon fibers. However, in the case of both PMCs and CMCs, the ability to conformally coat tows and woven fabrics is challenging due to high aspect-ratios and overlapping geometries that block line-of-sight deposition. As a result, these modified coating processes are often studied at the single-fiber level. CVD and physical vapor deposition (PVD) have been explored for coating fabrics; however, precise control of the composition and phase of the coatings on 3-D templates can be challenging.[84] Furthermore, in the case of nanocomposites, the need for highly conformal and uniform deposition processes at the nanoscale is pivotal to engineer interfacial properties. This highlights the need for deposition processes that allow for precise control and tunability of process parameters.

Atomic layer deposition (ALD) is a gas-phase deposition technique that allows for improved conformality and precise compositional control compared to conventional gas-phase and solution-based processes.[43] It has been previously shown that ALD can confor-

mally coat tows of fibers and woven fabrics with various compositions of metal oxides, alleviating the limitations of other coating techniques.[85–89] Additionally, Liang et al. demonstrated that the mechanical properties of multi-walled carbon nanotubes (MWCNTs) dispersed in a polymer-derived ceramic matrix could be altered significantly by controlling the coating material and the number of deposition cycles.[90] However, despite the advantages of ALD for interfacial engineering of composites, relatively few studies have explored the impact of ALD coatings on interfacial mechanics of FRCs.[91]

In addition to modification of the mechanical properties of FRCs, interfacial coatings may also be used to introduce new functionality into the composite. For example, deposition of dispersed CNTs onto fiber surfaces has been shown to significantly change the electrical and thermal properties of a fiber-reinforced laminate.[81,82,92] PZT ($PbZr_{0.52}Ti_{0.48}O_3$) coatings on carbon fibers and $BaTiO_3$ coatings on SiC fibers have demonstrated that piezoelectric interfaces can be used to convert mechanical stress from vibrational energy into an electrical signal.[93,94] These examples demonstrate that precisely engineered modifications at the interface of a FRC can enable the development of multifunctional composites.

Among the various modification methods available, ALD presents an excellent opportunity to develop multifunctional materials.[95] ALD can be used to deposit a wide range of material systems facilitating a virtually limitless selection and combination of materials with specific properties.[96,97] This ability to precisely tune interfacial chemistry and structure offers a powerful method for multifunctional composites development by design.[98]

2.3 Basics of Photocatalysis

Problems related to remediation of hazardous waste have emerged as a global priority that require addressing. Furthermore, investigation of renewable resources to address energy needs is also of urgent importance to address the effects of climate change today. Research in the field of photocatalysis presents an opportunity to address both.[99,100] Over the last

several decades, semiconductor photocatalysis has been extensively studied as a means to utilize the energy from the sun to address both environmental and energy needs.[101,102] Photocatalysis is generally defined as the acceleration of a photochemical reaction, that occurs at the surface of the photocatalyst, which initiates upon the absorption of energy from light. Homogeneous (solid-solid interfaces) and heterogeneous (solid-liquid and solid-gas interfaces) photocatalysts can be utilized in a variety of applications. Photocatalytic fuel production through water splitting of hydrogen and oxygen or through the reduction of carbon dioxide to produce fuels such as methanol are examples of such applications of renewable energy. Examples of applications related to environmental decontamination have also been demonstrated, such as water and air purification, degradation of hazardous waste, and pathogen inactivation.[101] The field of semiconductor photocatalysts is multidisciplinary, bringing together concepts from solid-state physics, photochemistry, and surface science. A summary of essential concepts that pertain to the work in Chapter 6 (i.e. heterogenous photocatalysts for water purification) are briefly reviewed below.

2.3.1 Principles and Mechanisms of Heterogeneous Photocatalysis for Water Purification

The mechanisms presented here will be discussed from the perspective of dye degradation in water, but also apply more generally to water decontamination and bactericidal applications. In order for the process of dye degradation in aqueous solution to take place, a semiconductor with a sufficiently large bandgap needs to be used to drive oxidation-reduction reactions. This bandgap needs to be sufficiently large to provide the necessary electrochemical potential to drive the reaction, and it needs to align such that the valence and conduction bands are below and above the necessary electrochemical potential s for oxidation and reduction, respectively. TiO_2 and ZnO are common examples of semiconductors that meet these requirements. However, even though these semiconductors can serve as functional photocatalysts, their broad band gap values requires the use of UV light

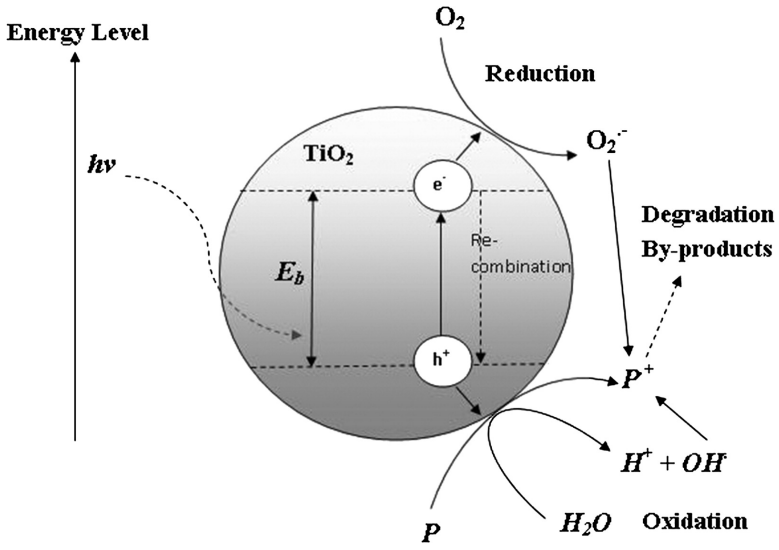

Figure 2.4: *Representative photo-induced formation mechanism of electron–hole pair in a semiconductor (e.g. TiO_2 particle) with the presence of water pollutant (P). [Reprinted with permission from Chong, M. N.; Jin, B.; Chow, C. W. K.; Saint, C. Recent developments in photocatalytic water treatment technology: A review. Water Res. 2010, **44** (10), 2997-3027. Copyright © 2010 Elsevier Ltd.]*

to achieve photoactivation.

The photons incident on the semiconductor need to have an energy (*hv*) that is equal or greater than the bandgap to be absorbed by the material. This absorbed photon can then excite an electron from the valence band to the conduction band of the semiconductor. As a negatively-charged electron (e^-) moves to the conduction band, a positively-charged hole is left behind in the valence band. This results in the generation of an electron-hole pair. Because the surface of the semiconductor is in contact with the water, an electron-hole pair migrates to the solid-liquid interface before recombination can simultaneously react with the molecules in the water. Generally what happens during this photocatalytic reaction is that hydroxyl radicals ($^{\bullet}OH$) will begin to evolve. This occurs as a result of the byproducts from the interaction between the photogenerated holes and the water (Figure 2.4). The electrons in the conductive band can also interact with dissolved oxygen (O_2) through a series of reactions to produce additional ($^{\bullet}OH$).

The evolution of these powerful oxidizing ($^{\bullet}OH$) species is particularly important for

the dye degradation process. As the dye molecules adsorb onto the semiconductor surface, the ($^{\bullet}$OH) radicals will begin to attack the dye through an oxidation process. While there are other mechanisms that can also contribute to dye degradation, the consensus in the literature denotes this to be the primary mechanism and the largest contributing factor for photocatalytic dye degradation.

Chapter 3

Design of Atomic Layer Deposition Reactor for Scalable Manufacturing with Improved Thermal Design

ALD can be utilized for a wide range of applications ranging from energy conversion and storage to nanocomposites and interfacial mechanics. Application of ALD to this diverse set of technology areas requires a wide range of functional materials that can be tuned with atomic-scale control.

For example, ALD of TiO_2, a functional semiconductor material, is of significant importance in a wide range of ALD applications ranging from high-k dielectrics, to gas sensing, to solar energy conversion. It is also an example of a material for which there are inconsistencies in the published literature on the reported ALD window.[103–105] Furthermore, defects such as adventitious incorporation of impurities in the ALD films have been reported, which can affect the electronic properties of the films. These inconsistencies are likely to be heavily dependent on variations in ALD reaction chamber designs, including spatial variations in surface temperature sensing and heat flux. Furthermore, many reports of ALD growth rate and ALD windows do not provide spatial maps of thickness across larger areas, and do not confirm that the reported temperature was locally measured in the region of reported growth rate. These inconsistencies in monitoring and reporting the coupling between localized spatial gradients in temperature and variations in ALD growth

presents a problem for the ALD community, and highlights the need for improved accuracy in thermal reactor design and spatial temperature sensing.

Furthermore, if ALD is to be used in larger scale applications, such as multifunctional composites, design of larger reactors will be necessary. Control of proper temperature distribution becomes more challenging at these larger length scales, thus careful thermal design considerations become critical. The goal of this study was to understand how inconsistencies in proper temperature monitoring can lead to undesired ALD growth and to implement strategies for improved temperature control in ALD systems.

3.1 Results and Discussion

This study was performed using TiO_2 as the deposited material. The tests were performed with the reaction chamber set to 200 °C based on reported temperatures for the deposition of TiO_2 with tetrakis(dimethylamido)titanium (TDMAT) and water as precursors. Ellipsometry was used to measure the thickness and uniformity of TiO_2 films deposited by ALD on planar 4" diameter Si (100) substrates. TiO_2 film growth initially demonstrated anomalous behavior, which was indicative of non-ideal ALD growth. Data from Table 3.1 shows inconsistent growth and thickness variations at the positions shown in Figure 3.1. The growth rate at the center of the chamber was significantly higher than the thickness at the edges. Across the 4" deposition region, the per cycle growth rate showed a percent range of 27.2% and a standard deviation of 0.18 Å. It was hypothesized that the non-uniform thickness was a result of spatial variations in the substrate temperature, causing some local regions to be outside the ALD window for TiO_2.

To verify this hypothesis, a series of thermocouple measurements, infrared (IR) imaging, and finite element analysis (FEA) were performed. Separate thermocouples were used to measure the temperature directly at the reactor surface in various positions. The locations of the thermocouples in the chamber and the temperature measurements obtained

Table 3.1: *Growth rate of TiO_2 at positions from Figure 3.1. Chamber set to 200 °C.*

POSITION	GROWTH RATE (Å/CYCLE)
1	1.14
2	0.77
3	0.81
4	0.73
5	0.69
Mean	0.83
Std Dev	0.18
% Range	27.2%

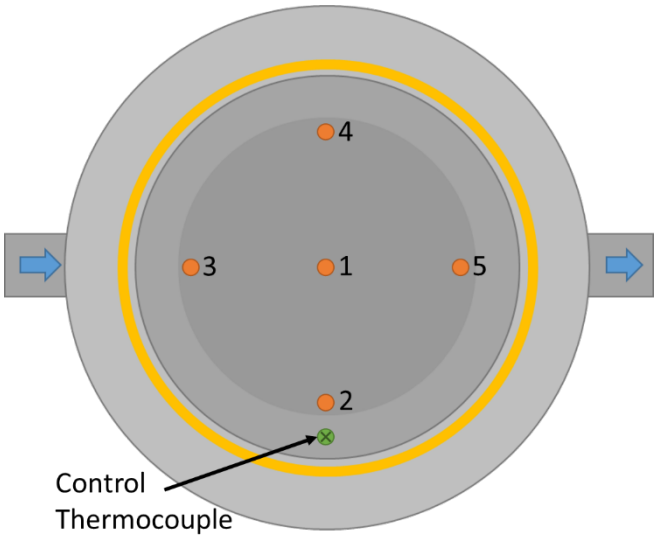

Figure 3.1: *Positions on the chamber from which multiple measurements were taken. Also indicates the thermocouple location of the former chamber design.*

from these locations are shown in Figure 3.1 and Table 3.2, respectively. The results show a temperature gradient of 51 °C between the center and the edge of the reaction surface. Additionally, the temperature at the center of the chamber was 236 °C, which is significantly higher than the intended set temperature of 200 °C. IR imaging was also performed to provide a higher resolution map of the observed thermal behavior (Figure 3.2a and 3.2b, respectively). IR imaging demonstrated an upper bound temperature between 230-240 °C and the lower bound between 170-180 °C, with the temperature radially decreasing from the center toward the edges.

To gain insight into the origins of this temperature gradient, FEA analysis was per-

Table 3.2: *Thermocouple temperature measurements on positions from Figure 3.1 (Control Set to 200 °C)*

POSITION	TEMPERATURE (°C)
1	236
2	185

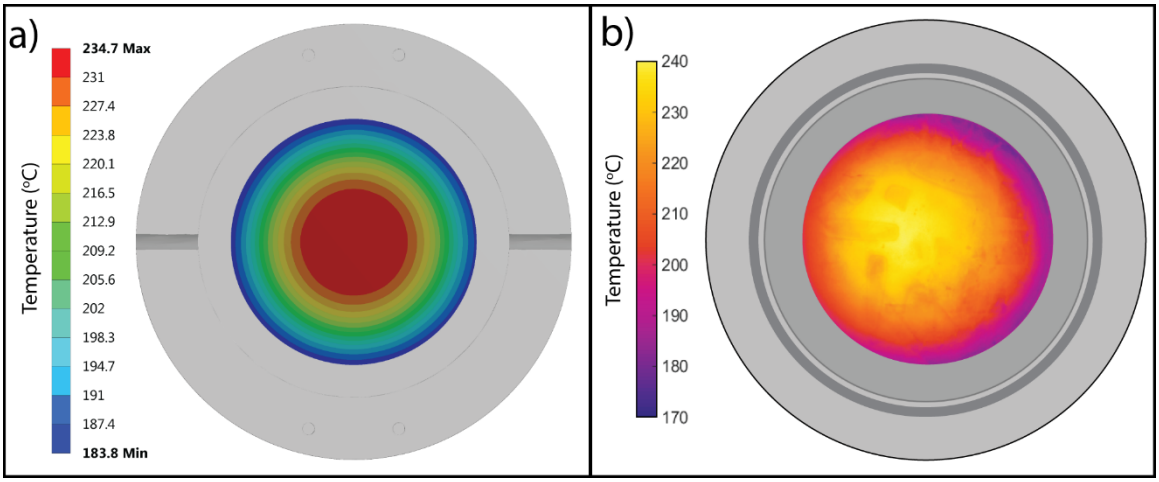

Figure 3.2: *(a) FEA & (b) IR imaging showing thermal profile of the reaction chamber.*

formed on the chamber, using the heater as an input, and with boundary conditions of the FEA that were set to be representative to the conditions in the environment, including heat dissipation due to natural convection and radiation. The thermal properties for each component were input based on material properties. The FEA results predicted a maximum temperature of 234.7 °C with a gradient of 50.9 °C, and almost perfectly replicated the thermocouple measurements. These results confirm the need to develop an improved thermal system design that both senses and controls spatial variations in substrate temperatures with a high degree of confidence, in order to improve reproducibility.

Originally, the custom-made ALD station used a ceramic heater (Watlow Electric Manufacturing, Co.) to heat the deposition chamber. These ceramic heaters are made from aluminum nitride, provide durable heater construction and thermal transfer necessary for high temperature and long heater life, and their high thermal conductivity make for an ultra-fast temperature ramp rate of up to 150°C (270°F) per second. However, the partic-

ular design of the heater used in this original reactor design was not optimized to obtain lateral uniform temperature distribution. Furthermore, material incompatibility and contact resistance between the aluminum nitride of the heater and the stainless steel of the reaction chamber required a high conductive and malleable interface to improve contact and heat conduction. Lastly, the ceramic heater has an internal thermocouple that measures the heater temperature, but an offset was measured between the heater temperature and substrate temperature when using a separate thermocouple. Therefore, a copper foil was inserted as an interfacial buffer to improve thermal conduction. However, copper oxidizes in air at high temperatures, which can degrade the thermal conductivity, which could lead to a decrease in accuracy over time.

In addition to the heater design, temperature sensor integration also affect the thermal profile of the ALD chamber. One challenge in ALD system design is that a single temperature sensor often provides inaccurate temperature feedback to the temperature controller, which maintains the targeted substrate temperature. Unless the heater accommodates insertion of the sensor in a representative region that accurately reflects the surface temperature of the substrate, an offset will instead be measured. Surface-mounted thermocouples with high-temperature adhesives are not very robust and can easily and accidentally be peeled off. Other more robust thermocouple integrations are more intrusive and could limit heater integration and/or disrupt thermal uniformity. The original ALD chamber used for this study utilized an RTD threaded thermocouple. However, due to its bulky geometry it was placed adjacent to the heater to avoid disturbing the thermal distribution, working under the simplifying assumption that the deposition surface was close to isothermal. Furthermore, this control thermocouple was located 2.25 inches away from the center of the chamber, since the flat Ultramic heater did not allow insertion of the thermocouple directly in between the heater and chamber outer surface. As a result, the thermocouple reading did not accurately measure the actual temperature at the surface of the reaction chamber, and could not capture the temperature gradient observed in the IR data. The lack of tempera-

ture uniformity and accurate temperature sensing and control are leading examples of the limitations many ALD systems currently face, and are directly correlated to the quality and uniformity of the resulting films, as demonstrated by the coupled thermal and thickness behavior reported above.

The need for high precision and high accuracy thermal system design becomes increasingly important as the ALD community develops new precursors and more complex materials with new functionalities but with narrower ALD windows. Furthermore, not all ALD processes exhibit a growth rate that is constant with temperature inside the ALD window. The higher demand of these new ALD chemistries require improvements in thermal system design in order to obtain reproducible ALD behavior. In these cases, it is especially important to maintain temperature uniformity across the substrate in order to obtain uniform film thickness. To address this challenge, Watlow Electric Manufacturing Co. worked collaboratively with the Dasgupta Research Group to provide a redesigned solution in order improve the thermal profile of the ALD chamber, as well as the accuracy of the temperature sensing.

Watlow's 430 stainless steel thick film conduction heaters provide a good combination of heat transfer, thermal efficiency, and temperature uniformity. They also offer design flexibility, allowing for configurations of different circular and rectangular shapes and sizes, and can be designed for areas where space is unconventionally small. Furthermore, because design flexibility of the heating elements is possible, FEA modeling can be used to inform the heater design in order to achieve proper thermal distribution over a wide range of temperature set points. Additionally, the thick film heaters ensure efficient heat transfer and precise resistance trace patterns, ensuring maximum temperature response.In hte modified reactor design, the single threaded insert thermocouple was replaced by two spring-loaded thermocouples. The spring-loaded thermocouples present an advantage over alternate sensor designs, such as surface mount or screw-in thermocouples. The reproducibility and accuracy of these traditional sensor designs may diminish as the chamber undergoes ther-

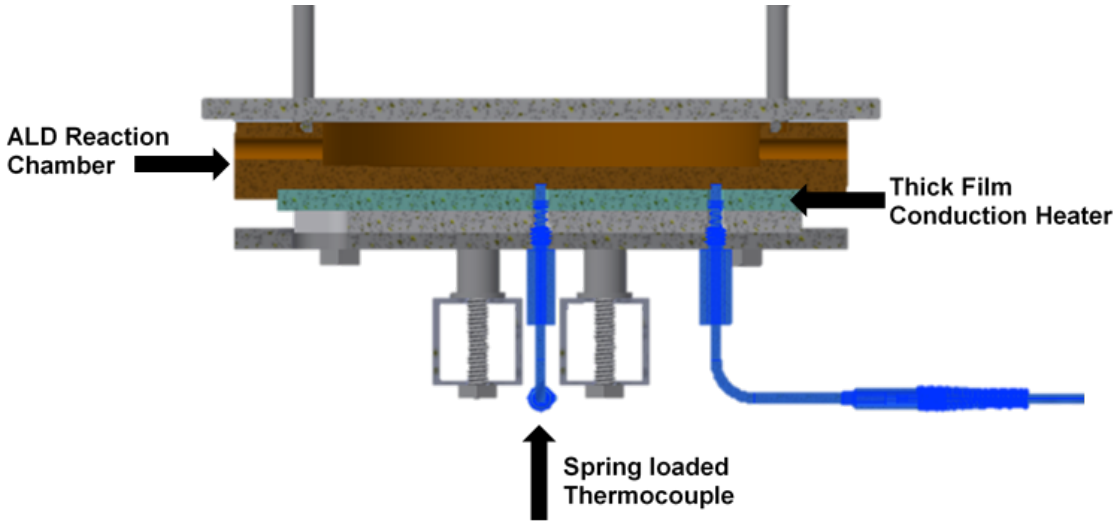

Figure 3.3: *Cross-sectional 3-D model of assembled ALD chamber with thick film conduction heater and spring loaded thermocouples.*

mal cycling, which can loosen contact, or affect the sensor/surface mechanical compressive load. The spring integration ensures the thermocouple maintains intimate thermal contact with the surface of interest even during thermal cycling, and enables a consistent load between the sensor and surface, improving contact resistance.

The incorporation of two thermocouples provides important feedback of the spatial temperature variations at different positions. Incorporating both the thick film conduction heater and the spring-loaded thermocouples allowed for an improved control heat transfer and temperature monitoring that drastically improved the thermal profile of the ALD reaction chamber. In order to enable improved sensor positioning, the thick film heaters were custom designed with two through holes, one at the very center and one 2 inches from the center along the radial direction. This enabled the integration of the spring-loaded thermocouples to accurately measure the radial thermal gradient across the deposition region. Additionally, the threaded portion of the thermocouple was screwed onto a structural component offset from the chamber (Figure 3.3). This allowed for only the tip of the thermocouple to be in contact with the chamber to minimize thermal disturbances. The modified thermocouple integration design allowed for more accurate temperature control and more

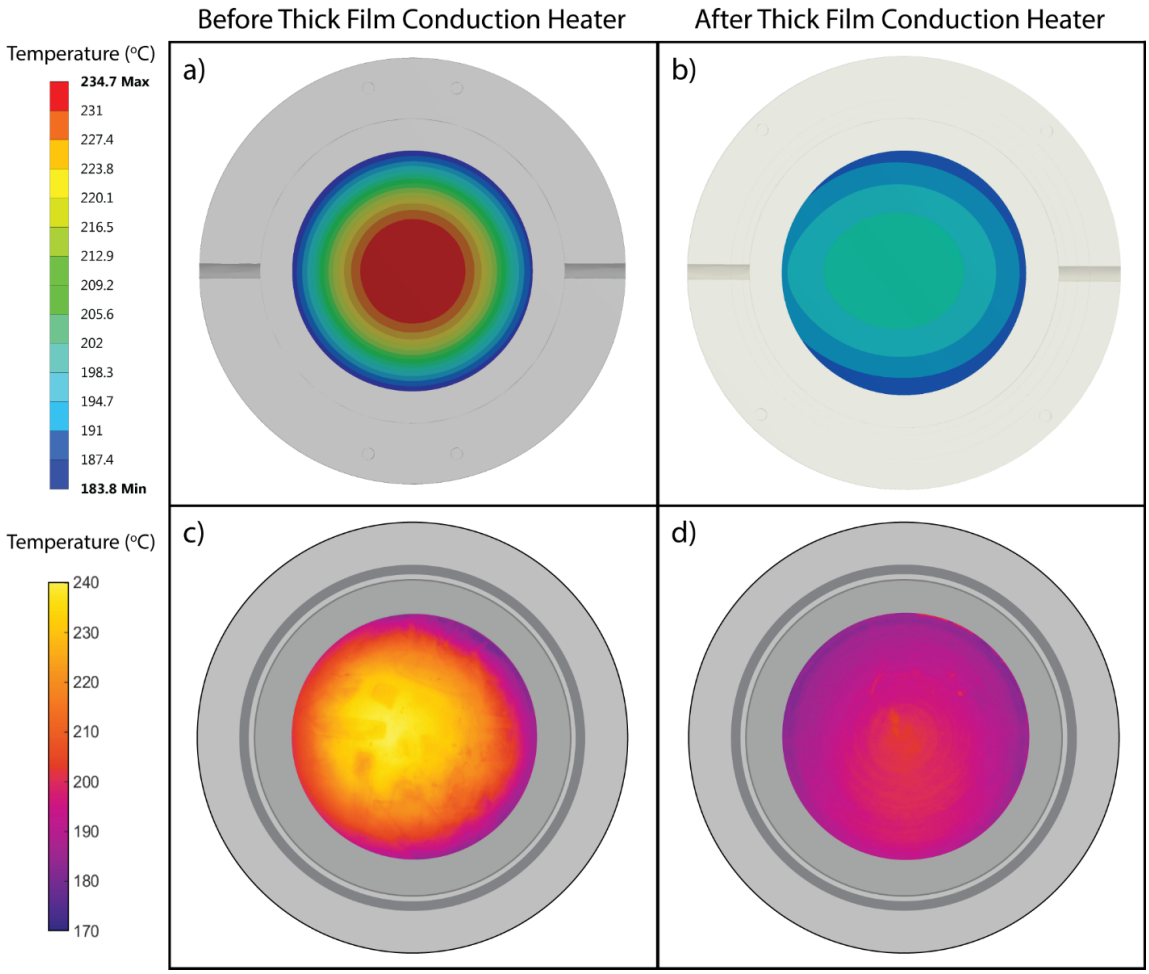

Figure 3.4: *FEA analysis (a) before and (b) after the new thermal design. IR imaging (c) before and (d) after the new thermal design.*

representative monitoring of the actual temperature profiles expected on the surface of the ALD chamber.

A temperature gradient of 9 °C with a maximum temperature of 200 °C at the center was measured between the two spring-loaded thermocouples. Additional thermocouple measurements on the deposition surface were performed to confirm the temperature profile measured by the spring-loaded thermocouples. The thermal gradient was reduced by 82% to 9°C for a setpoint temperature of 200 °C (Table 3.3), compared to the 51 °C obtained from the previous design, which is consistent with the gradient measured from the spring-loaded thermocouples. Additionally, FEA and IR imaging demonstrate similar trends to

Table 3.3: *Thermocouple temperature measurements on positions from Figure 3.1 after addition of thick film heater (Control set to 200 °C)*

POSITION	TEMPERATURE (°C)
1	198
2	193
3	193
4	193
5	189

support this improved thermal behavior. Figures 3.4a and 3.4c show the FEA and IR imaging results before the new heater design (from Figures 3.2a and 3.2b), which have been previously discussed. Figures 3.4b and 3.4d show the FEA and IR imaging results after the new heater design, and retain the temperature scale for comparison. The data from the FEA analysis predicted a maximum temperature of 201.4 °C with a temperature gradient of 13.9 °C, again showing improvements in the temperature profile across the deposition region. A similar trend is observable from the IR images.

To confirm the effect of the improved temperature profile on the ALD film growth, ellipsometry was performed using identical ALD growth conditions. The results obtained are shown in Table 3.4, and Figure 3.1 illustrates the positions where these measurements were taken. The average growth rate obtained across the deposition range was 0.76 Å per cycle, with a percent range of 2.0% and a standard deviation of 0.01 Å per cycle (Table 3.4). The deviation of the thickness variations across the chamber was reduced by 94% as

Table 3.4: *Growth rate of TiO_2 at positions from Figure 3.1 after addition of thick film heater. Chamber set to 200 °C.*

POSITION	GROWTH RATE (Å/CYCLE)
1	0.78
2	0.76
3	0.76
4	0.77
5	0.75
Mean	0.76
Std Dev	0.01
% Range	2.0%

Table 3.5: *Growth rate of TiO_2 at positions from Figure 3.1 after addition of thick film heater. Chamber set to 185 °C.*

POSITION	GROWTH RATE (Å/CYCLE)
1	0.68
2	0.67
3	0.67
4	0.67
5	0.67
Mean	0.67
Std Dev	0.004
% Range	0.7%

compared to the previous thermal design.

Additional experiments were run to verify growth rate variations when setting the reaction chamber to 185 °C. The average growth rate reported in Table 3.5 is 0.672 Å per cycle. While the standard deviation and percent range of 0.004 and 0.7% are still comparable, the growth rate is 0.1 Å less than when the chamber is set to 200 °C. This confirms a discrepancy in the growth rates from only a 15 °C variation, and merits further studies to accurately report the ALD window of materials such as TiO_2. This result identifies and supports the need for better thermal control in the ALD community, so that reported ALD windows are consistent across all platforms.

3.2 Conclusion

In this study, we measured the growth rate effects of TiO_2 and its dependence on temperature control. A poor thermal design resulted in a temperature gradient of 51 °C. This gave way to thickness variations with a percent range of 27.2% and a standard deviation of 0.18 Å, from an average growth rate of 0.828 Å per cycle. The implementation of an improved heater design, along with an accurate and precise thermal monitoring, resulted in drastically improved uniform ALD thickness across the reaction chamber. The improved thermal design significantly improved the thickness variation reducing the deviation of the growth rate by 94% and the temperature range by 93%. In conclusion, a more uniform tem-

perature profile has significantly improved the consistency of ALD thin-film processes for the deposition of materials, which was subsequently used to fabricate multifunctional composites in the later chapters of this Thesis. This improved reactor design enables precise thermal control that inspired the design and construction of a scaled-up ALD tools in our laboratory. It also highlighted the importance of accurate sensing and reporting of thermal gradients in the published literature on ALD, in order to reduce many of the inconsistencies and scatter in the reported data that hinder reproducible results.

Chapter 4

Mechanical and Interfacial Properties of Fibers Coated by Atomic Layer Deposition for Polymer-Matrix Composites with Enhanced Thermal and Ultraviolet Resistance

Adapted with permission from Rodríguez, R. E.; Cho, T. H.; Ravandi, M.; LePage, W. S.; Banu, M.; Thouless, M.D.; Dasgupta, N. P. Mechanical Properties of Fibers Coated by Atomic Layer Deposition for Polymer-Matrix Composites with Enhanced Thermal and Ultraviolet Resistance. *TMS 2020 149th Annual Meeting & Exhibition Supplemental Proceedings* 2020, 4614-4621.

In this work, we performed single-fiber microbond tests to study the mechanical properties of the interface of two fiber-polymer material systems: carbon fiber/epoxy and Kevlar®/PMMA. Al_2O_3, TiO_2, and ZnO coatings by ALD were used to study the effects of ALD modification on the mechanical properties at the interface. Furthermore, we demonstrate that ALD coatings can impart additional benefits, such as protection from radiation and thermal damage.[106] This added capability serves as a proof-of-concept demonstration that the development of multifunctional composites via ALD surface modification is possible.

4.1 Methods

The experimental procedure involved preparing samples for mechanical experiments (Section 4.1.1 "Material Systems and Specimen Preparation"). These mechanical experiments primarily used the microbond method (section 4.1.2 "Microbond Test Setup and Procedure"), and single-fiber tensile tests were also performed to assess fiber degradation during UV and thermal exposure (section 4.1.3 "Single-Fiber Tensile Tests of Kevlar® Fibers Exposed to Ultraviolet Radiation and Elevated Temperatures").

4.1.1 Material Systems and Specimen Preparation

4.1.1.1 Carbon Fiber/Epoxy

For the carbon fiber/epoxy material system, unsized HexTow® IM-8 carbon fibers (Hexcel Corporation; average fiber diameter of 5.2 μm) were used with EPO-TEK® 301 thermoset polymer (Epoxy Technology, Inc.). Single carbon fibers were separated and cleaned by soaking in a boiling acetone bath for 10 min, followed by a boiling ethanol bath for 10 min, to remove any organics and contaminants from the fiber surface. The fibers were then rinsed in deionized (DI) water for 5 min and dried in a vacuum oven at 130 °C for 3 h.

For the single-fiber microbond experiments, microdroplets of the polymer-matrices (PMMA and epoxy) were added to the fibers. After cleaning and drying, the fibers were mounted horizontally on a custom frame and glued to a paper tab on one end of the fiber (Figure 4.1). The paper tabs facilitated the handling of the fibers and helped prevent slippage when mounting the samples on the grips of the tensile stage. The uncured polymer droplets were produced by mixing 1 g of hardener for every 4 g of resin. The uncured epoxy microdroplets were transferred onto carbon fibers by means of a fiber-to-fiber resin transfer technique using a "conveyer fiber" (Figure 4.1). A micro-pipet was used to add a droplet of resin on the conveyer fiber mounted on a paper frame. Next, the fiber was used to transfer the resin to the original specimen by bringing the fibers into perpendicular contact.

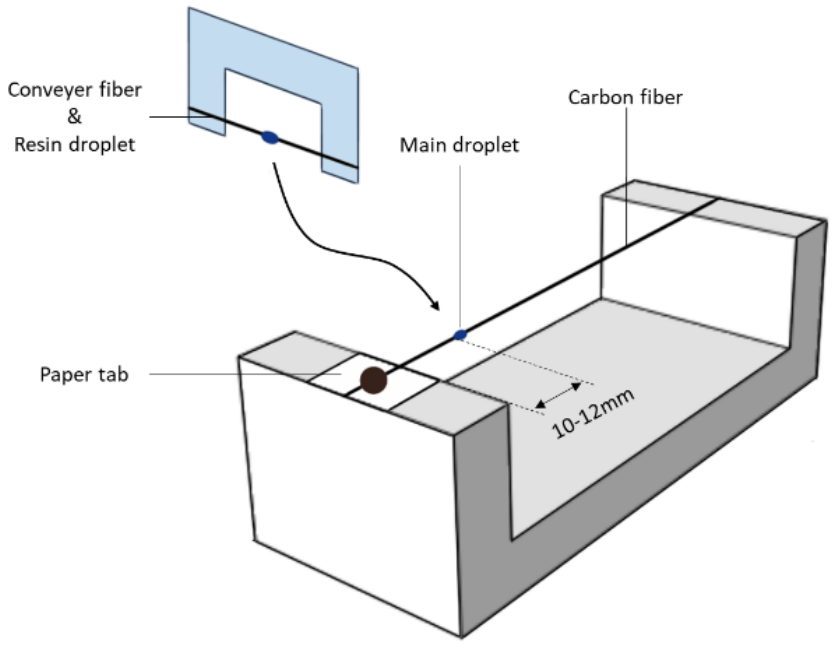

Figure 4.1: *A conveyer fiber was used to place the epoxy droplet onto the sample fibers, which were mounted on a custom frame with a paper tab attached at one end.*

The epoxy droplets were cured in a convection oven at 50 °C for 8 h and post-cured at room temperature for another 24 h. The droplets were observed in order to confirm that a symmetric geometry was obtained after curing, and the embedded lengths of the droplets were measured using an optical microscope. This technique produced consistent droplets with embedded lengths (L_{emb}) below 80 µm. Droplets that exceeded this L_{emb} threshold required shear forces to debond the interface that exceeded the ultimate tensile strength of the carbon fiber.

4.1.1.2 Kevlar®/PMMA

Unsized single Kevlar® 49 para-aramid fibers (JPS Composite Materials; average fiber diameter of 12.6 µm) were extracted, cleaned, and mounted horizontally onto a frame with paper tabs at the end, in the same manner as the carbon fibers. Polymethyl methacrylate (PMMA) thermoplastic, with an average molecular weight of 120,000 by gel permeation

chromatography (GPC), was used as the embedding microdroplet in this material system. A 3% wt PMMA solution was made by fully dissolving the PMMA powder in chloroform while stirring and heating to 70 °C for 10 min. After fully dissolving the PMMA, a droplet was placed on the Kevlar® fibers using the same fiber-to-fiber transfer technique. The chloroform solvent evaporates as soon as a drop is placed on the fiber, and the solidified PMMA does not immediately take the shape of an axisymmetric droplet. Therefore, the samples were heated to 200 °C for 2 h to allow the PMMA to melt and form into the desired droplet shape. Because the amount of polymer placed cannot be precisely controlled, some excess of PMMA may extend past the end of the droplet, forming a thin wetting layer. To remove this wetting layer, the fiber samples were submerged in chloroform for 3 min. This allowed the wetting layer to be fully etched without dissolving the PMMA droplet. The samples were then reheated to 200 °C for 1 h, and the final PMMA droplet shape was obtained. Droplets with embedded lengths greater than 250 μm resulted in the Kevlar® fibers breaking.

4.1.1.3 ALD Process

A custom-built, hot-wall, cross-flow thermal atomic layer deposition (ALD) reactor [28] was used for all ALD processes. Argon was used as the carrier gas for all ALD processes and was set with a flow rate of 70 sccm. For ALD of Al_2O_3, the ALD reaction chamber was heated to 130 °C, and the trimethylaluminum (TMA, Sigma-Aldrich) and water precursors were evaporated from stainless steel cylinders at room temperature. An ALD cycle for depositing Al_2O_3 films consisted of a 0.05 s pulse TMA followed by a 30 s argon purge and then followed by a 0.1 s pulse of water and 30 s more of argon purging. The average growth rate of Al_2O_3 on a Si wafer under these conditions was measured to be 1.31 Å/cycle using spectroscopic ellipsometry.

For ALD of ZnO, the precursor and chamber temperature, the flow rate of the carrier gas, and the precursor pulse times were the same as those used for Al_2O_3. Diethylzinc

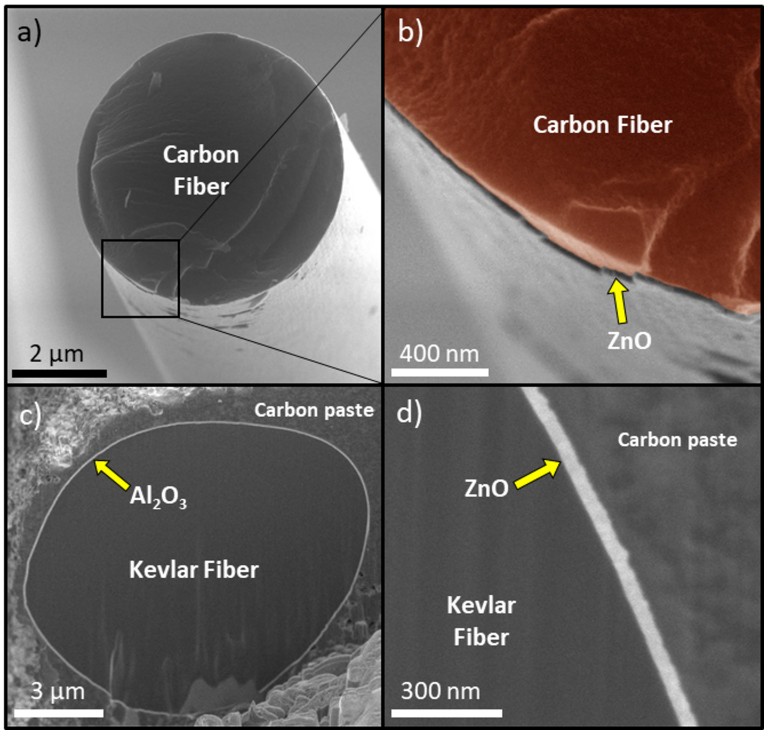

Figure 4.2: *(a) Low magnification and (b) high magnification SEM images of a carbon fiber coated with 20 nm of ZnO. (c) Low magnification SEM image of a Kevlar® fiber with 50 nm of Al_2O_3 and (d) high magnification SEM images of Kevlar® fiber coated with 50 nm of ZnO. All images show conformal coverage of the ALD coatings.*

(DEZ, Sigma-Aldrich) was used as the precursor. The growth rate of ZnO was measured to be 1.69 Å/cycle. The chamber temperature was 150 °C for the TiO_2 ALD processes. The carrier flow rates and precursor pulse times were the same as the previous two ALD processes. The tetrakis(dimethylamido)titanium (TDMAT, Sigma-Aldrich) precursor used for TiO_2 was heated to 75 °C. The growth rate for TiO_2 was measured to be 0.74 Å/cycle. The Kevlar® fibers and carbon fibers were coated after drying in the convection oven (during the cleaning process) and before placing the polymer droplets on the fiber surfaces. The ALD coatings conformally coated both carbon fibers and Kevlar® fibers (Figure 4.2), demonstrating the power of this technique for interfacial engineering of FRCs.

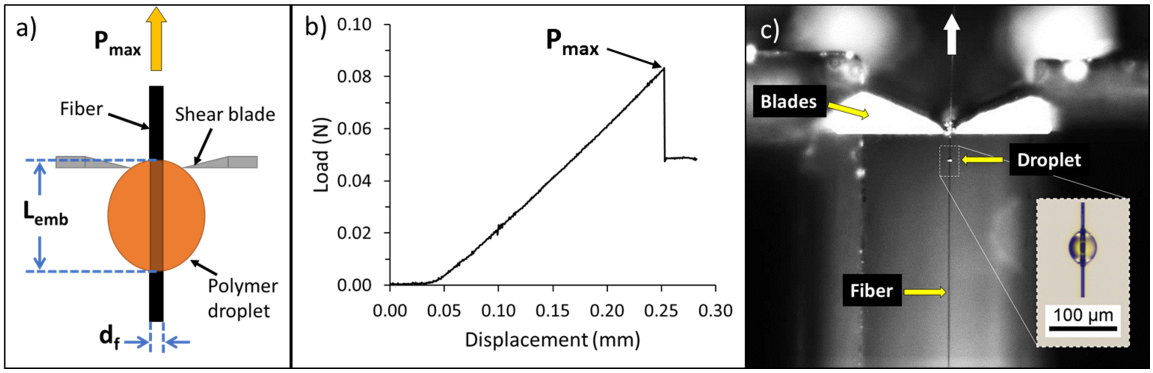

Figure 4.3: *(a) Schematic of the microbond method. (b) Representative load-displacement curve of a microbond test. (c) Image of an actual carbon fiber/epoxy sample mounted on the microvise, with shear blades in position and ready to be tested*

4.1.2 Microbond Test Setup and Procedure

The microbond test method was used to quantify the interfacial mechanical properties between a structural fiber and a polymer-matrix.[107–109] The method consisted of a micro-scale, axisymmetric polymer droplet that was placed on a single fiber, and then debonded by applying a shear force at the interface of the fiber-polymer (Figure 4.3a). This is an alternative procedure to the single-fiber pull-out test,[110–112] where very small embedded lengths (often in the micron scale) are necessary to avoid exceeding the ultimate strength of the fiber. The embedded length was defined as the geometrical length of the resin in the axial direction of the fiber, and the fiber-polymer interface area (A_{int}) is calculated as:

$$A_{int} = \pi d_f L_{emb} \tag{4.1}$$

where df is the nominal diameter of the structural fiber and L_{emb} is the embedded length. The interfacial mechanical properties were calculated from the interfacial area and the peak load at debonding (Figure 4.3b). A customized microvise setup, with position-adjustable shear blades, was designed and constructed to apply the shear load (Figure 4.3c).

The microbond test was performed with the custom microvise on an Instron 3345 universal testing machine equipped with a 10 N load cell. The paper tab region of

the droplet/fiber specimen was clamped in the upper grip attached to the displacement crosshead. The shear blade gap was adjusted by first bringing the razor blades into contact with the fiber and then retracting and adjusting the blade positions a specified distance. The blades were retracted approximately 2 μm from the contact position of the carbon fibers and approximately 5 μm from the contact position of the Kevlar® fibers. Accounting for the micrometer resolution accuracy of 2 μm, the blade gap was approximately 6–8 μm for carbon fiber/epoxy specimens and 15–20 μm for Kevlar®/PMMA specimens. The fiber was then pulled at a crosshead displacement rate of 0.05 mm/min, and the load was measured until an abrupt drop in the load was observed, signaling debonding of the polymer droplet. The peak load at the point of debonding was recorded and used to quantify the strength of the interface. Post-mortem analysis was performed using optical and/or electron microscopy to ensure that samples included in the data set failed at the interface and not due to cohesive fracture of the droplet.

It is common to report the interfacial shear strength as an average value under the assumption of a uniform shear distribution at the interface.[113,114] However, it is known that the shear stress distribution of the fiber-polymer interface is nonuniform during a microbond test.[109,113,115,116] To properly estimate the interfacial shear strength, an understanding of shear stress distribution at the interface would be necessary, requiring additional and extensive modeling. Variables such as fiber geometry, droplet size, razor blade position, and plasticity are parameters that need to be taken into account,[108,109,115,117,118] but these are often difficult to measure or control experimentally, requiring assumptions to be made that may introduce multi-variable uncertainties into the model. Therefore, in this work, the experimental data reported will not be referred to as an intrinsic mechanical property—instead, the data will be denoted as the "force to debond per unit interfacial area" (P_{max}/A_{int}).

4.1.3 Single-Fiber Tensile Tests of Kevlar® Fibers Exposed to Ultraviolet Radiation and Elevated Temperatures

The protection capabilities of ZnO coatings in Kevlar® fibers against elevated temperature exposure and ultraviolet (UV) radiation were studied. Tensile tests were conducted to evaluate the effects of temperature and UV light on the ultimate tensile strength (σ_{ult}) and work to failure *WF* of the fibers. The Kevlar® fibers were cleaned by the same method in section "Carbon Fiber/Epoxy", and the ALD conditions for ZnO were similar to section "ALD Process", except the precursors that were exposed for a longer period. One cycle of this ALD recipe consisted of a diethylzinc (DEZ) pulse time/additional DEZ exposure time/Ar purge/H_2O pulse time/additional H_2O exposure time/Ar purge, of 0.05 s/10 s/30 s/0.10 s/10 s/30 s. The samples were then exposed to UV radiation (of an intensity of 15 W/m_2) for 24 h or to temperatures of 300 °C for 8 h. The tensile properties of the Kevlar® fibers were tested using an RSA3 Dynamic Mechanical Analyzer (TA Instruments) following ASTM Standard C1557. The samples were pulled in tension at a constant displacement rate of 5 µm/s until the fiber failed, and ultimate tensile strength (σ_{ult}) and work to failure *WF* were recorded.

4.2 Results and Discussion

4.2.1 Kevlar® Fiber and PMMA

The box plot in Figure 4.4 shows the P_{max}/A_{int} results for the Kevlar® fibers and PMMA. The average P_{max}/A_{int} of uncoated Kevlar®/PMMA interfaces was 25.0 N/mm^2. The average P_{max}/A_{int} of Kevlar®/PMMA interfaces with coatings of 10 nm Al_2O_3, 10 nm TiO_2, 50 nm Al_2O_3, 50 nm TiO_2, and 50 nm of ZnO was 22.2 N/mm^2, 19.8 N/mm^2, 19.8 N/mm^2, and 20.9 N/mm^2, and 18.0 N/mm^2, respectively. The 50 nm ZnO coated samples exhibited the weakest P_{max}/A_{int} values with an average weakening of 28%, whereas the 10 nm Al_2O_3

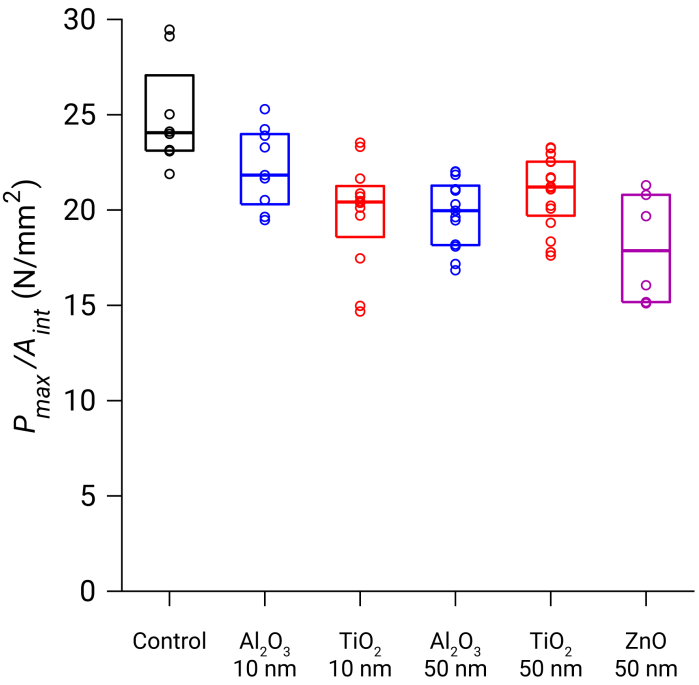

Figure 4.4: *Box plot of the force to debond per unit area of Kevlar®/PMMA samples with and without various ALD coatings.*

coatings had the least detrimental effects on the interface, weakening the interface by an average of 11%. These results demonstrate that ALD Al_2O_3, TiO_2, and ZnO coatings weaken the Kevlar®/PMMA interface, and the amount of weakening depends on both thickness and composition of the coating.

The results illustrate that nanometer-scale coatings of equal thickness, but different metal oxide composition, may result in significantly different interfacial mechanical properties. For example, the average P_{max}/A_{int} for coatings of 50 nm thick TiO_2 was 6% greater than the 50 nm Al_2O_3 coated Kevlar®, whereas fibers coated with 50 nm of ZnO were 11% weaker. Furthermore, the thickness of the ALD coatings also plays a role in influencing the mechanical properties at the interface. The average P_{max}/A_{int} for 10 nm thick Al_2O_3 coatings was 12% stronger than the thicker 50 nm Al_2O_3 coatings. The opposite trend is observed for TiO_2, where the average P_{max}/A_{int} for thinner 10 nm coatings was 5% weaker

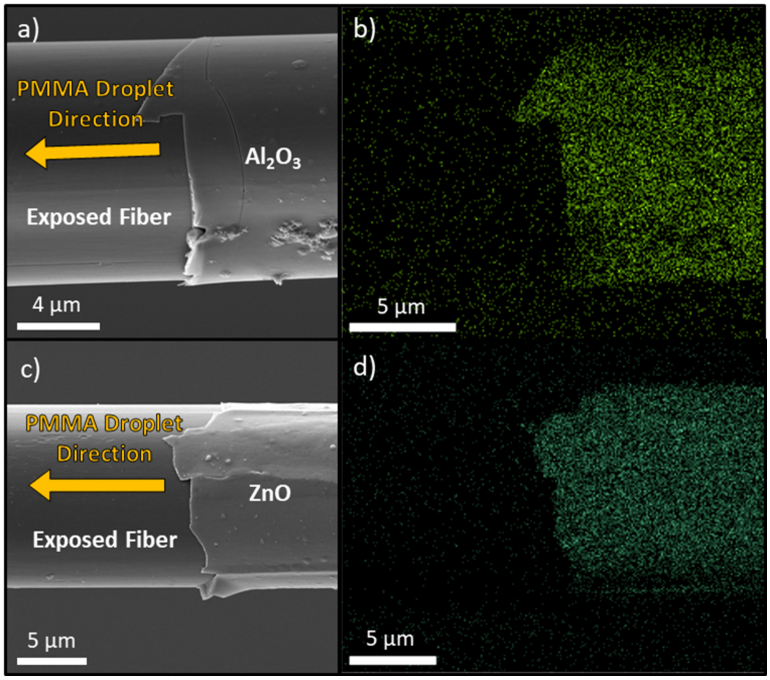

Figure 4.5: *(a) SEM image of a Kevlar®/50 nm Al_2O_3/PMMA sample after the microbond test. The Al_2O_3 coating is not present where the PMMA droplet used to be as confirmed by (b) the EDS elemental map of Al. (c) SEM image of a Kevlar®/50 nm ZnO/PMMA sample after the microbond test. Similar to the Al_2O_3 sample, the ZnO coating is not present where the PMMA droplet used to be as confirmed by (d) the EDS elemental map of Zn.*

than the thicker 50 nm TiO_2 coatings. These results highlight the importance of the material and thickness control of the coatings on the interfacial mechanical properties of the Kevlar®/PMMA interface.

SEM analysis was used to inspect the samples after the microbond experiments, in order to observe the morphology of the polymer droplets after they debonded from the fiber. The PMMA droplets pulled off cleanly from the Kevlar® fibers with no traces of PMMA residue, for the entire set of Kevlar®/PMMA samples (including the coated samples). Interestingly, the ALD coatings were also observed to delaminate from the Kevlar® surface in the original region where the droplet was bonded to the fiber (Figure 4.5). Both Al_2O_3 and ZnO coatings (50 nm thick) were absent in the original droplet position along the fiber surface after the microbond test (Figure 4.5a, c, respectively). EDS elemental mapping further confirms the absence of Al_2O_3 and ZnO coatings in the debonding region (Figure

4.5b, c, respectively).

These post-mortem observations suggest that the PMMA adheres more to the ALD coatings than the coatings adhere to the fiber. We therefore hypothesize that if the strength of adhesion between the ALD coatings and the Kevlar® fibers could be enhanced, the P_{max}/A_{int} could potentially reach or even surpass that of the bare Kevlar®/PMMA. Chen et al.[5] showed that the interfacial toughness was lower when delamination occurred at the ALD/polymer beam interface than when it occurred at the ALD/epoxy interface. This also indicates that control of the interface (fiber/ALD or ALD/epoxy) at which crack-propagation occurs can have a significant impact on debonding force. Future work dedicated to modification of the interfacial chemistry between ALD coatings and the Kevlar® fibers would help identify surface treatments that could promote stronger or weaker adhesion, depending on the targeted application.

4.2.2 Carbon Fiber and Epoxy

The P_{max}/A_{int} was also evaluated for the material combination of carbon fiber and epoxy (Figure 4.6). The average interfacial P_{max}/A_{int} of bare and 20 nm ZnO coated carbon fibers with epoxy was 52.6 and 41.2 N/mm^2. Similar to the microbond results of the Kevlar®/PMMA material system, the average P_{max}/A_{int} of the 20 nm ZnO coated carbon fibers/epoxy weakened by 21.7% as compared to the bare fibers/epoxy. These results demonstrate that ALD coatings can impact a range of fiber-matrix combinations, and provide motivation for a deeper understanding of the coupled chemical-mechanical properties of ALD-modified FRC interfaces.

4.2.3 Statistical Significance Analysis

Statistical analysis was conducted to confirm that ALD coatings have a measurable effect on the average weakening of the P_{max}/A_{int}. The statistical significance of the P_{max}/A_{int} measurements for coated fibers was evaluated against the fibers without coatings, using a

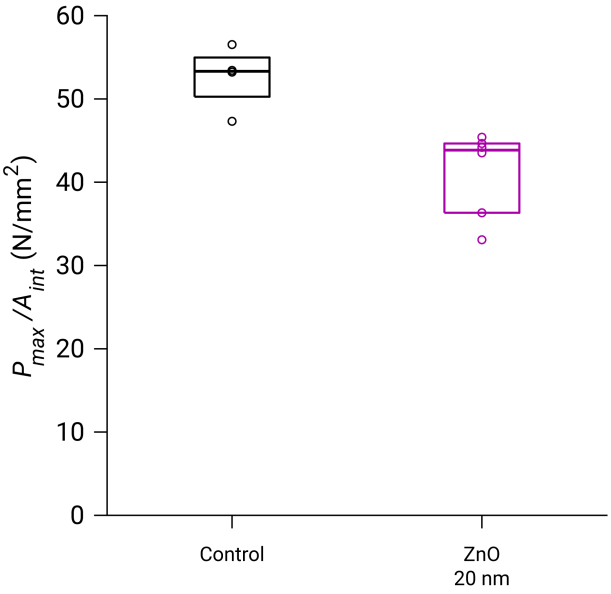

Figure 4.6: *Box plot of the force to debond per unit area of carbon fiber/epoxy samples with and without 20 nm ZnO coatings.*

one-tailed t-test. The null hypothesis for this test is that ALD coatings on the fiber-polymer interface have no direct effect on the $P_{\max}/A_{\text{int}}$ values obtained. The null hypothesis will be rejected if the p-value is less than 0.05 (confidence interval of 95%). The calculated p-values for each ALD coating and material system are listed in Table 4.1. The significance level criteria previously established are met for all coatings and material systems, and thus, the null hypothesis is fully rejected, supporting the conclusions that the ALD coatings can systematically modify interfacial mechanical properties.

4.2.4 Ultraviolet and Thermal Protection

In addition to modification of mechanical properties of fiber-matrix interfaces, coatings are often used on fiber surfaces to protect them during composite materials processing. Coatings may also be used to protect a composite from environmental conditions. Polymers often experience effects of degradation when exposed to extreme radiation or temperatures,

Table 4.1: *t-test results of the statistical significance of the P_{max}/A_{int} from Figs. 4 and 6*

COATING	*t*-SCORE	DEGREES OF FREEDOM	*p*-VALUE ($p < 0.05$)
Kevlar®/PMMA			
10 nm Al_2O_3	2.2840	15	0.0187
10 nm TiO_2	4.0115	18	0.0004
10 nm TiO_2	4.0115	18	0.0004
50 nm Al_2O_3	4.6399	22	0.0006
50 nm Al_2O_3	4.6399	22	0.0006
50 nm TiO_2	3.6861	12	0.0004
Carbon fiber/epoxy			
20 nm ZnO	4.0030	8	0.0020

which can often limit their use. Coatings that can protect a polymer-matrix or polymer fiber from these detrimental effects would enable the use of polymer composites in wider range of applications.

The ability of ALD ZnO coatings to protect Kevlar® fibers from ultraviolet (UV) radiation thermal degradation was evaluated by measuring the ultimate tensile strength (σ_{ult}) and the *WF* of the fibers (Figure 4.7). UV light exposure, of an intensity of 15 W/m^2 for 24 h, reduced the average σ_{ult} of uncoated fibers by 24% and the average *WF* by 46%. Furthermore, uncoated fibers that were exposed to an ambient temperature of 300 °C for 8 h experienced a decrease in σ_{ult} by 30% and a decrease in *WF* by 46% (Figure 4.7). In contrast, Kevlar® fibers with a 50 nm coating of ZnO by ALD had a negligible change in the average σ_{ult} (0% difference) and the average *WF* (2% lower) after the same UV treatment. Similarly, Kevlar® fibers with the ZnO coatings reduced the impact of thermal degradation in the average σ_{ult} (12% weaker) and increased the average *WF* (11% higher). It is also evident that the ZnO coatings did not influence the average σ_{ult} significantly (3% stronger), but did slightly increase the average *WF* (11% higher). The UV protection capabilities shown here are consistent with previous work from Azpitarte et al.[106]

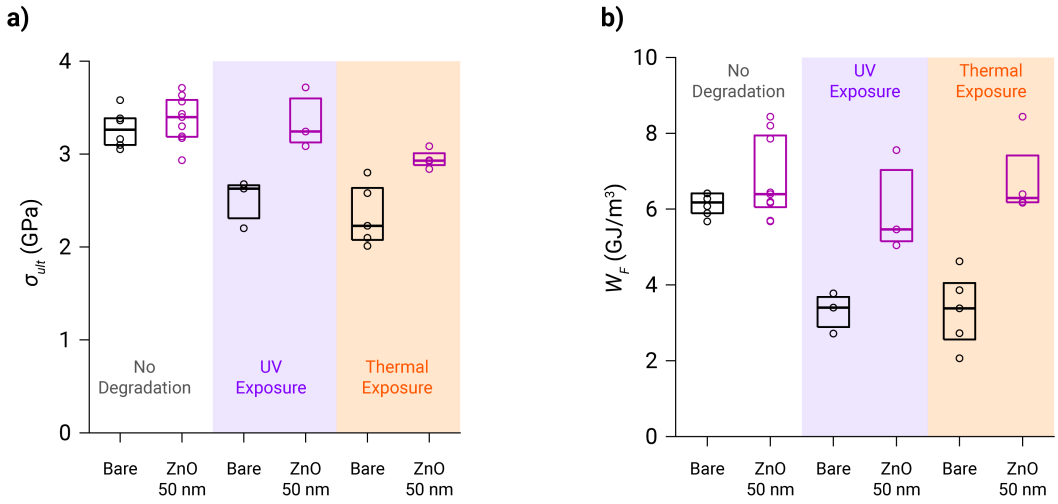

Figure 4.7: *(a) Ultimate tensile strength (b) and work to failure of the Kevlar® fibers exposed to ultraviolet radiation and 300 °C temperatures, with and without 50 nm ZnO coatings by ALD, were obtained.*

4.3 Conclusion

Understanding the interfacial properties is crucial to predict the overall mechanical properties of FRCs. The ability to tune the interfacial properties, not only in PMCs but also CMCs, presents an opportunity to develop engineered structural composite materials designed with specific macroscopic mechanical properties. In this study, we explored the effects ALD coatings have on the interface of two distinct fiber-polymer material systems. We demonstrated ALD can conformally coat Kevlar® fibers and carbon fibers with sub-nanometer thickness control, and that this level of thickness control can influence the interfacial properties of both material systems (Kevlar®/PMMA and carbon fiber/epoxy). Furthermore, we showed that the mechanical response of ALD coated fibers depends on coating thickness and composition. It was observed that the ALD coatings preferentially delaminated from Kevlar® fiber surfaces, indicating that the adhesion of the coatings to the matrix was higher than the adhesion of the coatings to the fiber surfaces. Functionalization of the fiber surfaces, such as electrochemical oxidation or plasma treatments, presents an opportunity to

further enhance the adhesion between the coatings and fibers.

Finally, it was demonstrated that ALD coatings could be used to impart additional benefits beyond tuning interfacial bonding. As a proof-of-concept, we showed that deposition of 50 nm of ZnO by ALD can protect Kevlar® fibers from ultraviolet light degradation and thermal degradation. This model material system demonstrates that ALD coatings could enable opportunities to produce multifunctional composites, bringing forth an exciting new field of research and development.

Chapter 5

Multifunctional Polymer-Matrix Composites: Electrically Conductive Kevlar Fibers by Atomic Layer Deposition

Fiber-reinforced composites (FRCs) are low-density materials that have been widely used as structural components in high-performance automotive and aerospace vehicles. FRCs can be designed to have a high specific strength, stiffness, and/or toughness, and their lightweight characteristics can offer significant improvements in performance and fuel efficiency. Over the past two decades, a variety of multifunctional composites have been developed[119] including structural batteries and supercapacitors[120,121] structural health monitoring,[122,123] structural electronic devices,[124] electromagnetic interference shielding,[125,126] and self-healing materials.[127–129] Imparting additional functionality to FRCs while maintaining their lightweight and structural qualities is highly desirable to save space and augment the performance of automotive and aerospace vehicles.[130]

To enable multifunctionality in FRCs, there is a need to modify non-structural properties such as thermal and electrical conductivity. This is often achieved through the inclusion of additives or coatings. For example, to design FRCs that also function as an electronic device, constituents with electrically conducting and semiconducting qualities are necessary. However, polymer-matrix composites (PMCs) are generally electrically insulating, which often necessitates the inclusion of electrically conductive additives. For FRCs, rein-

forcements that are intrinsically conductive, such as carbon fibers, may be used. However, restricting the materials selection to intrinsically conductive fabrics may significantly limit the material design flexibility. For example, while the conductance of a carbon-fiber reinforced PMC can be increased by increasing the volume fraction of the fibers, this also impacts its density, stiffness, and strength. In composites where all constituents are electrically insulating, a common strategy to impart conductivity is to mix electrically conductive additives such as carbon black,[131–133] graphene,[134,135] or carbon nanotubes[136,137] into the matrix. However, such additives tend to affect the bulk mechanical properties and density of the final product,[138–140] which may not be desired. Furthermore, the distribution of these additives may not be uniform in composites that use braided/woven fabrics, resulting in inhomogeneous mechanical and electrical properties.[137] Therefore, there is a desire to decouple the electrical response of the composite from its mechanical properties, enabling improved control of materials by design.

A potential method to tune electrical conductivity without significantly affecting stiffness, strength, and density is to modify the surface of the reinforcement with a thin, uniform, and conformal conductive coating before incorporation into the matrix. Chemical vapor deposition (CVD)[141–143] and electrophoretic deposition[144] have been explored as methods for coating fabrics. However, many thin-film deposition methods suffer from tradeoffs between conformality, uniformity, and precise thickness control at the nanoscale, especially when coating 3-D topologies with high aspect-ratios. This highlights the need for coating processes that maintain precise control and tunability of thickness and composition when coating fibers, tows, and fabrics that are used in PMCs.

Among the potential thin-film deposition techniques, atomic layer deposition (ALD) provides unparalleled conformality with sub-nanometer resolution in material thickness and composition, which are ideal characteristics when coating complex 3-D topologies such as woven fabrics.[43,85–89] ALD is a vapor-phase deposition technique that utilizes two or more precursors that react with the substrate in a self-limiting manner that is not line-

of-sight dependent. The precursors react in sequential steps, allowing for precise tuning of film thickness and composition. Additionally, a wide range of materials can be deposited using ALD,[96] including ceramics, metals, and polymers. This broad materials selection allows for the design of materials with specified properties, representing a powerful method for incorporating multifunctionality into composites.[98] Previous works have demonstrated that ALD can conformally coat fibers,[145–148] and that they can be made conductive.[149–151] Furthermore, the effects interconnected fibers in woven[152] and non-woven fabrics on their conductive properties have been studied.[153] However, the use of ALD to impart electrical conductivity into PMCs has not been previously studied, which represents an important step towards multifunctional composites by design. Moreover, there is a need to quantify the coupled mechanical and electrical behavior of these multifunctional PMCs under applied loads, in order to identify the design constraints and criteria for co-optimization of their functional and structural properties.

In this work, we use ALD to impart electrically conductivity onto Kevlar® 49 (K49) woven fabrics by coating them with aluminum-doped zinc oxide (AZO). AZO was selected as the coating material because it has a low electrical resistivity ($\sim 10^{-3}$ Ω-cm)[154,155] and can be deposited at relatively low temperatures (< 150 °C), which minimizes physical damage to the K49 fabric. The conductive properties of the coated fabrics were measured as a function of ALD film thickness at the single fiber, single tow, and woven fabric levels. The trends in thickness-dependent conductivity were explored with scanning electron microscopy/focused-ion beam (SEM-FIB) analysis. The coated fabrics were integrated into PMCs with an epoxy matrix using a vacuum-assisted resin transfer molding (VARTM) process.[156] The mechanical properties of the PMCs were evaluated, and their multifunctional properties were characterized through in situ measurements of electrical conductivity during tensile testing. The change in electrical response with increasing strain was analyzed, which was described with a fracture mechanics model. The results of this study highlight the importance of precise thickness control and conformality in the coating of multifunc-

tional composites, and explore the role of thin-film mechanics in controlling the limits of functional interlayers under applied loads.

5.1 Experimental Methods

K49 fabrics in a 351-style plain weave (JPS Composite Materials, Corp.) were used for this study. The single fibers, single tows, and woven fabric samples were extracted and cleaned as described in Appendix A. A custom-built, hot-wall, crossflow atomic layer deposition (ALD) reactor[155] was used. The precursors were diethylzinc (DEZ, 52 wt.% Zn, Sigma-Aldrich), dimethylaluminum isopropoxide (DMAI, 98% (99.99+/-Al), Strem Chemicals, Inc.), and deionized water. The ALD reactor was heated to 130 °C, the DMAI source was heated to 65 °C, and the DEZ and water were kept at room temperature. Argon (99.999% purity) was used as the carrier gas at 70 sccm. The recipe for AZO coating consisted of repeating a sequence of precursor-A/argon/precursor-B/argon. For the ternary AZO growth, this sequence represents a "subcycle", which is integrated into a "supercycle" recipe. The ratio of $ZnO:Al_2O_3$ subcycles within a supercycle controls the final Zn:Al ratio in the ALD film.[155] DEZ and DMAI are precursor-A for their respective subcycles and precursor-B uses DI water for both cases. The time sequence for both subcycles was 0.05 s/45 s/0.10 s/ 45 s. One supercycle consisted of a ratio of 15:1 DEZ:DMAI subcycles. The average growth rate of AZO on Si wafers was measured to be 29.6 Å/supercycle or 1.9 Å/cycle using spectroscopic ellipsometry. The total number of supercycles was adjusted in each run to achieve a targeted AZO thickness between 40-200 nm. Scanning electron microscopy (SEM), x-ray photoelectron spectroscopy (XPS), x-ray diffraction (XRD) were used to confirm the composition and phase of the AZO coating on the K49 fabrics (Figures A.1-A.1). After coating the K49 single fibers, tows, and fabrics to specified thicknesses, their electrical resistance was measured with an SP-200 Biologic potentiostat using a four-point probe[157] (details in Appendix A).

Single-ply PMCs were manufactured using the vacuum-assisted resin transfer molding (VARTM) method (details in Appendix A). The matrix polymer was a bisphenol A, low-viscosity epoxy resin (R-3501, Composite Envisions, LLC) and hardener (H-5000-01, Composite Envisions, LLC). VARTM was performed at room temperature and the epoxy was set for 36 hours to ensure proper curing. Composite strips with in-plane dimensions of 11 mm × 140 mm were prepared for tensile testing, and tabs were added per ASTM standard D3039/D3039M. Tabs were added to the sample per ASTM D3039/D3039M. In order to contact the conductive fibers at the ends of the composite, silver paste was applied to exposed ends of the fabric, as described in Appendix A.

The composites were loaded in tension while measuring the electrical current in situ with a constant applied voltage of 5V. The tensile stage used was an Instron 4301 with a ±10 kN load cell (2525-804, Instron) and custom-made grips. The major principle strain (ε_{11}) in the sample was measured by 3-D digital-image correlation (DIC),[158–161] using Vic-3D 7 software (Correlated Solutions, Inc.) and two machine-vision cameras (GRAS 50S5M-C, Point Grey) with 75 mm lenses (HF75SA-1, Fujinon) and 10 mm extension tubes (Figure A.6). A speckle pattern was painted on the sample for DIC (Figure A.7) by air-brushing black paint speckles (carbon black color, Golden, Inc.) over a white paint background (titanium white color, Golden, Inc.). A schematic of the prepared sample can be found in Figure A.8.

5.2 Results and Discussion

The targeted thicknesses of the AZO coatings on K49 was 80 nm, 120 nm, 160 nm, 200 nm. This was in close agreement with the measured thicknesses of 83 nm, 119 nm, 158 nm, 192 nm using spectroscopic ellipsometry on adjacent Si pieces. These measurements were also consistent with SEM-PFIB cross-sectional analysis of the coated fibers. The AZO coatings uniformly coated the entire surface of the exposed K49 fibers (Figure 5.1a

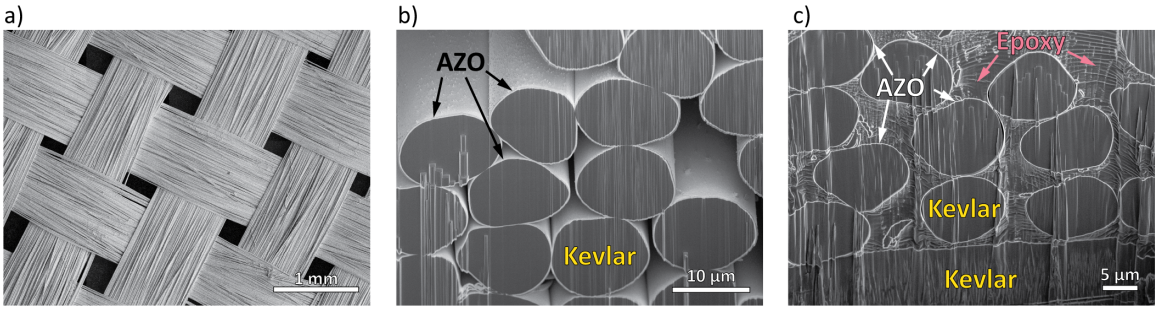

Figure 5.1: *SEM of a) top-down view of K49 woven fabric coated with 200 nm of AZO, b) SEM-FIB cross-section of K49 fabric coated with 200 nm of AZO, and c) of 120 nm AZO-coated K49 fabrics embedded in epoxy after VARTM.*

and Figure 5.1b). This illustrates the utility of ALD to enable conformal coatings with precise control of thickness on three-dimensional, high-surface-area fiber substrates with overlapping geometries. Furthermore, the coating is preserved after embedding the fibers in an epoxy matrix via VARTM (Figure 5.1c), demonstrating the applicability of this approach for interfacial engineering of PMCs.

The average resistivity of planar AZO films deposited on glass was measured to be 2.3 mΩ-cm with a standard deviation of +/- 0.4 mΩ-cm using a four-point probe,[157] which is considered to be a material property of the coating. However, for the application of ALD coatings in multifunctional fabrics and composites, it is also meaningful to measure an effective resistivity,[162–165] based on the total cross-sectional area of the coated sample. The effective resistivity for single fibers, tows, and fabrics was calculated using Equation 5.1:

$$\rho_e = R\frac{A_{eff}}{s} \tag{5.1}$$

where R is the experimentally measured resistance, A_{eff} is the effective cross-sectional area (area of AZO coating plus substrate), and s is the probe spacing (s = 12 mm). The values of A_{eff} for single fibers (A_{fib}), tows (A_{tow}), and woven fabrics (A_{fab}) are provided in Appendix A.

The measured values of effective resistivity can be compared to a theoretical limit,

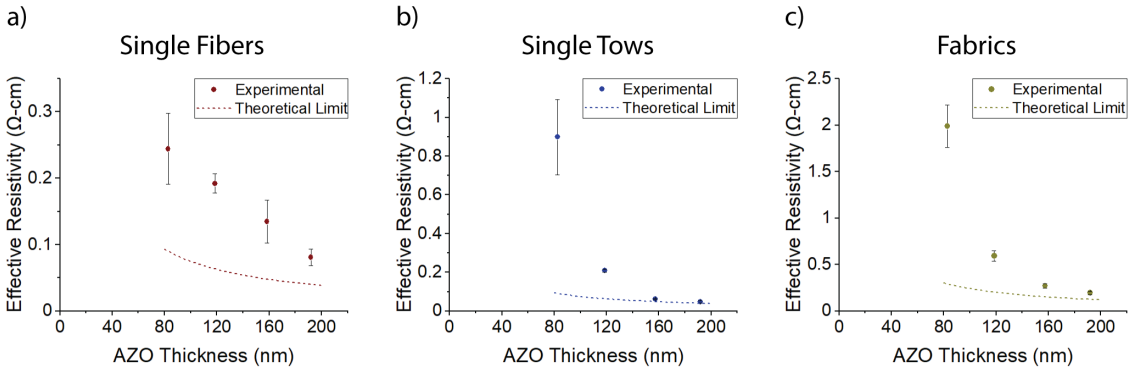

Figure 5.2: *The experimental resistivity (ρ_e) and theoretical limit of resistivity (ρ_t) for a) single fibers, b) tows, and c) fabrics coated with varying thicknesses of AZO.*

which would be the expected value if all of the coated surfaces in the 3-D geometry fully contribute to electrical conduction. The theoretical limit of effective resistivity is thus defined by Equation 5.2:

$$\rho_t = \rho_{AZO} \frac{A_{eff}}{A_{AZO}} f_L \tag{5.2}$$

where ρ_{AZO} is the measured resistivity of planar AZO films, A_{AZO} is the cross-sectional area of only the AZO coating, and τ_f is a tortuosity factor that considers the fact that in a woven fabric, the total length of the individual fibers is longer than the fabric length, because of the waviness of the weave. The τ_f for the fibers and the tows was 1, and the τ_f of the woven fabric was estimated to be 1.006 based on the weave geometry.

The measured ρ_e values for the fibers, tows, and fabrics as a function of AZO thickness are shown in Figure 5.2. For all three sample geometries, the average ρ_e monotonically decreases as the thickness of the coating increases. This is expected, because AAZO increases as the ALD coating thickness increases.

As observed in Figure 5.2a, deviations between ρ_e and ρ_t for the single fibers are observed. We hypothesize that this deviation is a result of microscopic cracks or flaws present in the coating along the fiber length, which likely form during the sensitive handling of single fibers. The theoretical limit assumes the ALD coating to be a perfectly continuous shell. Therefore, any microscopic flaw, such as a crack, will result in a "bottleneck" for

local current flow (Figure A.9), increasing the measured resistance. When the thickness of the coating was further reduced to 40 nm, an order-of-magnitude increase in ρ_e was observed. Therefore, 80 nm was chosen as the minimal thickness to achieve sufficiently low electrical resistivity in this study.

The tows exhibit a similar trend of decreasing ρ_e with increasing ALD film thickness. As the thickness increases, ρ_e converges to ρ_t (Figure 5.2b). However, for thinner coatings, the deviation between ρ_e and ρ_t increases substantially. For example, the tows coated with 158 nm and 192 nm of AZO exhibit a percent difference of 24.3% and 15.7%, respectively (further details in Appendix A). Comparatively, the percent difference for the tows coated with 83 nm of AZO was almost 900%.

The dependence of ρ_e on thickness for the tows can be rationalized by considering the interconnectivity of adjacent fibers in the tow. This interconnected network between adjacent fibers in a tow allows for additional charge pathways and improved percolation, which reduces the resistivity of the sample. In the limit that all fibers within the tow fully contribute to the conductance, ρ_e converges to ρ_t. The interconnectivity between fibers can be visualized using SEM-FIB imaging (Figure 5.3a-b). Figure 5.3a shows a FIB cross section of multiple adjacent fibers within a tow, where the ALD shell merges and forms contact points. Figure 5.3b shows a region of a shell in a fiber that had detached from an adjacent fiber during handling. Grooves along the longitudinal direction are associated with prior line contacts between two cylindrical fibers, and a local delamination is visible along one of the groves, indicating that the continuous ALD shell detached when the adjacent fiber was removed.

Thicker AZO coatings will facilitate a higher number of bridged connections, enhancing percolation, and improving the conductive properties of the coated tows. Furthermore, thicker coatings are more likely to have a larger bridged contact area for each connection point (Figure 5.3c-d), which would reduce the contact resistance between adjacent fibers. These bridged connections between fibers will also make the conductive pathway more

"defect tolerant", because if a bottleneck to current flow (such as a flaw in the ALD coating) exists along a single fiber, the current can follow a parallel pathway. This can help to rationalize the observation of improved agreement between ρ_e and ρ_t for thicker coatings (160-200 nm) in the tows (Figure 5.2b) compared to the single fibers (Figure 5.2a). A quantitative comparison of the percent difference for single fibers, tows, and fabrics with varying thicknesses is provided in Table A.1.

In addition to the fiber-fiber contact resistance, another factor that will influence the experimentally-measured ρ_e is the contact to the metal electrodes used for the electrical resistance measurements. To form a metal contact in this study, silver paint was applied to the fibers, tows, and fabrics. While the liquid paint can diffuse into larger voids between fibers, interior fibers in the tows and fabrics will rely on fiber-to-fiber bridged connections in order to contribute to the overall conductive network (Figure A.10). The metal contact does not directly contact each individual fiber, which amplifies the deviation between ρ_e and ρ_t with decreasing thickness. because only those fibers within the network that have a pathway to the electrode will contribute to conduction. Thicker coatings increase the probability and number of sites with bridged connections, which increases the interconnectivity within the tows and fabrics. This further highlights the importance of the electrical contact in manufacturing multifunctional composites where the functional layer is confined to the interphase region.

Similar trends to those observed for the individual tows were observed in the resistivity data for the woven fabrics (Figure 5.2c). As the coating thickness increases, the measured ρ_e values converge to the theoretical limit. For example, the difference between ρ_e and ρ_t for the fabrics coated with 158 nm and 192 nm films was 64.8% and 44.7%, respectively. Once again, owing to the percolation effects described above, these values are closer to the theoretical limit than the corresponding values for single fibers. However, in addition to the improved percolation within a tow, for the woven fabric, there are also tow-to-tow contact regions that overlap between the longitudinal and transverse weave directions.

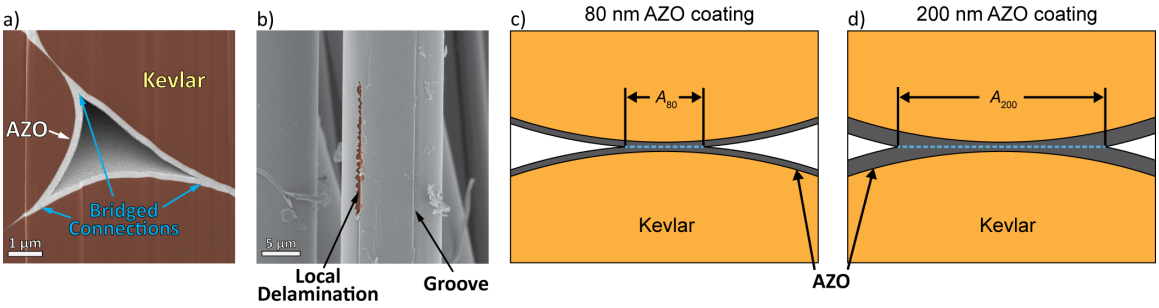

Figure 5.3: *a) SEM-FIB imaging of three parallel K49 fiber coated with 200 nm of AZO with bridged connections, and b) a top-down view of a K49 fiber coated with 120 nm of ZnO after merged parallel fibers detached (orange false color added to highlight exposed surface of K49 fibers). c) Schematic of K49 fibers with bridged AZO coatings 80 nm and d) 200 nm thick that are equally spaced.*

Overlapping, perpendicular fibers that contact one another also contain bridged AZO connections, as confirmed by SEM imaging (Figure A.11). Because of this overlapping geometry, the electrical current may follow multiple paths. For simplicity, one of the assumptions made for the theoretical limit (ρ_t) of the fabrics was that only longitudinally-aligned tows (0° direction) contribute to the resistance, whereas the transversely-aligned tows (90° direction) did not. This is a reasonable assumption because the contacts were formed such that the applied voltage was along the longitudinal direction, which explains the good convergence between the experimental and theoretical values in this study. However, as the complexity of the fabric network increases (such as non-orthotropic weaves), electrical transport within the fabrics will be determined by a weighted statistical distribution over all possible charge paths.

In addition to the fabrics, the conductive properties of PMCs were analyzed after embedding the coated fabrics in an epoxy matrix via the VARTM process. The ρ_e of the composites follows the same trend that was observed with the woven fabrics up to 160 nm, indicating that the electrical properties were preserved after fabrication (Figure 5.4). The 200 nm thick sample exhibited a slight increase in the average and standard deviation of effective resistivity, which we attribute to minor damage of the coating, as a result of slight bending during the handling process after fabrication. The single-ply composite (which

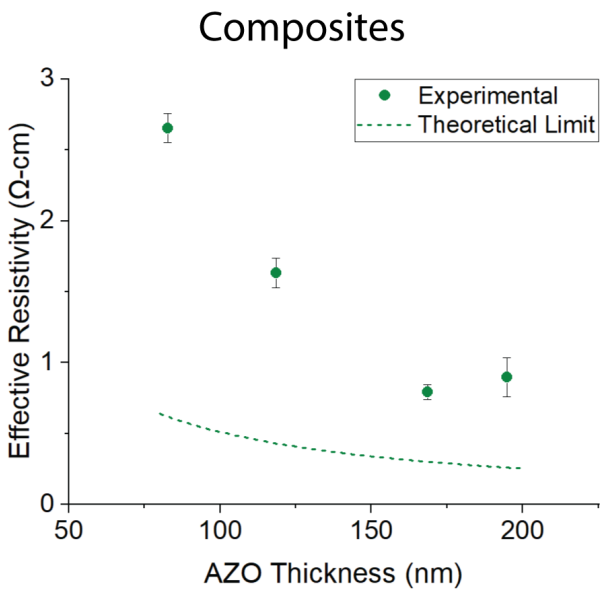

Figure 5.4: *ρ_e and ρ_t values for fabricated composites using fabrics coated with different thicknesses of AZO (calculated using Equation 5.1 & 5.2, where s = 114 mm).*

is approximately 0.2 mm thick) is prone to bending during manufacturing. As a consequence of this bending strain, thicker coatings are more likely to fracture, which leads to the slightly higher variation in ρ_e observed. The relationships between thickness of the coating and its fracture behavior will be discussed in further detail below. Overall, the electrical conductivity imparted by the coatings was preserved after the VARTM process, which is consistent with cross-sectional SEM analysis (Figure 5.1c).

To study the mechanical response of the ALD-modified composites, the samples were mechanically loaded in tension until failure. This allowed for a determination of the impact that the coatings had on the bulk stress-strain response (Figure 5.5). The samples all fractured within the gauge region. In the uncoated sample, a slight non-linearity was observed in the stress-strain response, where the modulus increases with increasing strain up to $\sim$2.0%, after which linear-elastic behavior is observed. This "tension-stiffening" effect may be attributed to straightening of the woven fibers in the longitudinal direction under applied tension. In contrast, the coated composites exhibit a linear-elastic response above

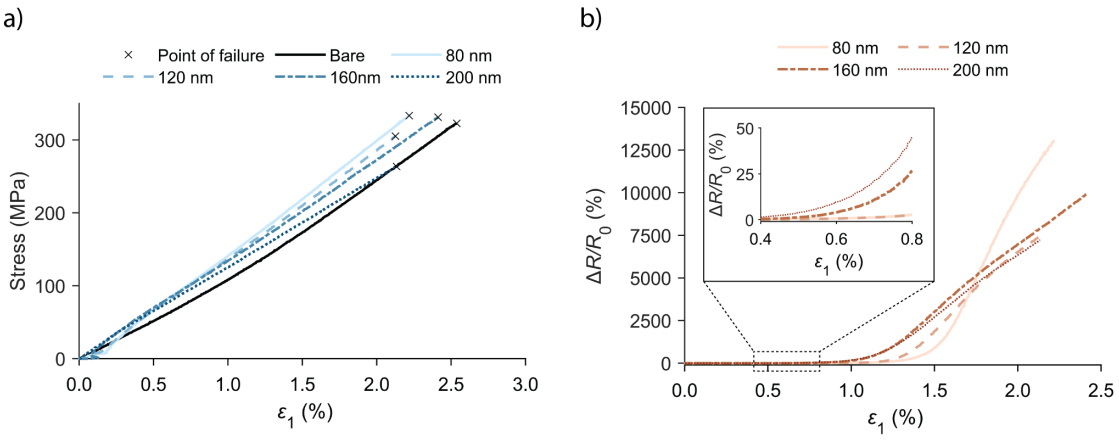

Figure 5.5: *a) Stress-strain curves and b) $\Delta R/R_0$-strain curves for K49-epoxy composites with varying thicknesses of AZO coatings on the K49 fabrics.*

$\sim$0.4% strain. We hypothesize that the AZO coatings may contribute to this improved linearity at lower strains as a result of the bridged connections, which could increase the shear resistance and restrict the sliding of the fibers. In general, the modulus was consistent among all of the samples, with minimal variation as a function of coating thickness. Furthermore, the experimental stress-strain response from these experiments was within a consistent range of expected modulus values, which was based on the fiber volume fraction ($\sim$0.25-0.30) and moduli of K49 (112 GPa) and epoxy (1.26 GPa). Moreover, no clear correlation between the AZO thickness and the ultimate tensile strength or ultimate tensile strain were observed. These results demonstrate that ALD is an effective means of imparting multifunctionality into PMCs, which can be achieved without deleterious effects on their bulk mechanical properties.

The *in situ* electrical response of the PMCs as a function of applied strain was also studied. A significant change in the measured electrical resistance was observed under increased tensile loading (Figure 5.5b). This change was quantified according to Equation 5.3:

$$\frac{\Delta R}{R_0} = \frac{R\left(\varepsilon_{11}\right) - R_0}{R_0} \tag{5.3}$$

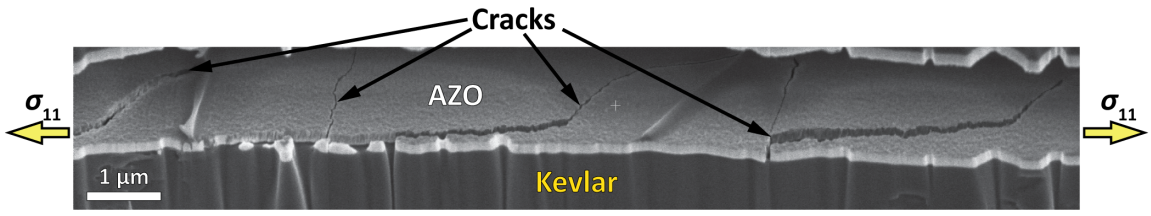

Figure 5.6: *Post-mortem SEM cross-section of a composite loaded to failure, with K49 fabric coated with 120 nm of AZO. The load was applied horizontally with respect to the plane of the image. (Selective adjustments of contrast and brightness were done to highlight the cracks).*

where $R(\varepsilon_{11})$ is the measured resistance as a function of strain, and R0 is the initial resistance at a strain value of zero.

$\Delta R/R_0$ was observed to increase as the principal strain ($R(\varepsilon_{11})$) increased (Figure 5.5b). To investigate the origins of this increase in resistance, post-mortem SEM-FIB imaging was performed. Figure 5.6 shows a FIB cross-section of an exposed ALD coating on a fiber surface, where the tensile load was applied in the horizontal direction (along the fiber axis). Channel cracks in the coating are observed, which primarily occur along the circumference of the fiber (perpendicular to the applied load). We attribute the increased resistance under tension to the formation of these cracks, which impede current flow and decrease the number of continuous charge pathways. However, the composite can maintain some of its conductivity even after cracks have formed, because the bridged connections between the fibers enables alternative pathways for current flow throughout the interconnected network.

The impact of crack formation in the coating on electrical transport within the composite is illustrated in Figure 5.7. According to the principles of thin-film fracture mechanics, when the critical stress for the onset of fracture is reached within the coating, crack formation will initiate.[166,167] As strain continues to increase, additional cracks will form, which further disrupts the electrical conduction pathways.[168]

To provide a qualitative visual-aid of these trends, a 3-D model was developed using COMSOL Multiphysics (Figure 5.7). The model is simplified, using only five fibers aligned along a plane. The applied voltage at the boundaries was consistent among the three panels.

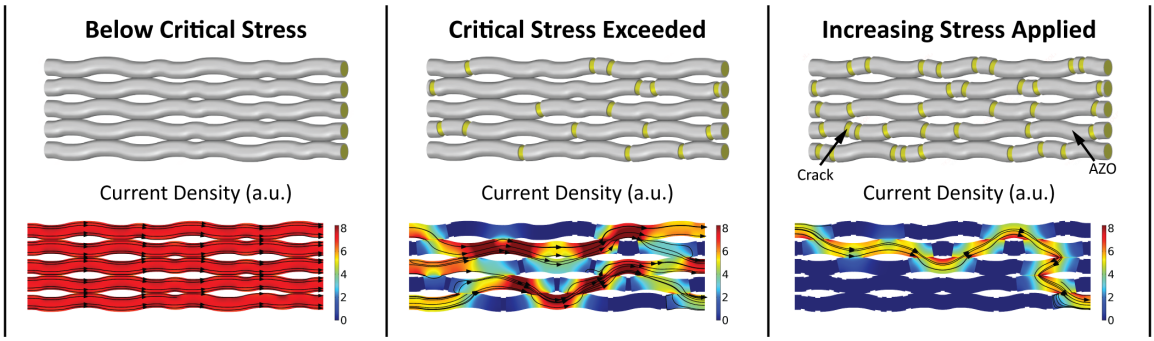

Figure 5.7: *Schematic illustration and associated COMSOL model for qualitative visualization of charge pathways within a simplified tow of five fibers (not to scale). Left, a representative behavior of a coated fabric with no applied load; middle, as the load increases and cracks begin to form in the coating, the path of least resistance will be facilitated by alternative pathways through bridged connections between fibers, resulting in an increase in resistance; right, upon further loading, an increased density of cracks will result in fewer viable conductive paths, increasing the tortuosity of viable charge pathways and the associated resistance.*

On the left panel of Figure 5.7, before the onset of cracking, the current flows uninterrupted along the continuous coating. As cracks begin to form, the electrical resistance of the individual fibers increases. In the extreme case where a circumferential crack completely isolates two sections of the coating, the current flow through an individual fiber will halt. As a consequence of these increases in the resistance of individual fibers, the path of least resistance through the fiber network will evolve. Specifically, bridged connections between adjacent fibers are required to provide alternative pathways.

As the number of cracks grows under increasing stress, the number of possible pathways will continue to decrease resulting in a monotonic increase in the electrical resistance. The tows in the K49 fabric used in this study contain over 200 fibers that are closely packed, which allows for the composite to maintain a percolated network of charge pathways even when the crack density along the AZO coating is significant. This is analogous to the increased tolerance to defects for tows and fabrics described previously, where bridged connections between fibers can compensate for bottlenecks to current flow within single fibers.

As described above, the electrical response as a function of strain in the composites

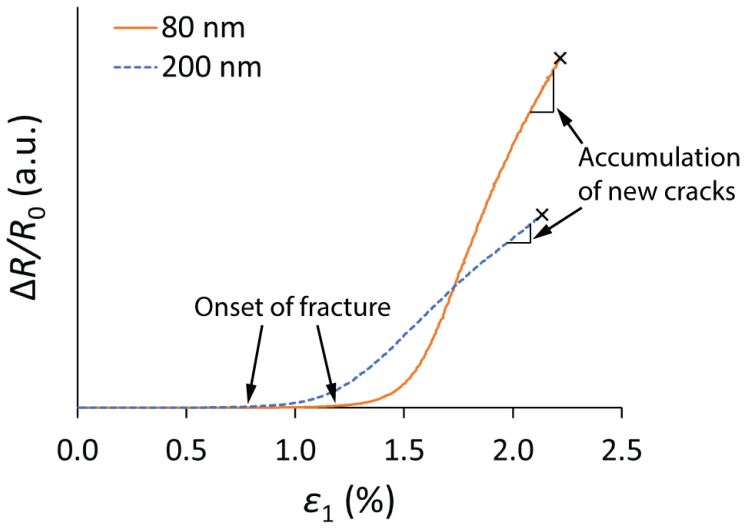

Figure 5.8: *Representative $\Delta R/R_0$ vs. strain curves for PMCs with thin (80 nm) and thick (200 nm) AZO coatings. The onset fracture of the coating occurs sooner for the thicker coating. As strain continues to increase, both the accumulation of cracks and the rate increase of the electrical resistance will be larger for the thin coating.*

varied with the thickness of the coating (Figure 5.5b). Initially, there is minimal change in resistance with strain. As the strain increases to approximately 0.7%-1.2%, a gradual increase in $\Delta R/R_0$ is observed, with an earlier onset for samples with thicker coatings. As the strain continues to rise, we observe a further increase in the slope of $\Delta R/R_0$. The slope of the curve in this higher-strain range (greater than 1.5%) becomes larger as the film thickness decreases. At the point where bulk fracture of the composite occurs, the final value of $\Delta R/R_0$ monotonically decreases with increasing coating thickness. These observations, which are summarized in Figure 5.8, suggest that multiple competing factors are at play when determining the thickness dependence of $\Delta R/R_0$.

To rationalize the competing effects in the cracking behavior for different coating thicknesses, we consider the theory of fracture mechanics of thin films on infinitely large substrates. A channeling crack will propagate in the coating at a critical onset stress. The coated fabric is modeled as a homogenous linear-elastic system, because the Young's modulus of K49 fibers (112 GPa) is sufficiently close to the Young's modulus of ZnO (143

GPa).[169] The embedded epoxy has a lower modulus of 1.26 GPa, and thus for simplicity it was not considered in this analysis. The critical stress in the coating (σ_c) can then be described as follows:[166,167]

$$\sigma_c = \sqrt{\frac{{K_{I_c}}^2}{1.98t}} \tag{5.4}$$

where K_{I_c} is the mode-I fracture toughness under plane-strain conditions and t is the thickness of the coating. Because K_{I_c} is proportional to $1/t^{0.5}$, thicker coatings will have a lower critical stress. This correlates well with our experimental observations, wherein the initial increase in $\Delta R/R_0$ occurs at lower strain values as the coating thickness increases (Figure 5.5b, Figure 5.8). We note that this initial increase will be statistical in nature, since the local stress along the individual fibers (as well as the initial defect distribution within the coatings) will vary slightly throughout the woven composite. However, the cumulative effect of multiple fibers experiencing the onset of fracture at low strain values will result in the net increase in measured resistance.

As the strain in the samples continuously increases, a sharper rise of the slope of $\Delta R/R_0$ vs. strain is observed as the coating thickness decreases (Figure 5.5b, Figure 5.8). The formation of additional cracks in the film depends on the stress and the inter-crack spacing. Both of these factors depend on the coating thickness. Previous modeling work has described the theoretical equilibrium crack spacing (s_{equil}) for a linear-elastic, homogeneous system with a perfectly bonded interface.[168] This can be expressed as:

$$\frac{s_{equil}}{t} = 5.6\sqrt{\frac{K_{I_c}}{{\sigma_f}^2 t}} \tag{5.5}$$

where σ_f is the stress in the coating. Contrary to Equation 5.4, s_{equil} is proportional to $t^{0.5}$. Therefore, s_{equil} will be larger for thicker films. This is consistent with the observation that the measured resistance of the composites rises faster with applied strain in the composite samples with thinner films. As shown in Figure 5.7, as inter-crack spacing decreases, the

pathway for electronic transport becomes more limited. An additional contributing factor to this trend is the fact that composites with thicker coatings have a higher number of bridged connections, forming a more robust percolation network. This also helps to explain the fact that the final measured $\Delta R/R_0$ after bulk fracture of the composite is lower for thicker coatings.

The relationships described herein between strain and electrical conduction can be used in the future to guide and inform the design of PMCs with interfacial coatings using ALD. In particular, we identify the acceptable strain limits under an applied load that are allowable to maintain sufficient conductivity (and continuity), which can be adjusted by varying the coating thickness. Depending on the targeted application, this may also lead to design tradeoffs, where control of thickness may also be important to the functionality itself. For example, as we show in Figures 5.2 and 5.4, effective resistivity decreases with increasing thickness. In applications where a large electrical current is passed, a lower resistance may be needed to avoid a large voltage drop and excessive Joule heating, which may necessitate a thicker coating. As shown in Figure 5.5b, while thicker coatings maintain a higher fraction of their initial conductivity at failure, they start to deviate in resistivity at lower strains. Therefore, depending on the predicted load profile that the composite will experience during service, this sets up a multi-dimensional optimization problem.

In addition to the coating serving as a component in a multifunctional composite, the change in resistance with strain could also be used for structural health monitoring. Because cracking leads to permanent changes in $\Delta R/R_0$, the resistance can serve as a record of maximum load experienced during operation. The sensitivity of this increase can be tuned by varying the coating thickness. This could be particularly useful as a signal to warn of the potential for catastrophic failure, since the range of $\Delta R/R_0$ spans several orders of magnitude before bulk fracture of the composite occurs. Because the coating has minimal impact on the elastic response of the coating (Figure 5.5a), this change in resistance can provide a warning signal as we approach catastrophic failure (Figure 5.5b).

5.3 Conclusion

This work demonstrated the ability to impart electrical conductivity into electrically-insulating fibers, fabrics, and PMCs through interfacial modification. The use of ALD facilitates sub-nm precision in coating thickness on complex fabrics, which can be used to tune the effective resistivity. Specifically, we show that the influence of thickness on resistivity depends both on the conduction through individual fibers, as well as the percolation through a fiber network, which is dependent on the number of bridged connections. This percolation effect allows for increased tolerance to defects in individual fibers, by providing alternative current pathways.

The conductive properties of the coated fabrics were maintained after they were embedded in an epoxy matrix using the VARTM method, illustrating the utility of this approach for the design and manufacturing of multifunctional composites. The composites were loaded in tension to failure, and the resulting changes in the electrical resistance were observed. These changes were attributed to crack formation in the conductive coating. The relative change in resistance was studied as a function of thickness, and two competing effects were observed. Specifically, the onset of cracking at low strain values occurs earlier as the coating thickness increases. However, the rate of increase in crack formation at larger strains was faster as thickness decreases. Additionally, the samples with the thicker coatings have a larger number of bridged connections, which helps to maintain electrical conductance even as cracks form.

Overall, the insights from this study can be useful when designing multifunctional composites. Specifically, the influence of coating thickness on the coupled electrical and mechanical response of the system can define the limits of useful operation, which may also be useful for structural health monitoring. In this study, AZO was selected as a model system owing to its high electrical conductivity. However, given the diverse set of materials that can be deposited by ALD, this platform can be extended in the future to manufacture more complex devices within a composite framework, including electronics, energy stor-

age, and optoelectronics. Beyond tuning the functional properties of the coating materials, this work also illustrates the importance of thin-film mechanics in designing such devices, which must be simultaneously optimized to ensure optimal performance under the targeted loading conditions.

Chapter 6

Biotemplated *Morpho* Butterfly Wings for Tunable Structurally Colored Photocatalysts

In photonic applications, there has been widespread interest in studying the structural coloration observed in *Morpho* butterfly wings. Structural coloration relies on photonic resonances rather than pigmentation, resulting in constructive interference of visible light bands. Small scales on the *Morpho*'s wings contain ribbed lamellae layers that form tree-like hierarchical structures that are ordered in a periodic manner.[170] The nanostructures selectively interact with specific wavelengths, which produces the characteristic blue iridescence of the *Morpho* butterfly.

The hierarchical nanostructures found in butterfly wings also make them interesting materials to study for functional applications. For example, butterfly wings have been used in optical gas sensors,[30] solar cells,[171] infrared detectors,[172] photocatalysts,[173] surface-enhanced Raman spectroscopy (SERS) substrates,[174] and more. In photocatalysis and photoelectrochemistry applications, hierarchical nanostructures have demonstrated enhanced performance due to a favorable combination of enhanced light absorption, reduced transport lengths, and high surface areas for favorable charge transfer kinetics.[36,175] This has

motivated efforts to harness the natural nanostructures in butterfly wings as a template to impart and optimize photocatalytic performance.[26,176]

Herein, we demonstrate a biotemplating approach to rationally design *Morpho* butterfly nanostructures with optimized photocatalytic activity in the UV regime while simultaneously tuning visible light reflection to impart aesthetic appeal. These multifunctional materials are inspired by recent work on photovoltaics (PVs), where structural color was used to tune aesthetic properties for applications such as decorative colored solar cells for building-integrated PVs.[177–179] Here, we apply this concept to the field of photocatalysis, which would enable integration of water purification systems into decorative buildings, signs, and structures. However, the ability to integrate photocatalytically active semiconductors into the complex hierarchical structure of *Morpho* wings is limited using traditional approaches.

To address this challenge, ALD is a powerful coating technique based on self-limiting surface reactions,[43,46] which enables deposition of conformal thin-films onto 3-D surfaces while precisely maintaining the structural form of the underlying template. ALD provides an unparalleled degree of precision and tunable control of film thickness and composition. Furthermore, ALD processes often occur at temperatures below 300 °C, which allows for coating of temperature-sensitive biological and organic templates.[180] ALD has been explored for a range of biotemplating examples, including tobacco mosaic virus templating of nanotubes,[181] DNA functionalization for carbon nanotube (CNT) transistors,[182] and improving the toughness of spider silk.[148]

Despite these benefits, there have been relatively few examples that use ALD for biotemplating in solar energy harvesting applications.[148,183–185] The pioneering study of ALD biotemplating of *Morpho* butterflies utilized electrically insulating Al_2O_3 as a proof-of-concept coating to tune the optical reflectivity.[186] To date, this approach has been limited to "passive" coatings, rather than integration of functional materials for targeted applications.[187–189] Another butterfly species, Papilio blumei, was coated with ALD TiO_2

and demonstrated tunable structural coloration, which was supported by simulations of the modulated optical properties, but no functional device was proposed or demonstrated.[190]

Here, we demonstrate the ability of ALD biotemplating to manufacture structurally colored water purification photocatalysts from *Morpho sulkowskyi* butterfly wings (Figure 6.1). The precise tunablility of ALD enables rational design of both structural color in the visible regime and photocatalytic activity in the ultraviolet. Using a combined experimental and computational approach, the relationships between film thickness and photocatalytic activity are elucidated. We observed an optimal thickness, which is attributed to the trade-offs between light absorption and catalytic quantum yield.

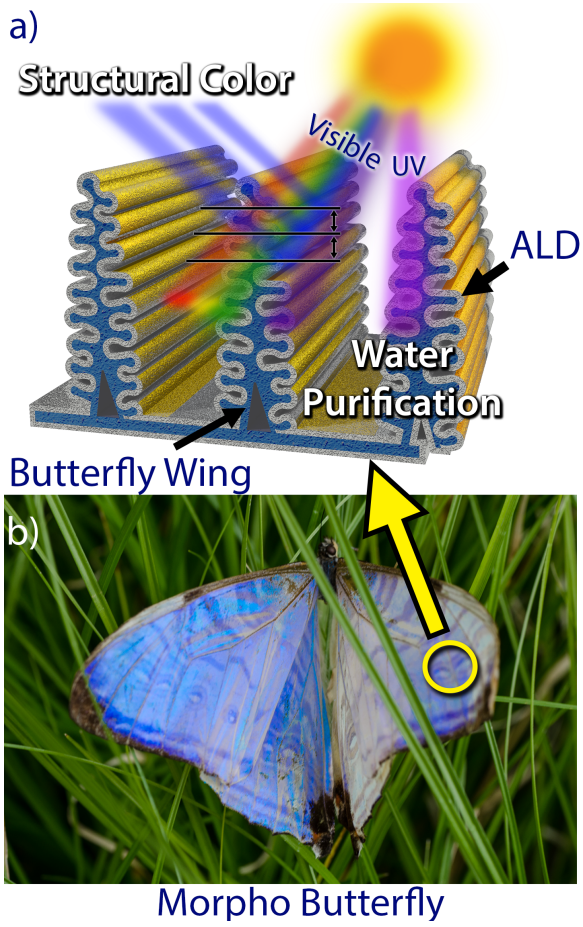

Figure 6.1: *(a) ALD coatings on Morpho butterfly wings enable multifunctional photocatalysts for water purification that also allow for tunable structural color for aesthetic appeal and (b) a Morpho sulkowskyi butterfly.*

6.1 Results and Discussion

As a model material system, *Morpho sulkowskyi* wings were coated with ZnO by ALD. ALD ZnO films are nanocrystalline wurtzite as deposited at low temperatures (<150 °C),[191] avoiding high-temperature postannealing processes that would damage the mechanical integrity of the butterfly wing. In contrast, alternate common photocatalysts such as TiO_2 grow as amorphous films by ALD, requiring high-temperature postannealing for crystallization.[192,193] While this preserves the microscopic form of *Morpho* scales, postannealing was observed to damage the macroscopic wing structure, causing effects such as geometric curling of the wing and pulverization. In contrast, the low-temperature ALD of crystalline ZnO enabled coating of entire wings, which remain intact and planar after deposition. Therefore, unlike alternate studies on biotemplated butterfly wing photocatalysts, which generated particle catalyst samples composed of wing fragments,[194,195] macroscopic planar wing sections with areas >1 cm^2 were studied in this work. This preserves the structural coloration over large areas, enabling their consideration for applications such as multifunctional decorative surfaces on macroscopic structures.

ZnO films of 10, 15, 20, 25, 35, and 50 nm were deposited onto *Morpho* wings and glass substrates. Figure 6.2 shows the highly conformal thin films by ALD that perfectly preserve the *Morpho* nanostructures, demonstrating the exceptional ability of ALD as a biotemplating method. No effects of nucleation delay of the ALD process were observed on the butterfly surface (Appendix B), which is attributed to the presence of surface hydroxyl groups on the underlying chitin. The nanocrystalline grains from the as-deposited ZnO process at 150 °C are clearly observable in Figures 6.2c and d. Furthermore, XPS confirmed the presence of ZnO on the butterfly surface, and XRD confirmed the polycrystallinity of the as-deposited ZnO film (Appendix B). As shown in the SEM images, for the 50 nm coatings, the branching lamellae ridges experienced a geometric "pinch-off" effect due to closure of the outer gaps (Figure 6.2d). Therefore, coatings less than 50 nm were studied to preserve the structure and maintain a high surface area that is accessible when immersed

in a liquid. The conformal nature of ALD is critical to monotonically increase thickness with subnanometer precision, which allows us to study thickness-dependent phenomena with unparalleled resolution.

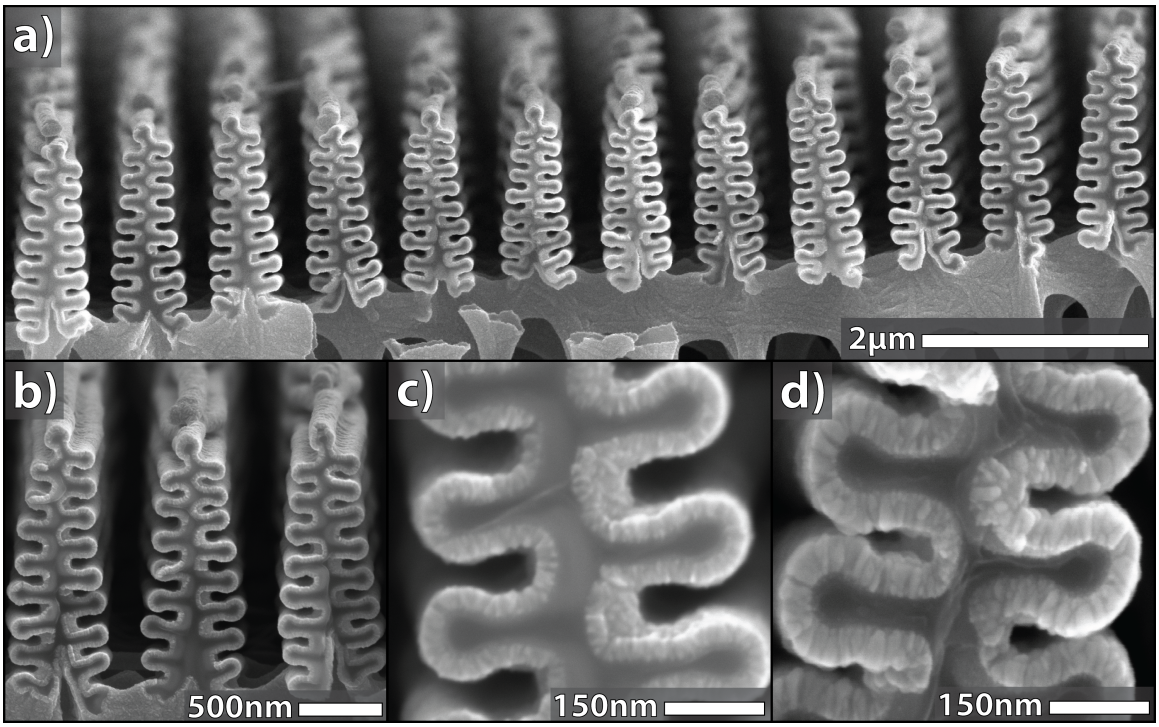

Figure 6.2: *Cross-sectional SEM images of 35 nm ALD ZnO films on Morpho nanostructures at (a) 10,000×, (b) 50,000×, and (c) 250,000× magnification. (d) SEM image of 50 nm ZnO at 250,000× magnification.*

The coating of the *Morpho* wings with ZnO generates a different index of refraction from the underlying biological chitin and also modulates the periodicity of the hierarchical nanostructures.[190] Therefore, by tuning the thickness of the ZnO coating, the structural coloration can be precisely manipulated. As demonstrated in Figure 6.3, the "digital" thickness control of ALD enables tunable structural coloration within the visible spectrum. An increase in thickness of the ZnO film resulted in a red-shift, which was quantified using optical reflection measurements in a UV–vis spectrophotometer under normal incidence. The peak wavelength shifted from 463 nm (uncoated *Morpho*) to 556 nm (35 nm ZnO coated *Morpho*). This was further supported by FDTD modeling, which was performed

to simulate the optical reflectance of the *Morpho* wings with the ZnO thicknesses used in this study (detailed methods in Appendix B). Considering the natural geometric variations in the biological wing surface versus the simplicity of the modeled geometry (a perfectly periodic array of a single geometric unit cell), the observed red-shift and specular trends in reflectivity agree remarkably well with the measured reflectance spectra.

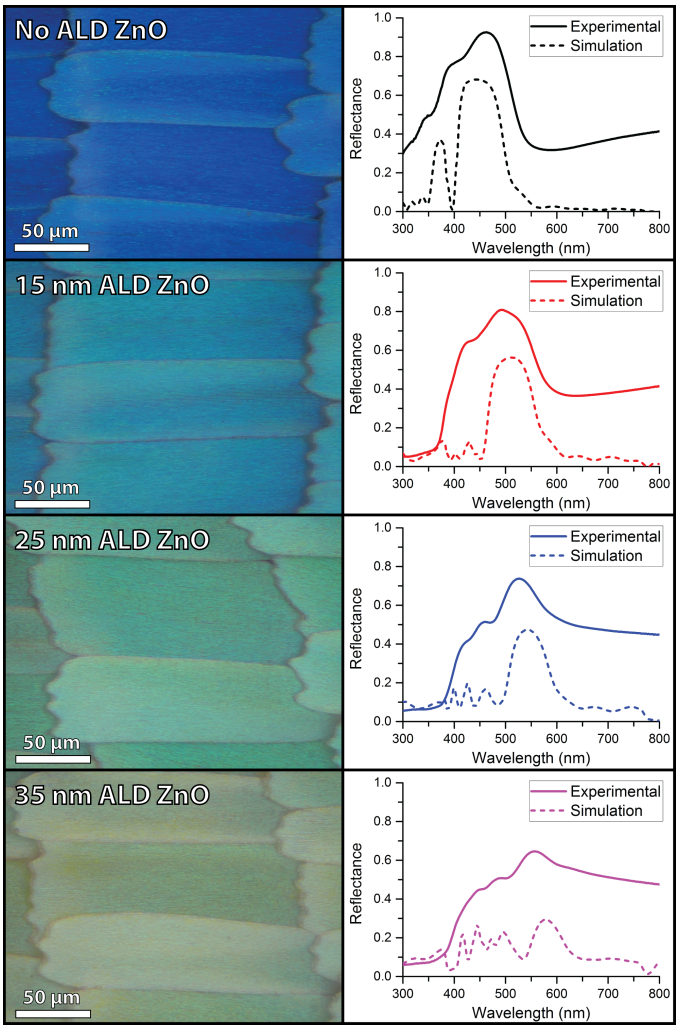

Figure 6.3: *(left) Optical microscopy images showing true coloration of the Morpho wing with varying ALD thickness. (right) Optical reflectance measurements and FDTD simulations showing the spectral reflection of the butterfly samples with varying ALD film thicknesses. Reflectance data correspond to the same ALD thicknesses shown on the left panel for each row.*

As shown in Figure 6.3, a decrease in reflectivity in the UV regime was also observed, which is a result of UV light absorption in the ZnO coating. This demonstrates the ability of ALD biotemplating as a method to selectively absorb specific wavelengths of light (which benefits from light scattering and trapping within the nanostructures), while simultaneously tuning the reflection of visible wavelengths due to programmable control of the geometric and optical parameters that result in structural coloration. This ability to decouple optical absorption and reflection across different wavelengths could enable the creation of multifunctional devices that benefit from aesthetic control of color.

To demonstrate that functionalized biological nanostructures can serve as efficient photocatalysts for water purification, methylene blue dye-degradation tests were performed on fully intact ALD coated *Morpho* wings under UV illumination.[196] The precise thickness control of ALD allowed for a study of thickness-dependent photocatalytic activity, which was compared to ALD films on planar substrates. In contrast, previously reported biotemplated butterfly photocatalysts utilized wing fragments that were dispersed as particles in solution.[194,195,197]

In particle photocatalyst measurements, the incident light intensity on the particle surfaces changes as the light travels through the dye/particle solution due to attenuation. As a result, the localized photoactivity varies depending on the position of the dispersed photocatalyst particles in the dye solution, making a quantitative comparison of intensity-dependent reaction rate kinetics difficult. Therefore, particle-based measurements typically only report the power of the light source and distance from the solution. To the best of our knowledge, none have reported quantifiable reaction kinetics on intact biotemplated wings.

In contrast, the water purification test setup for the current study enabled a well-defined light intensity incident on the planar and intact wing sample, which allows us to quantify the reaction rate kinetics of the photocatalyst samples at a uniform intensity. By placing the fully intact ALD coated *Morpho* wings at a fixed distance from the light source, we directly measured the incident light intensity in the plane of the wing sample before measurements,

which was maintained in all experiments at 15 W/m^2.

Figure 6.4a shows the remaining dye concentration measured at two-hour intervals. As expected, ZnO-coated *Morpho* butterfly samples exhibited an increase in photocatalytic activity compared to that of uncoated butterfly templates. Figure 6.4b demonstrates the thickness dependence of the ALD coating on photocatalytic activity. Interestingly, when increasing ZnO thickness on the butterfly samples, a maximum in activity was observed followed by a decrease. The 15 nm coated *Morpho* butterfly exhibited the fastest overall dye-degradation behavior, whereas the thicker samples showed diminishing photocatalytic activity. The 15 nm ZnO on *Morpho* reduced the dye concentration by 66.4% from its original concentration after being exposed to UV light for 12 h.

Planar ALD ZnO films were also studied to quantify the origins of the photocatalytic enhancement, and demonstrate that it can be attributed to the photonic properties and geometry of the *Morpho* wings. ZnO coated glass samples were prepared, and their photocatalytic activity was compared with that of the butterfly samples with equivalent ALD ZnO thicknesses (Figure 6.4b). Unlike the butterfly templates, no maximum in activity was observed over the thickness range tested, and activity increased monotonically with thickness. This demonstrated that the optimal activity of the 15 nm butterfly sample was uniquely attributed to the butterfly morphology, which motivated a deeper investigation of the underlying phenomena that guide activity on the butterfly template.

To quantify the benefits of the biotemplated geometry, the optimal 15 nm coated *Morpho* butterfly sample can be first compared to a 15 nm planar sample. The planar sample reduced the dye concentration by only 6.5% of its original measured concentration after 12 h of UV light exposure, demonstrating the benefits of the nanostructured *Morpho* template to enhance activity. An additional planar sample was prepared with an equivalent mass of ZnO over the same projected area as the 15 nm *Morpho* butterfly sample to account for the increase in mass loading from the butterfly surface. The roughness factor (actual surface area divided by projected surface area) of the *Morpho* butterfly was measured to be approx-

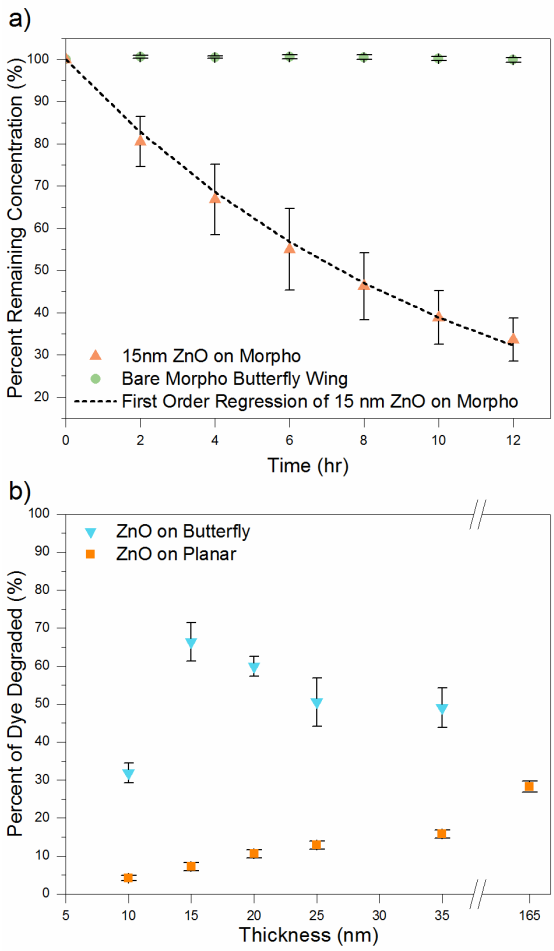

Figure 6.4: *(a) Remaining dye concentration vs time for an uncoated wing and a 15 nm coated sample. A first order kinetics model is fit to the 15 nm ZnO on Morpho data, which was derived from Figure B.4 of the Appendix. (b) Percent of dye degraded vs ALD ZnO thickness after 12 h of UV illumination.*

imately 11 using cross-sectional SEM analysis. Therefore, a planar sample with a thickness of 165 nm was deposited on a glass slide. The percentage of dye concentration degraded after 12 h UV run was 28.3% from the original measured concentration. In summary, the 15 nm ALD ZnO on the *Morpho* butterfly enhanced the dye-degradation process compared to both 15 nm ZnO (equivalent thickness) 165 nm ZnO (equivalent mass loading) on a planar substrate. This illustrates the benefits of the nanostructured butterfly template to enhance light absorption while minimizing carrier diffusion lengths and maximizing surface area for enhanced charge extraction.

Using the concentration measurements at various points in time in our dye-degradation setup, the reaction rate kinetics of the catalyst could be calculated under a uniform light intensity. Due to the planar geometry of the butterfly wing photocatalysts, the photocatalytic activity (measured as percentage of dye degraded from the initial concentration) was normalized by projected geometric area, rather than normalization by mass, which is typically used for powder catalyst loading (Appendix B). This allows us to make direct quantifiable comparisons of the reaction rate kinetics, deconvoluting effects of dye concentration and sample surface area. The reaction rate (r) fit well with a first order kinetics model:

$$r = -\frac{\mathrm{d}[C]}{\mathrm{d}t} = k[C]^n \tag{6.1}$$

where n = 1, and after mathematical integration and normalizing by area (A) we obtain,

$$kt = \frac{\ln\left(\frac{C(0)}{C(t)}\right)}{A} \tag{6.2}$$

where C_0 is the initial concentration and $C(t)$ is the time-dependent concentration under illumination. The reaction rate coefficient (k) was calculated from a fitted regression following the Equation 6.2 (see Figure B.4 for an example). These coefficients are tabulated in Table 6.1. The 15 nm ZnO coating on the *Morpho* substrate had the highest reaction rate constant of 0.086 $h^{-1}cm^{-2}$. The fitted regression was then applied to Figure 6.4a, and the curve closely follows the remaining concentration percentages with an R^2 value of 0.995. This 15 nm ZnO *Morpho* sample exhibited superior photocatalytic dye-degradation activity with a reaction rate coefficient of 3.6 times that of the 165 nm ZnO planar sample (0.023 $h^{-1}cm^{-2}$).

To understand the origins of the optimal photocatalytic performance observed at a coating thickness of 15 nm on the *Morpho* wings, additional FDTD simulations were performed. The FDTD model simulated the electric field intensity for the varying ZnO film thicknesses on the *Morpho*'s hierarchical nanostructures under 360 nm plane wave illumi-

Table 6.1: *Reaction rate kinetics for Morpho wings with varying ZnO thickness and planar glass with a ZnO thickness of 165 nm (equivalent mass per area to 15 nm on the butterfly)*

***Morpho* Butterfly**		
THICKNESS (nm)	k **($h^{-1}cm^{-2}$)**	R^2
10	0.033	0.8838
15	0.086	0.9953
20	0.067	0.9990
25	0.052	0.9998
35	0.048	0.9996
Planar Glass		
THICKNESS (nm)	k **($h^{-1}cm^{-2}$)**	R^2
165	0.023	0.994

nation at normal incidence. The results are shown in Figure 6.5, and capture the trade-off between increased catalyst mass loading and decreased optical penetration depth with increasing ALD coating thickness on the wings. As the ZnO layer thickness increases, attenuation of the incident UV light increases near the top surface of the wing, preventing light from being transmitted through the branching lamellae ridges to the lower portion of the wing scales, thereby limiting optical penetration depth.

To understand the relationship between light absorption and reaction rate kinetics, the rate equation for a photochemical reaction can be expressed as a function of the catalytic quantum yield (Φ) of the photocatalyst and absorbed light intensity (I_a).[198,199]

$$-\frac{d[C]}{dt} = \Phi I_a \tag{6.3}$$

Assuming a first order reaction, this can be combined with Equation 6.1 to provide an expression for the rate constant of the photoreaction.[198]

$$k' = \frac{(\Phi I_a)}{[C]} \tag{6.4}$$

The rate constant is proportional to the product of the quantum yield and the absorbed light intensity. In the case of suspended powder photocatalysts, the rate is known to initially increase with increasing catalyst mass loading due to an increase in absorbed light intensity

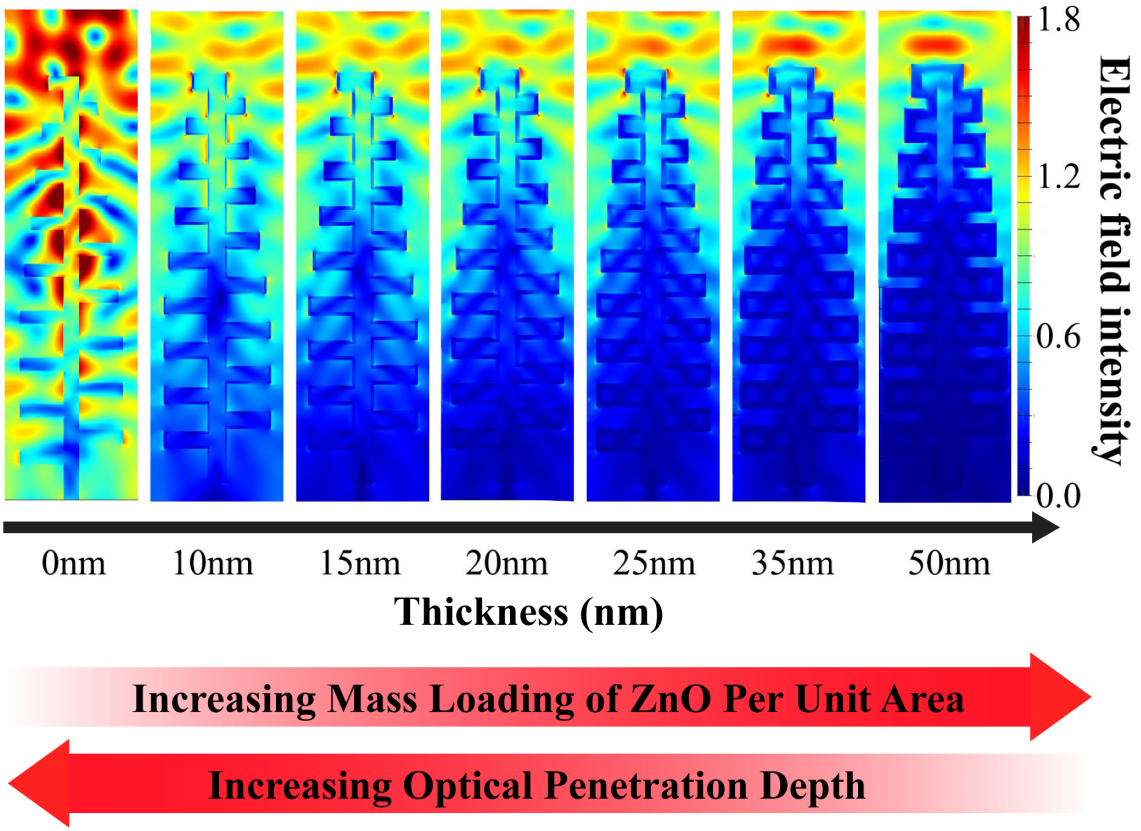

Figure 6.5: *FDTD simulations of electric field intensity for varying ALD ZnO thicknesses on Morpho butterfly wings.*

(I_a). As photocatalyst loading continues to increase, the reaction rate saturates, leading to an optimal mass loading.[198] Additionally, in some cases the reaction rate begins to decrease with further mass loading, which can be attributed to reduced optical penetration depth and increased light scattering. This represents a decrease in catalytic quantum yield, which is caused by an increased photon flux being concentrated in a smaller region of the solution. In other words, the catalytic quantum yield is a function of localized light intensity. This can be explained by increased recombination in the semiconductor material, as the turnover frequency (TOF) of the catalyst surface cannot keep up with the increased flux of excited charge carriers to the semiconductor/solution interface.[175] Indeed, the intensity dependence of catalytic quantum yield for ZnO has been previously observed in photocatalytic CO oxidation.[200]

This mechanism is also responsible for the maximum in reaction rate kinetics observed as a function of ALD coating thickness on the butterfly samples. As the coating thickness increases initially, there is an increase in total absorbed light intensity (I_a) of the film. However, as shown in the FDTD simulations, as film thickness continues to increase, the optical penetration depth decreases, leading to an increased local absorbed photon flux at the top surface of the wing. This leads to a decrease in catalytic quantum yield, as the TOF requirements of the top surface become the limiting factor in the overall photocatalysis kinetics. Because very little light penetrates to the bottom of the lamellae structure, these portions of the wing surface are under-utilized, leading to minimal contribution to the overall chemical reaction. This concept is shown schematically in Figure 6.6, where the trade-offs between increasing I_a and decreasing Φ lead to a maximum in reaction rate. As can be observed in Figure 6.5, the maximum activity observed at 15 nm therefore reflects this balance of absorption and localized quantum yield.

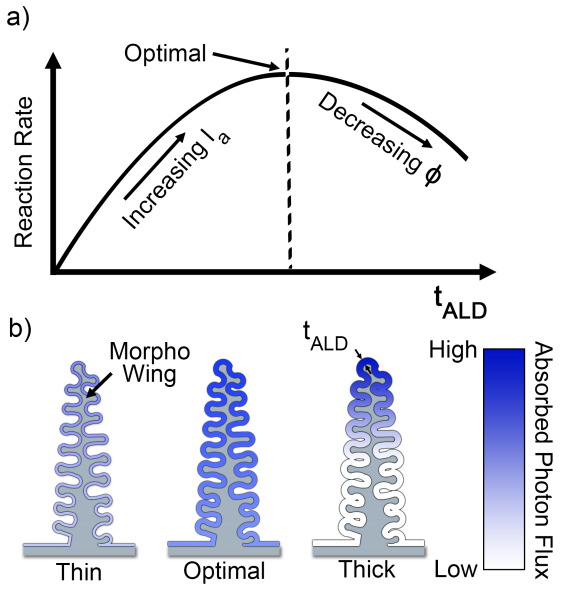

Figure 6.6: *(a) Depiction of the trade-offs between light absorption and localized quantum yield on reaction rate and (b) variation in localized absorbed photon flux with increasing ALD thickness.*

6.2 Conclusion

This study demonstrates that biotemplating of *Morpho* butterflies can be used to enable a new class of multifunctional materials with precisely tunable structural color across visible wavelengths while simultaneously enhancing photocatalytic activity. The precise thickness control enabled by ALD allowed us to optimize performance and study the trade-offs that arise due to competing effects of film thickness, catalytic quantum yield, and optical reflection/absorption. Additionally, by maintaining the macroscopic butterfly wing structure intact over large areas, these materials can provide the building blocks to integrate structural color into aesthetically designed surfaces, which can be further stitched together to form pixels, and integrate functions such as water purification into the sides of buildings, signs, or other facades. This degree of tunability and control demonstrates that atomically precise biotemplating is a powerful nanomanufacturing platform to extend bioinspired engineering to new applications.

Chapter 7

Conclusions and Future Work

7.1 Conclusions

The work in this dissertation has shown that ALD can be utilized as a powerful tool for modifying surfaces and interfaces to impart multifunctional properties into composite and hybrid material systems. The conclusions and scientific contributions derived from the work presented in this dissertation are discussed below.

In the work presented in Chapter 3, we studied the growth rate effects of TiO_2 and its dependence on temperature control. Thermocouples and IR imaging were used to assess the temperature uniformity. Nonuniform ALD growth was observed to occur, which was attributed to variations in the temperature distribution across the reactor. A redesign of the reactor with careful placement of heater and temperature sensors was implemented, which was informed by computer-aided design (CAD) and finite element analysis (FEA) studies. After installation of the new reactor, the updated thermal design significantly improved the thickness uniformity. This work provides a direct contribution in understanding the relationship between processing conditions and ALD growth behavior. In particular, the work presented highlights the importance of accurate sensing and reporting of thermal gradients in ALD systems, which become more critical to uniformly coat large substrates, especially when using precursor chemistries that have tighter ALD windows.

Chapters 4 and 5 explored the use of ALD coatings to modify the properties of polymer-

matrix composites (PMCs). Evaluating and controlling the interfacial properties in composites is critical to predict and achieve the desired macroscopical properties. Therefore, understanding the mechanism of delamination when using ALD coating interlayers is important. The main contribution from Chapter 4 was the study and evaluation of the interfacial mechanical properties of PMCs with varying materials of ALD coating interlayers (i.e. Al_2O_3, ZnO, and TiO_2). The interfacial strength was generally weaker when coating the fibers with any of the coatings. The polymer microdroplets were observed to adhere better to the ALD coatings than to the fiber. Therefore, if stiffer composites are desired, functionalization of the fiber surfaces such as electrochemical oxidation or plasma treatments may be necessary to promote stronger adhesion between the ALD coatings and the fibers. Furthermore, here we demonstrated ALD coatings can impart new functionalities onto materials, which were further explored in Chapters 5 and 6.

Chapter 5 expanded upon the work from Chapter 4. The results from this work demonstrated the tunable control of properties, which was enabled by the thickness control of coatings by ALD. Furthermore, a change in electrical resistance was determined to occur as a result of cracking of the conductive coatings, which was evaluated as a function of strain and coating thickness. A model from thin-film fracture mechanics was leveraged to interpret the cracking behavior of the coatings and the associated changes in electrical resistance. This represents the first study to date that has developed or studied electrically conductive composites that utilize only ALD coatings for interphase modification. Incorporating electrical conduction in PMCs utilizing conformal coatings presents a step towards the development of composites integrated with more complex functionality. Lastly, this is the first study to our knowledge that has performed *in situ* tests looking at coupled effects between mechanical loading and electrical conductivity for PMCs modified with ALD in the context of fracture mechanics. The evaluation of these coupled phenomena in multifunctional is important in order consider their use and application as multifunctional structures.

In Chapter 6, a biotemplating approach is presented that replicates *Morpho* nanostructures by depositing nanocrystalline ZnO coatings onto wings via ALD. This study demonstrated the ability to precisely tune the natural structural coloration, while also integrating multifunctionality by imparting photocatalytic activity onto fully-intact Morpho wings. Optical spectroscopy and finite-difference time-domain (FDTD) numerical modeling demonstrate that ALD ZnO coatings can rationally tune the structural coloration across the visible spectrum. These structurally colored inorganic-organic hybrid materials can also be optimized to maximize UV light absorption and charge extraction for water purification. Unlike powder photocatlaysts, the fully-intact wing photocatalyst allows for quantification of reaction kinetics at a uniform light intensity, enabling quantitative evaluation of the benefits of the hierarchical nanostructured geometry for photocatalytic activity. The novelty of this study lies not only in the unparalleled ability of ALD to replicate the complex hierarchical nanostructures found in natural wings, but to impart new functionality onto the natural template through integration of functional materials with tailored properties. This is the first demonstration of ALD biotemplating of structurally colored materials to impart active functionality. It represents a pioneering effort incorporating both tunable structural coloration in biological nanostructures and bio-inpsired photocatalysis. These multifunctional photocatalysts present a potentially new approach to integrating solar energy harvesting into visually attractive and decorative surfaces that can be integrated into building facades or other macroscopic structures to impart aesthetic appeal. Lastly, this study also inspired other published work in our lab, which highlighted the impact of geometric parameters (such as ALD coating thickness) on the spatial heterogeneity of light absorption and internal quantum efficiency, which directly affect system performance of nanostructured photocatalysts.[201]

In summary, the work presented throughout this dissertation contributed to various fields, primarily in the processing science of nanomaterials, specifically ALD, for multifunctional materials and nanostructured surfaces. It also contributed in understanding

coupled relationships and mechanisms between coating thickness, functional activation, and performance of multifunctional materials.

7.2 Future Work

As discussed in Section 2.2, Chapter 4, and Chapter 5, synthetically-derived structural fibers and polymers are an important component in fiber-reinforced composite (FRC) design and manufacturing of low-density materials. However, these materials are often made from petroleum-based polymers with limited recyclability or reusability. In contrast, biologically-derived composites have the potential to serve as an environment-friendly and biodegradable alternative to traditional composite materials. For example, replacement of glass fibers with plant-based cellulose fibers could enable low-weight composites with comparable mechanical performance, while significantly reducing the carbon footprint.[202] However, natural fibers have inherent electrically insulating properties, which would normally make them incompatible for many multifunctional applications. The work we have presented throughout this thesis has demonstrated that multifunctionality can be enabled on biological templates through reliable surface and interface modification methods (Chapter 6. Thus, low-temperature atomic layer deposition (ALD) presents an opportunity to extend multifunctional capabilities with tunable control of properties onto biologically-derived composites.

In Chapter 5 we demonstrated the limitations associated with film fracture when utilizing brittle coatings to impart multifunctionality. In some cases, this brittle behavior may not be desired. For example, there might be an application that requires the conductive properties to remain unchanged under large strains. Integration of molecular-layer deposition (MLD) processes present an opportunity to develop functional coatings that are ductile. MLD is analogous to ALD, which is able to deposit organic films with sub-nanometer precision.[203,204] Organic-inorganic hybrid films have demonstrated conductive properties

while maintaining more ductile properties.[205] The integration of MLD into multifunctional composites has the potential to add additional "knobs" to tune for materials optimization. Therefore, the ability to precisely tune the chemistry and structure of the coatings using hybrid ALD-MLD processes offers a powerful platform to engineer and design multifunctional materials with a broader range of material properties.

Lastly, the interest to integrate functional devices into composites is continuing to expand. As the device complexity increases, this results in more stringent processing limitations. An example of this is the field of structural batteries, which require the deposition of a variety of materials (e.g. electrodes, solid electrolyte, current collector, etc) within a composite backbone. A structural battery requires precise deposition processes in order to obtain the desired layered structure of materials. This highlights the need of coating techniques that are able to deposit thin-films with precise control of thickness and composition, which could potentially be enabled by the ALD process knowledge set forth in this dissertation.

APPENDIX A

Supplementary Information for Chapter 5

A.1 Additional Experimental Details for Chapter 5

Sample preparation

Kevlar® (K49) fabrics that came in a 351-style plain weave were used for this study. Strips of fabric were cut to a length and width of 70 mm and 11 mm, respectively. The cuts were made along the tows to ensure a 0° and 90° oriented bidirectional fabric. Additionally, single tows and single fibers were extracted from separate K49 stock and cut to a length of 130 mm. The fibers, tows, and fabrics were cleaned in boiling acetone for 10 min, followed by boiling ethanol for 10 min, and finally in deionized water for 5 min. The samples were then placed in a vacuum oven and heated to 135 °C for 3 hours to remove adsorbed moisture. Afterwards, the K49 samples were transferred to the atomic layer deposition (ALD) reactor. Clean Si wafer pieces and glass slides were included in each run to measure the aluminum-doped zinc oxide (AZO) film thickness and resistivity, respectively.

Four-point probe

The AZO-coated single fibers, single tows, and woven fabric were placed on an electrically insulating substrate (i.e. 2.5 cm. × 7.6 cm. glass slides). Afterwards, PELCO® conductive silver paint was applied to the samples to make four contact pads. The contact pads were approximately 3 mm wide and the edge-to-edge spacing between them was 12 ± 1 mm (the

center-to-center distance between the pads was 15 mm). Afterwards, spring-loaded copper pins, which are connected to the potentiostat, were pressed against the silver paint (Figure A.3). Afterwards, a single cycle voltammogram was done by measuring the electrical current while sweeping the voltage at a rate of 10 mV/s between -0.5 V and 0.5 V. This single cycle produced a linear current-voltage curve (Figure A.4), which was fitted to calculate the inverse of the electrical resistance (1/R).

Process for putting silver contacts on composite samples

Adding the conductive silver contacts on the composite samples is a slightly different process. The epoxy can encapsulate the conductive AZO coatings after the vacuum-assisted resin transfer molding (VARTM) process (which is described in Appendix A.1). Thus, it is necessary to first apply a protective mask that can be removed after the VARTM process in order to access the AZO. A polymethyl methacrylate (PMMA) mask was applied on two opposite edges of the 140 mm × 140 mm fabrics. The PMMA layer that was applied along the edges was approximately 13 mm wide and was applied several times on both faces of the fabric. The fabric with the PMMA masking layer was then used to make the composite via the VARTM process. Lastly, the composite samples were cut to the desired size and the PMMA mask was removed to access the AZO coating. This was done by submerging the edge of the composite with the PMMA in acetone for 5-10 minutes. The PMMA softens and can be gently removed with tweezers. After the PMMA was removed, the samples were prepared following ASTM standard D3039/D3039M. Composite strips with in-plane dimensions of 11 mm × 140 mm were prepared for tensile testing, and tabs were added per ASTM standard D3039/D3039M. Tabs were added to the sample per ASTM D3039/D3039M. Finally, PELCO® conductive silver paint was applied to the exposed area and allowed to dry. Another layer of silver paint was applied, and copper foil of 0.5 cm width and 7.5 cm length was pressed onto the silver paint. The paint was allowed to dry, then a third layer of silver paint was applied on top of the copper foil. The same process

was done on the other side of the composite strip. The copper foil was added in order to attach the alligator clips of the potentiostat for electrical conductivity measurements.

Vacuum-assisted resin transfer molding

The K49 fabrics coated with 0 nm, 40 nm, 80 nm, 120 nm, 160 nm, and 200 nm of AZO were used in the VARTM process to make single-ply PMCs. The size of the K49 fabrics used for the VARTM process were 140 mm × 140 mm, and the cuts were done along the tows to ensure a 0° and 90° oriented bidirectional fabric. The coated K49 fabric was placed on an aluminum surface covered with a Teflon sheet, with peel ply and breather fabric arranged on the left and right sides of the fabric to aid the flow of epoxy over the fabric. Plastic piping was placed at the left and right sides of the Teflon sheet, with breather fabric wrapped around the ends to similarly aid the flow of epoxy. On one side, plastic piping was inserted into a catch pot, which was subsequently connected to a pump, which applied vacuum to the setup. On the other side, the plastic piping was sealed, but would later be used to feed the resin into the VARTM. The K49 fabric, peel ply, breather fabric, and piping arrangement was then covered with a vacuum bag, which was adhered to the surrounding aluminum surface using Airtech AT200Y tacky tape (Composite Envisions, LLC). The vacuum pump was powered on and the vacuum bag was checked for air leaks. Afterwards, the sealed pipe was submerged in a container with the low-viscosity resin and opened. This causes the resin to flow into the vacuum bag setup. The resin cured after 36 hours, to create a thin, even layer of epoxy around the K49 fabric, resulting in a K49-reinforced composite. A picture of the setup can be found in Figure A.5.

Calculating the effective cross-sectional area (A_{eff})

Single fiber:

The nominal radius (r_i) of a single K49 fiber is 6.3 μm as measured by SEM and image post processing software. The fiber can have some variation in shape, but the geometry

was mostly circular. Thus, the effective cross-sectional area of the fiber A_{fib} was calculated as that of a circle with outer radius (r_o):

$$r_o = r_i + t_{AZO} \tag{A.1}$$

where t_{AZO} is the thickness of the AZO coating. Lastly, A_{fib} is calculated as:

$$A_{fib} = \pi(r_i + t_{AZO})^2 = \pi {r_o}^2 \tag{A.2}$$

Single tow:

A single tow of K49 has 267 fibers for the style 351 plain weave fabric used (as specified by the supplier, JPS Composite Materials CO.). Then the effective cross-sectional area of the tow A_{tow} simply becomes:

$$A_{tow} = n_f \pi {r_o}^2 = n_f A_{fib} \tag{A.3}$$

where n_f is the fiber count for a single tow. There are 267 fibers in each tow per the supplier (JPS Composite Materials, Corp).

Fabric:

The effective resistivity of the fabric is calculated using the nominal cross-sectional area, rather than the actual cross-sectional area. The effective cross-sectional area of the woven fabric A_{fab} then becomes:

$$A_{fab} = w_{fab} t_{fab} \tag{A.4}$$

where w_{fab} is the measured width of the fabric and t_{fab} is the nominal thickness of the fabric per the supplier (JPS Composite Materials, Corp).

Calculating the AZO cross-sectional area (A_{AZO})

The A_{AZO} for single fibers (textit$A_{AZO_{fib}}$), tows (textit$A_{AZO_{tow}}$), and woven fabrics (textit$A_{AZO_{fab}}$) are:

$$A_{AZO_{fib}} = \pi({r_o}^2 - {r_i}^2) \tag{A.5}$$

$$A_{AZO_{fib}} = n_f \pi({r_o}^2 - {r_i}^2) = n_f A_{AZO_{fib}} \tag{A.6}$$

$$A_{AZO_{fab}} = n_t n_f \pi({r_o}^2 - {r_i}^2) = n_t n_f A_{AZO_{fib}} = n_t A_{AZO_{tow}} \tag{A.7}$$

where n_t is the number of longitudinally-aligned tows (0° direction). As explained in the main article, the transversely-aligned tows (90° direction) were assumed to not contribute to the conductance of the fabric.

Calculating the percent difference of ρ_e to ρ_t

We define "percent difference" as the difference between the average experimental resistivity (ρ_e) and the theoretical limit (ρ_t) relative to the ρ_t. The equation for the percent difference is:

$$\text{Percent difference} = \left(\frac{\rho_e - \rho_t}{\rho_t} \right) \cdot 100\% \tag{A.8}$$

A.2 Supplementary Figures and Tables for Chapter 5

Table A.1: *Percent difference of the average experimental effective resistivity to the theoretical limit of the electrical resistivity.*

THICKNESS (nm)	FIBER	TOW	FABRIC	COMPOSITE
40	2792%	-	-	-
80	169%	888%	576%	325%
120	200%	226%	189%	275%
160	177%	24%	75%	159%
200	99%	16%	54%	239%

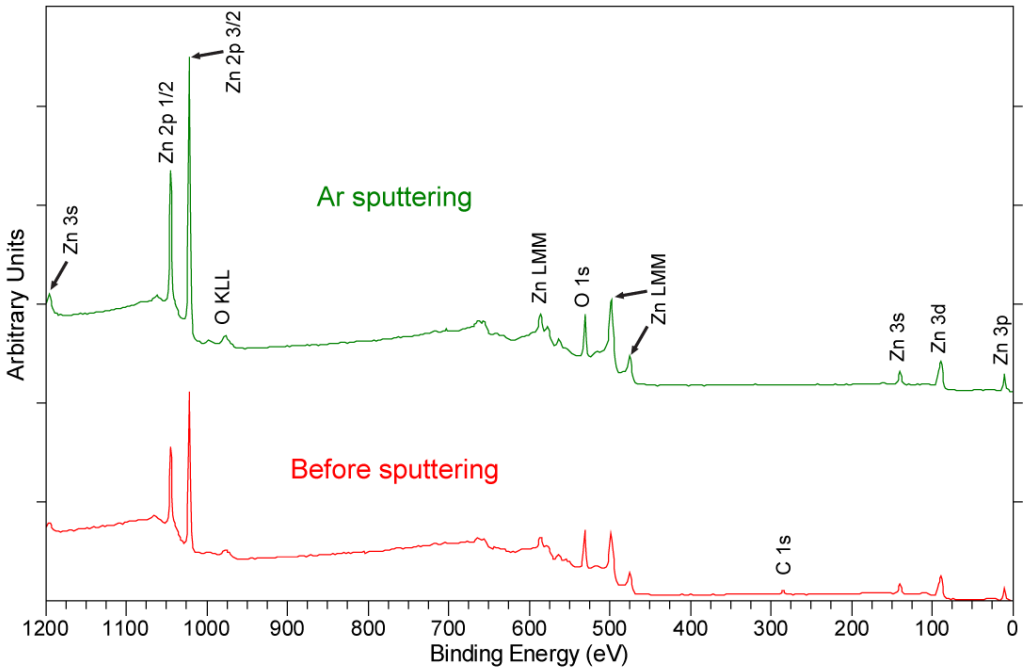

Figure A.1: *X-ray photoelectron spectroscopy of K49 fabrics coated with 120 nm of AZO. Ar sputtering removes the adventitious carbon on the coating surface.*

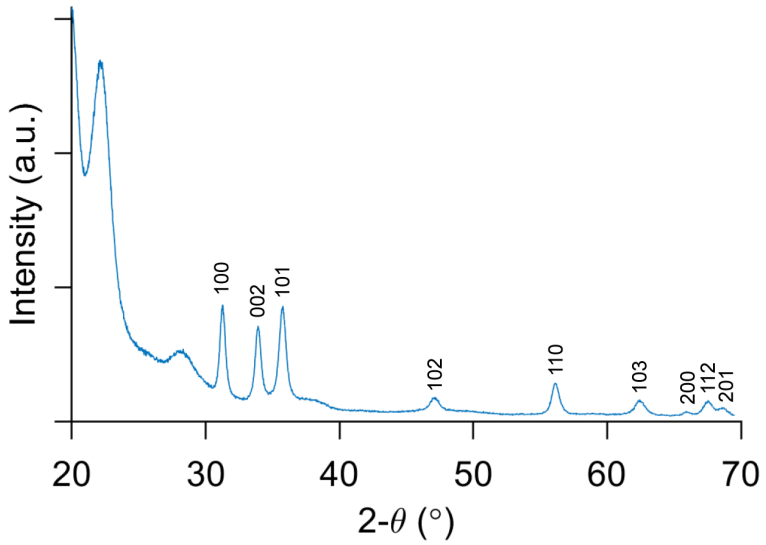

Figure A.2: *X-ray diffraction of K49 fabrics coated with 120 nm of AZO. The indexed diffraction peaks show (100), (002), and (101) planes, which are characteristic of the hexagonal (wurtzite) ZnO crystalline structure.*

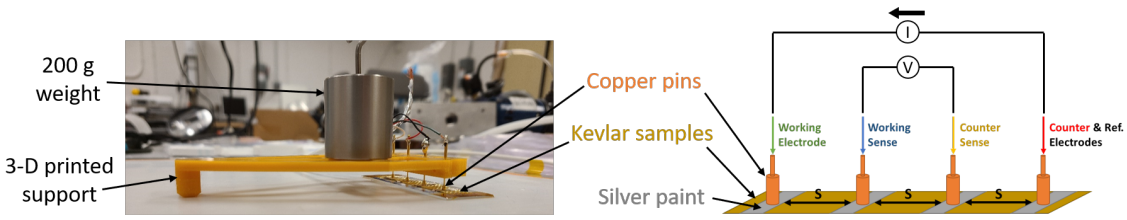

Figure A.3: *Left, four-point probe setup using a 3-D printed support with four spring-loaded copper pins. A 200 g weight is applied to ensure the pins contact the silver paint pads. Right, schematic of the four-point probe.*

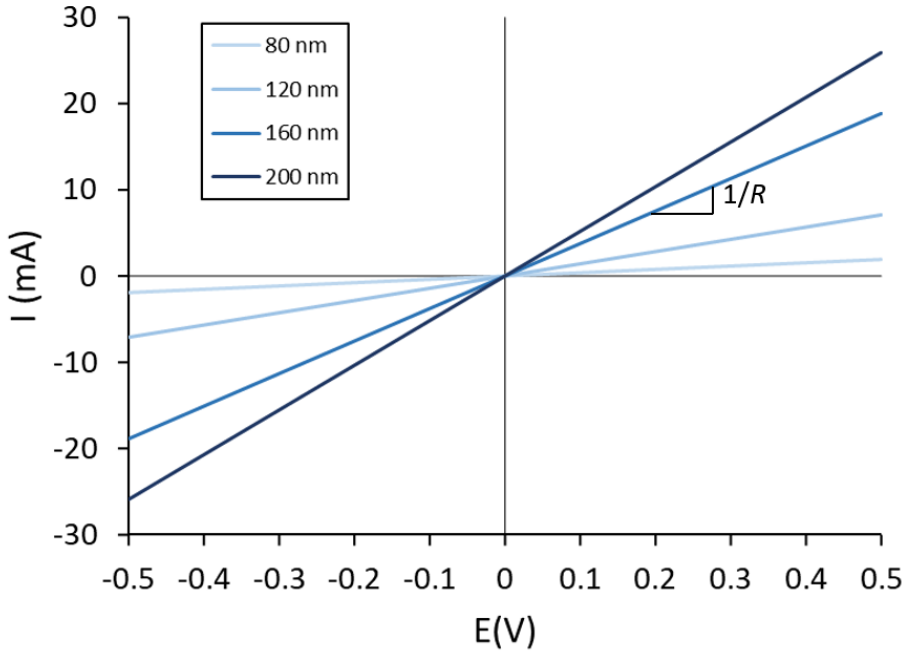

Figure A.4: *Example of current-voltage curves obtained from the four-point probe method done on AZO-coated woven K49 fabrics.*

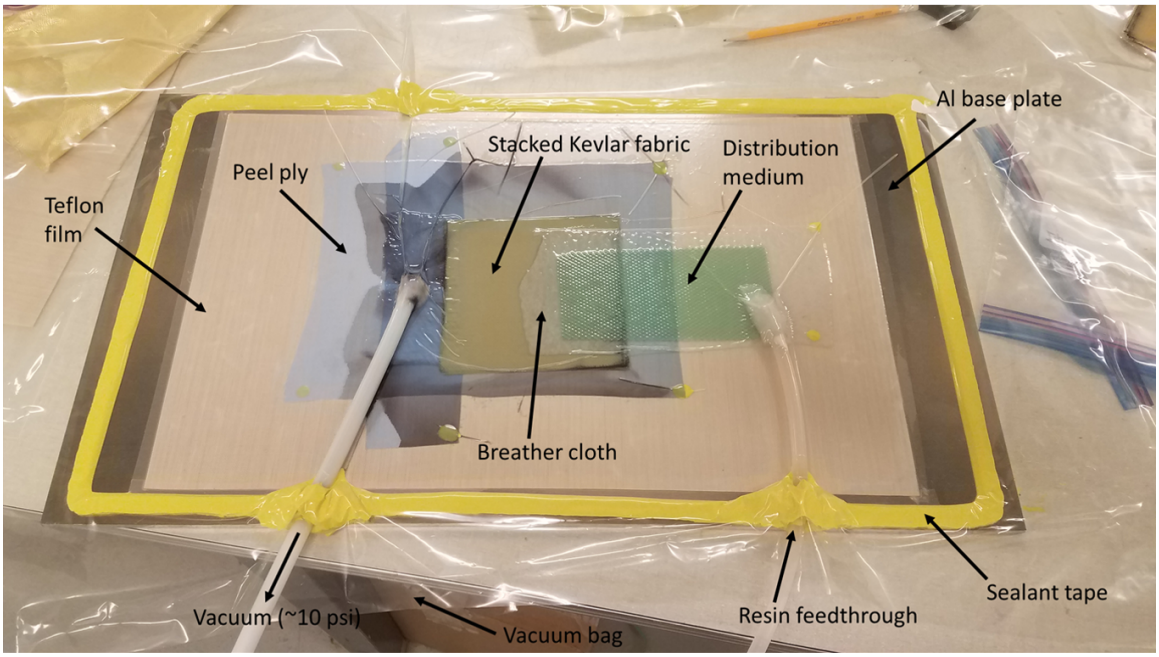

Figure A.5: *Components of the lab-scale vacuum-assisted resin transfer molding (VARTM) setup.*

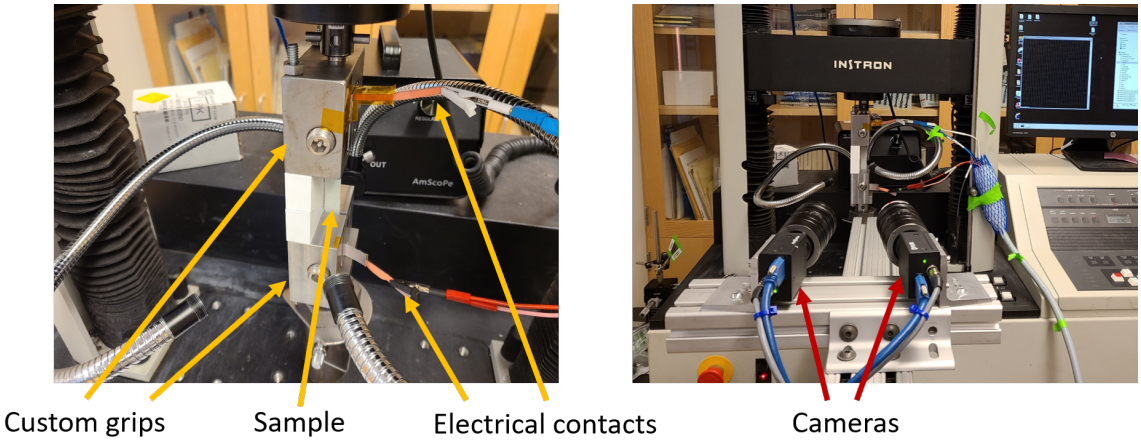

Figure A.6: *Shows the experimental setup for the tensile tests. Left, the clamp grip fixture with the sample is mounted on the tensile tester. Right, two-camera setup to capture images for digital image correlation (DIC).*

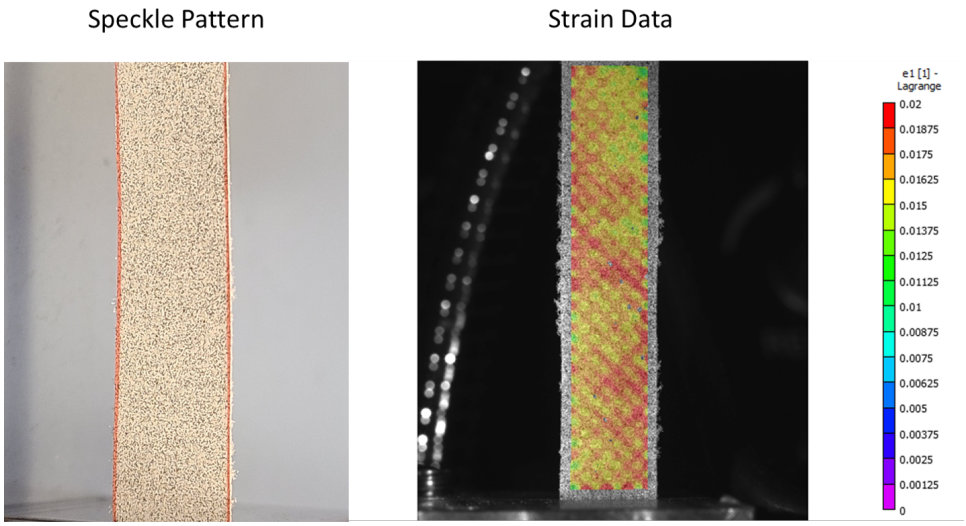

Figure A.7: *Left, speckle pattern applied to K49-reinforced composite sample. Right, map of the principle strain of the sample obtained via digital image correlation (DIC). The average principle strain ($R(\varepsilon_{11})$) was recorded.*

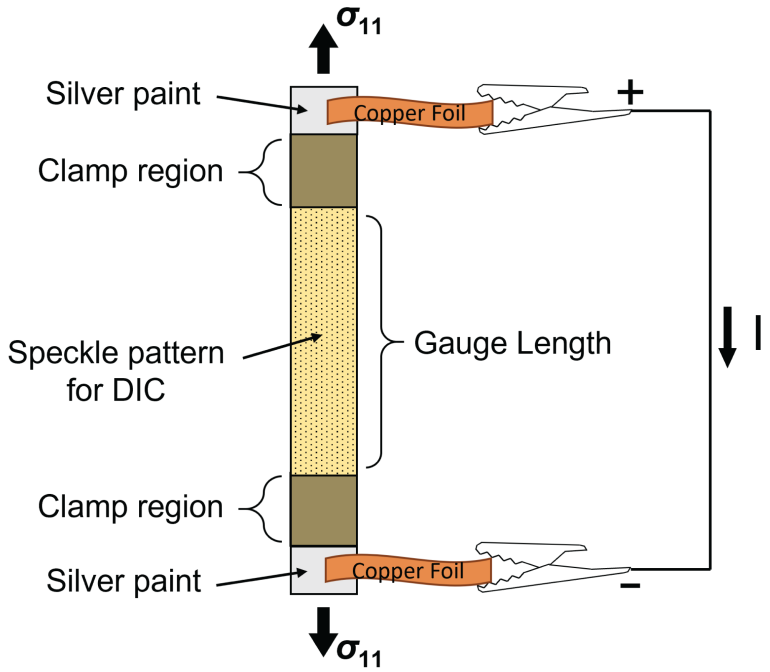

Figure A.8: *Schematic of composite sample prepared for in situ mechanical testing while monitoring the electrical resistance of the sample.*

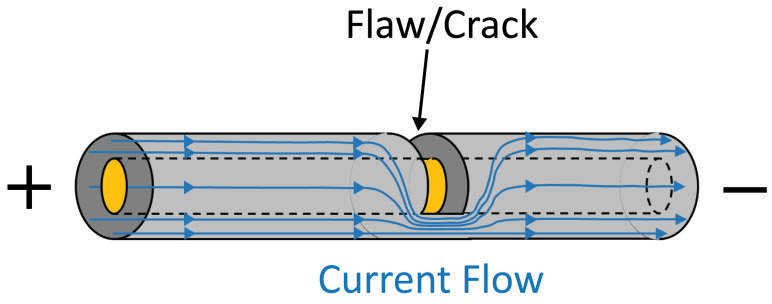

Figure A.9: *Schematic of single fiber with local flaw/crack that constricts local current flow.*

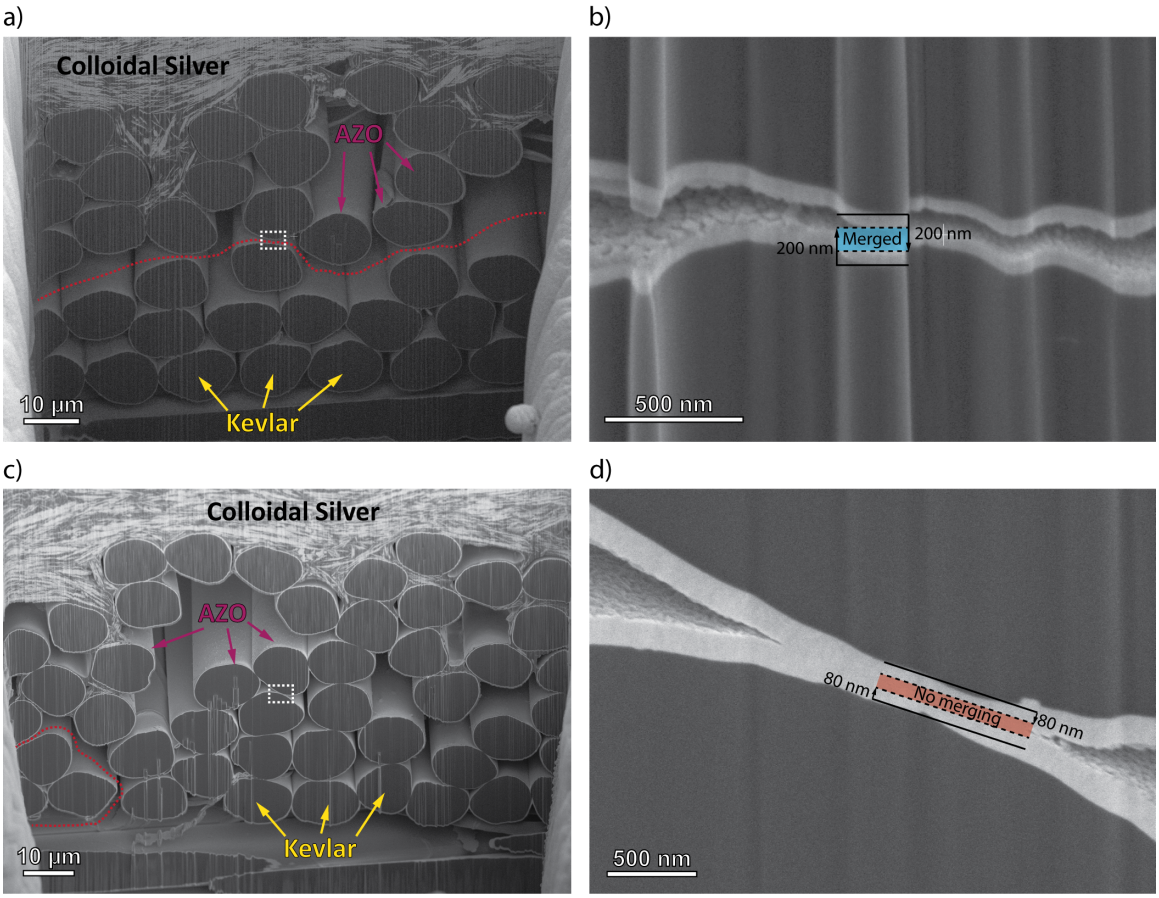

Figure A.10: *a) Low-magnification SEM cross-section of an 80 nm AZO-coated K49 fabric with colloidal silver paint. The section below the red dashed line has no viable charge pathways to the silver paint. The white box is the b) high-magnification SEM cross-section. If the coating were 200 nm, the AZO between the fibers would have merged. c) Low-magnification SEM cross-section of a 200 nm AZO-coated K49 fabric with colloidal silver paint. The section inside the red dashed line has no viable charge pathways to the silver paint. The white box is the d) high-magnification SEM cross-section. If the coating was 80 nm, the AZO between the fibers would not have merged.*

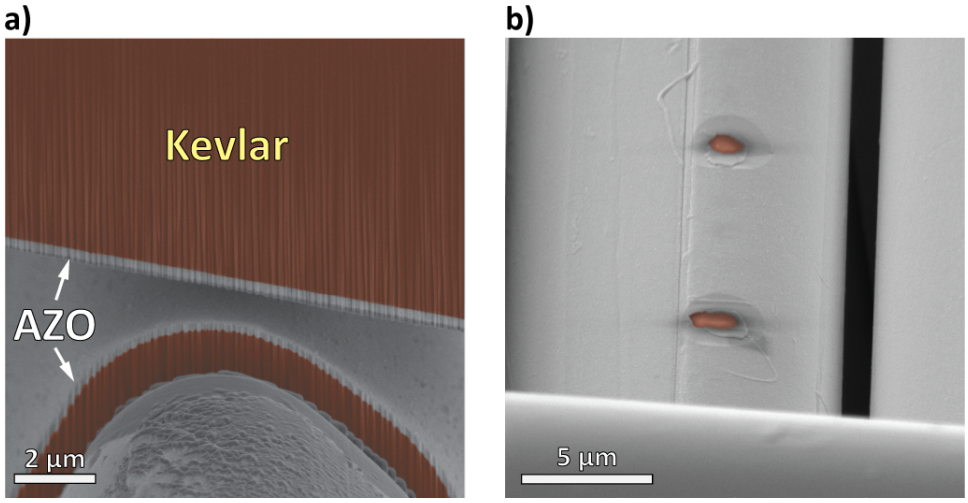

Figure A.11: *SEM-FIB imaging of a) a cross-section of two perpendicular fibers with a 200 nm ZnO coating, and b) SEM of a K49 fiber coated with 120 nm ZnO that had bridged connections with two perpendicular fibers that detached, exposing the surface of the K49.*

APPENDIX B

Supplementary Information for Chapter 6

B.1 Experimental Details for Chapter 6

A custom built, flow-type thermal ALD system was used for ALD processing. The ALD reaction chamber was set to 150 °C, with an argon carrier gas flow rate of 10 sccm, and the base pressure of the system was ∼600 mTorr. An ALD cycle for depositing ZnO films consists of a 0.05 s pulse of diethylzinc (DEZ) and a 30 s argon purge time, and then followed by a 0.1 s pulse of water and 30 s Argon purge. ZnO films of 10 nm, 15 nm, 20 nm, 25 nm, 35 nm, and 50 nm thickness were deposited onto the *Morpho* butterfly wings and glass substrates, based on a growth rate of 2.0 Å/cycle. Five samples of each set of thickness and each substrate were made for this study.

The glass substrates were prepared by dicing them to the desired dimensions and cleaned by rinsing them with acetone, isopropyl alcohol, and deionized water. The glass substrates were then coated with ZnO by ALD. The butterfly samples were pre-baked at 100 °C for 2 hours and then coated with ZnO.

After ALD, a working area of 1 cm^2 area was defined for each sample. The edges of the samples outside of the predefined 1 cm^2 area were covered with a polymethyl methacrylate (PMMA) blocking film to define the wetted area, therefore controlling the area of photocatalytic reaction. The same PMMA was used to help adhere the butterfly wing samples to a clean glass slide to make handling of the butterfly samples easier. The sides and

bottom of the samples were also coated with PMMA so that only the active 1 cm^2 area was exposed to water.

A 15 W fluorescent UV (365nm) lamp (UVP Blak-Ray XX-15BLB UV Bench Lamp) was used as the illumination source. The height and position of the sample with respect to the UV light is critical to ensure consistent UV light intensity for all dye degradation experiments. For this, we first assembled the test setup without the dye solution and measured the light intensity at the position where the sample would be placed. A power meter was used to measure the light intensity at the exact position relative to the light source where the samples would be placed. The light intensity was measured to be 15 W/m^2 . The samples were placed at the same position so that the light intensity on the intact butterfly surface was identical for all experiments. This planar geometry provides a much more consistent light illumination at the photocatlyst surface than using powder photocatalysts, allowing for quantitative measurement of reaction-rate kinetics at a uniform intensity.

Prior to illumination of the photocatalyst samples, a 20 μM methylene blue solution was prepared, and all wetted components were pre-rinsed with this methylene blue solution (i.e. inside walls of the beaker, stir bar, and sample). After rinsing, 10 ml of 20 μM methylene blue dye solution were added to the beaker. The beaker was then left stirring in the dark for 30 minutes until adsorption of dye on the sample came to equilibrium with the solution. Next, an aliquot of the dye solution was taken to measure the light absorbance utilizing a UV-vis spectrophotometer (Shimazdu UV-2600). Absorption intensity was recorded at the peak absorption wavelength for Methylene Blue of 664 nm to quantify dye-concentration. Aliquot samples of the dye-solution were measured for every 2-hour intervals until the 12th hour, and the entire methods described above were repeated for each sample.

The equation to calculate percentage of dye degraded ($D\%$) was:

$$D\% = \frac{(C_0 - C(t))}{C_0} \times 100 = \left(1 - \frac{C(t)}{C_0}\right) \times 100 \tag{B.1}$$

where C_0 is the initial concentration as measured by absorption and *C(t)* is the concentra-

tion after an amount of time illuminated by UV light (t) as measured by absorption. The percentage of the remaining dye concentration ($R\%$) was also calculated:

$$R\% = 100 - D\% = \left(\frac{C(t)}{C_0}\right) \times 100 \tag{B.2}$$

To measure the reflectance spectra of butterfly wings with varying ZnO film thicknesses, all the samples were cut into about 1 cm × 1 cm in size and attached to the silica glass with their iridescent sides facing up. The wavelength range was set from 300 nm to 800 nm during the measurement. Reflection spectra were recorded using a Lambda 750S UV/VIS/NIR spectrophotometer (Perkin Elmer, Inc., USA). Five sample replicas were tested for each to observe if the results were reproducible. The error bars on Figure 6.4a are the standard deviation from the averages of the five replica samples. The reaction rate coefficient was calculated by utilizing the average concentration after time *C(t)* at each time interval. For example, the concentration for all 5 samples of the 10 nm coated butterfly were averaged at each time interval (the 2^{nd}, 4^{th}, 6^{th}, 8^{th}, 10^{th}, and 12^{th} hour) of light illumination. Then this was plotted in a graph similar to Figure B.4 and a regression was fit to that averaged data points. The slope of the graph is our reaction rate coefficient (k). The y-intercept of the graph is 1.098 nanometers and the coefficient of determination (R^2) is 99.97%. All data points including the two thinnest coatings being studied (10nm and 15 nm) traced the fitted line with negligible error. From this, we deduce that nucleation delay effects are trivial within the range of the ALD coatings being studied. The reflection properties and electric field intensity distribution of the *Morpho* wings with different ZnO thicknesses were simulated by FDTD methods. ZnO films were assumed to be deposited on the butterfly wings uniformly, consistent with the SEM analysis. In the modeling, the refractive index of chitin was set to be 1.56 and the wavelength-dependent refractive index of ZnO was input.[206] A plane wave was used as the light source and the incident direction was perpendicular to the surface of butterfly wings. The boundary condition was set based on the assumptions that the light was absorbed (perfectly matched layer, PML) in the ver-

tical direction and the nanostructures were periodic (periodic boundary condition, PBC) in the horizontal direction. The mesh size was 2 nm × 2 nm. The structural parameters were set based on SEM image of *Morpho* butterfly wings, including the lamella thickness (∼60 nm), the lamella length (∼200 nm), the inter-lamella spacing (∼150 nm), the height of the ridge (∼1900 nm), the width of the ridge (∼70 nm), and the separation between ridges (∼770 nm), as shown in Figure B.5.

B.2 Supplementary Figures and Tables for Chapter 6

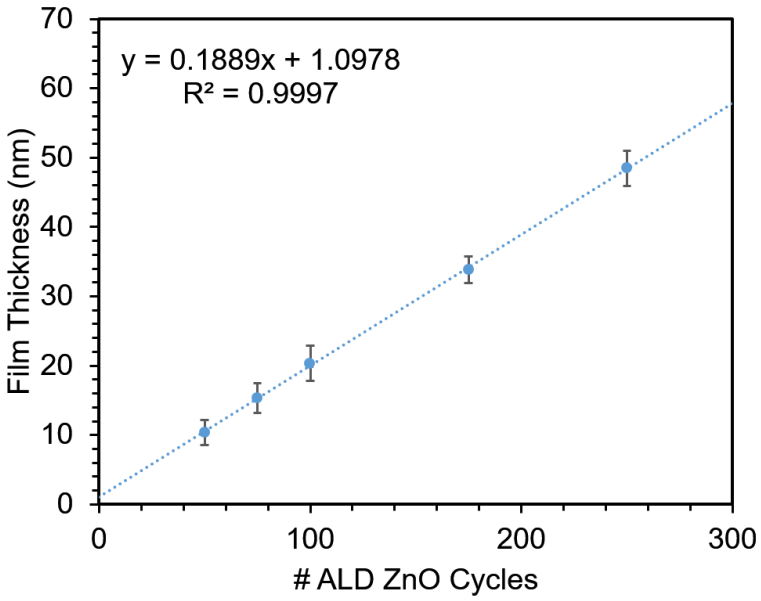

Figure B.1: *Film thickness of the ZnO coated Morpho butterflies (measured using image processing software) as a function of ALD cycles. A linear regression that fit the set of film thickness data is included.*

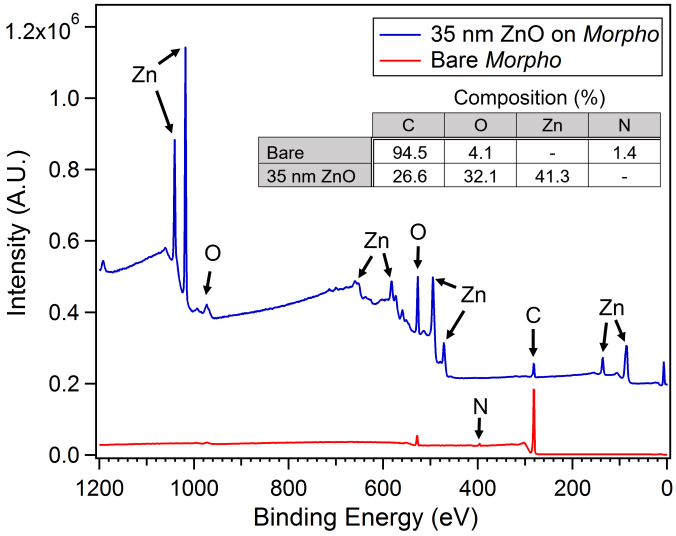

Figure B.2: *X-ray photoelectron spectroscopy of a bare Morpho wing sample and a Morpho wing coated with 35 nm of ZnO.*

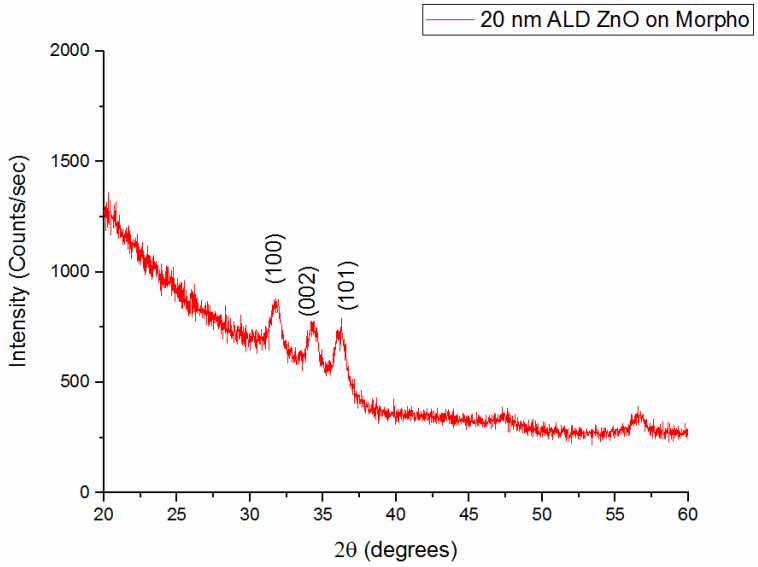

Figure B.3: *X-ray diffraction showing Wurtzite crystal structure of Morpho butterfly coated with 20 nm of as-deposited ALD ZnO.*

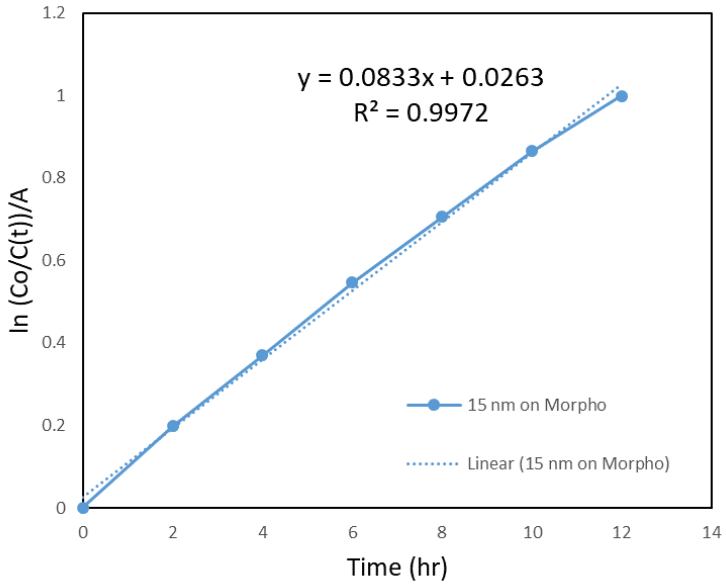

Figure B.4: *First order kinetics model of the initial concentration per averaged concentration after illumination, per unit area as a function of time. The slope of the regression is the reaction rate constant (k) for a 15 nm ZnO coated Morpho butterfly.*

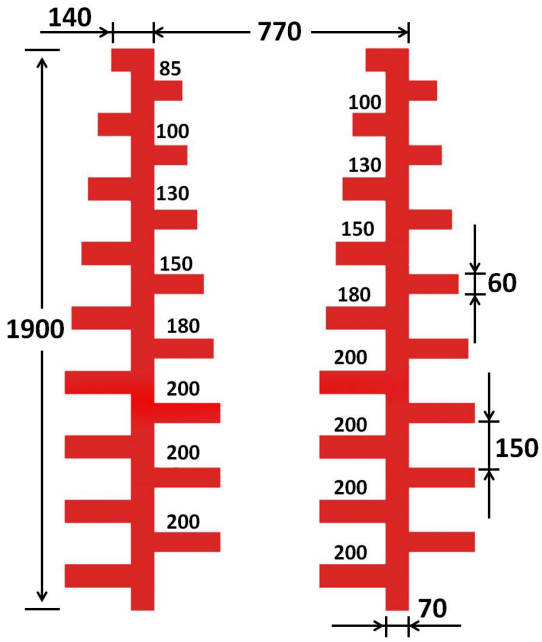

Figure B.5: *Geometric representation of the branched lamellae structures of the Morpho wing utilized for FDTD modeling. Used to simulate the optical properties (Figure 6.2) and the electric field intensity (Figure 6.4) for different thickness of ZnO coatings (unit: nm).*

BIBLIOGRAPHY

(1) Kazyak, E.; Wood, K. N.; Dasgupta, N. P. Improved Cycle Life and Stability of Lithium Metal Anodes through Ultrathin Atomic Layer Deposition Surface Treatments. *Chemistry of Materials* **2015**, *27*, 6457–6462.

(2) Chen, K. H.; Sanchez, A. J.; Kazyak, E.; Davis, A. L.; Dasgupta, N. P. Synergistic Effect of 3D Current Collectors and ALD Surface Modification for High Coulombic Efficiency Lithium Metal Anodes. *Advanced Energy Materials* **2019**, *9*, 1802534.

(3) Tang, L. G.; Karoos, J. L. A review of methods for improving the interfacial adhesion between carbon fiber and polymer matrix. *Polymer Composites* **1997**, *18*, 100–113.

(4) Lin, Y.; Ehlert, G.; Sodano, H. A. Increased interface strength in carbon fiber composites through a ZnO nanowire interphase. *Advanced Functional Materials* **2009**, *19*, 2654–2660.

(5) Chen, Y.; Ginga, N. J.; LePage, W. S.; Kazyak, E.; Gayle, A. J.; Wang, J.; Rodríguez, R. E.; Thouless, M. D.; Dasgupta, N. P. Enhanced Interfacial Toughness of Thermoplastic–Epoxy Interfaces Using ALD Surface Treatments. *ACS Applied Materials & Interfaces* **2019**, *11*, 43573–43580.

(6) Bielinski, A. R.; Boban, M.; He, Y.; Kazyak, E.; Lee, D. H.; Wang, C.; Tuteja, A.; Dasgupta, N. P. Rational Design of Hyperbranched Nanowire Systems for Tunable

Superomniphobic Surfaces Enabled by Atomic Layer Deposition. *ACS Nano* **2017**, *11*, 478–489.

(7) Sharafi, A.; Kazyak, E.; Davis, A. L.; Yu, S.; Thompson, T.; Siegel, D. J.; Dasgupta, N. P.; Sakamoto, J. Surface Chemistry Mechanism of Ultra-Low Interfacial Resistance in the Solid-State Electrolyte Li7La3Zr2O12. *Chemistry of Materials* **2017**, *29*, 7961–7968.

(8) Allemang, C. R.; Cho, T. H.; Trejo, O.; Ravan, S.; Rodríguez, R. E.; Dasgupta, N. P.; Peterson, R. L. High-Performance Zinc Tin Oxide TFTs with Active Layers Deposited by Atomic Layer Deposition. *Advanced Electronic Materials* **2020**, *6*, 2000195.

(9) Cho, T. H.; Farjam, N.; Allemang, C. R.; Pannier, C. P.; Kazyak, E.; Huber, C.; Rose, M.; Trejo, O.; Peterson, R. L.; Barton, K.; Dasgupta, N. P. Area-Selective Atomic Layer Deposition Patterned by Electrohydrodynamic Jet Printing for Additive Manufacturing of Functional Materials and Devices. *ACS Nano* **2020**, *14*, 17262–17272.

(10) Snyder, J. F.; Carter, R. H.; Wetzel, E. D. Electrochemical and mechanical behavior in mechanically robust solid polymer electrolytes for use in multifunctional structural batteries. *Chemistry of Materials* **2007**, *19*, 3793–3801.

(11) Liu, P.; Sherman, E.; Jacobsen, A. Design and fabrication of multifunctional structural batteries. *Journal of Power Sources* **2009**, *189*, 646–650.

(12) Toohey, K. S.; Sottos, N. R.; Lewis, J. A.; Moore, J. S.; White, S. R. Self-healing materials with microvascular networks. *Nature Materials* **2007**, *6*, 581–585.

(13) Yang, Y.; Urban, M. W. Self-healing polymeric materials. *Chemical Society Reviews* **2013**, *42*, 7446–7467.

(14) Chen, Y.; Kushner, A. M.; Williams, G. A.; Guan, Z. Multiphase design of autonomic self-healing thermoplastic elastomers. *NATURE CHEMISTRY* — **2012**, *4*, DOI: 10.1038/NCHEM.1314.

(15) Gao, W.; Emaminejad, S.; Nyein, H. Y. Y.; Challa, S.; Chen, K.; Peck, A.; Fahad, H. M.; Ota, H.; Shiraki, H.; Kiriya, D.; Lien, D. H.; Brooks, G. A.; Davis, R. W.; Javey, A. Fully integrated wearable sensor arrays for multiplexed in situ perspiration analysis. *Nature* **2016**, *529*, 509–514.

(16) Yamada, T.; Hayamizu, Y.; Yamamoto, Y.; Yomogida, Y.; Izadi-Najafabadi, A.; Futaba, D. N.; Hata, K. A stretchable carbon nanotube strain sensor for human-motion detection. **2011**, DOI: 10.1038/NNANO.2011.36.

(17) Amjadi, M.; Kyung, K. U.; Park, I.; Sitti, M. Stretchable, Skin-Mountable, and Wearable Strain Sensors and Their Potential Applications: A Review, 2016.

(18) Camacho-Ballesta, C.; Zornoza, E.; Garcés, P. Performance of cement-based sensors with CNT for strain sensing. *Advances in Cement Research* **2016**, *28*, 274–284.

(19) Aly, K.; Li, A.; Bradford, P. D. Strain sensing in composites using aligned carbon nanotube sheets embedded in the interlaminar region. *Composites Part A: Applied Science and Manufacturing* **2016**, *90*, 536–548.

(20) Yang, Y.; Gupta, M. C.; Dudley, K. L.; Lawrence, R. W. Novel carbon nanotube - Polystyrene foam composites for electromagnetic interference shielding. *Nano Letters* **2005**, *5*, 2131–2134.

(21) Chung, D. D. Carbon materials for structural self-sensing, electromagnetic shielding and thermal interfacing. *Carbon* **2012**, *50*, 3342–3353.

(22) Luo, X.; Chung, D. D. Electromagnetic interference shielding using continuous carbon-fiber carbon-matrix and polymer-matrix composites. *Composites Part B: Engineering* **1999**, *30*, 227–231.

(23) Akbar, M.; Curiel-Sosa, J. L. Piezoelectric energy harvester composite under dynamic bending with implementation to aircraft wingbox structure. *Composite Structures* **2016**, *153*, 193–203.

(24) Balazs, A. C.; Emrick, T.; Russell, T. P. Nanoparticle polymer composites: Where two small worlds meet, 2006.

(25) Maspoch, D.; Ruiz-Molina, D.; Veciana, J. Old materials with new tricks: Multifunctional open-framework materials. *Chemical Society Reviews* **2007**, *36*, 770–818.

(26) Lou, S.; Guo, X.; Fan, T.; Zhang, D. Butterflies: inspiration for solar cells and sunlight water-splitting catalysts. *Energy & Environmental Science* **2012**, *5*, 9195.

(27) Wegst, U. G. K.; Bai, H.; Saiz, E.; Tomsia, A. P.; Ritchie, R. O.; Ortiz, C.; Boyce, M.; Wegst, U. G. K.; Bai, H.; Saiz, E.; Tomsia, A. P.; Ritchie, R. O. Bioinspired structural materials. *Nature materials* **2014**, *14*, 23–36.

(28) Sun, T.; Feng, L.; Gao, X.; Jiang, L. Bioinspired surfaces with special wettability. *Accounts of Chemical Research* **2005**, *38*, 644–652.

(29) Paris, O.; Burgert, I.; Fratzl, P. Biomimetics and Biotemplating of Natural Materials. *MRS Bulletin* **2010**, *35*, 219–225.

(30) Potyrailo, R. A.; Ghiradella, H.; Vertiatchikh, A.; Dovidenko, K.; Cournoyer, J. R.; Olson, E. Morpho butterfly wing scales demonstrate highly selective vapour response. *Nature Photonics* **2007**, *1*, 123–128.

(31) Passoni, L.; Criante, L.; Fumagalli, F.; Scotognella, F.; Lanzani, G.; Di Fonzo, F. Self-Assembled hierarchical nanostructures for high-efficiency porous photonic crystals. *ACS Nano* **2014**, *8*, 12167–12174.

(32) Lee, J. H. Gas sensors using hierarchical and hollow oxide nanostructures: Overview, 2009.

(33) Ma, S.; Li, R.; Lv, C.; Xu, W.; Gou, X. Facile synthesis of ZnO nanorod arrays and hierarchical nanostructures for photocatalysis and gas sensor applications. *Journal of Hazardous Materials* **2011**, *192*, 730–740.

(34) Zhou, L.; Wang, W.; Xu, H.; Sun, S.; Shang, M. Bi2O3 hierarchical nanostructures: Controllable synthesis, growth mechanism, and their application in photocatalysis. *Chemistry - A European Journal* **2009**, *15*, 1776–1782.

(35) Jiang, J.; Li, Y.; Liu, J.; Huang, X.; Yuan, C.; Lou, X. W. Recent advances in metal oxide-based electrode architecture design for electrochemical energy storage, 2012.

(36) Bierman, M. J.; Jin, S. Potential applications of hierarchical branching nanowires in solar energy conversion. *Energy & Environmental Science* **2009**, *2*, 1050.

(37) Huang, C. H.; Zhang, Q.; Chou, T. C.; Chen, C. M.; Su, D. S.; Doong, R. A. Three-dimensional hierarchically ordered porous carbons with partially graphitic nanostructures for electrochemical capacitive energy storage. *ChemSusChem* **2012**, *5*, 563–571.

(38) Li, Y.; Fu, Z. Y.; Su, B. L. Hierarchically structured porous materials for energy conversion and storage, 2012.

(39) Wang, J.; Lee, S.; Bielinski, A. R.; Meyer, K. A.; Dhyani, A.; Ortiz-Ortiz, A. M.; Tuteja, A.; Dasgupta, N. P. Rational Design of Transparent Nanowire Architectures with Tunable Geometries for Preventing Marine Fouling. *Advanced Materials Interfaces* **2020**, *7*, 2000672.

(40) Dumanli, A. G.; Savin, T. Recent advances in the biomimicry of structural colours. *Chemical Society Reviews* **2016**, *45*, 6698–6724.

(41) Saito, A.; Miyamura, Y.; Nakajima, M.; Ishikawa, Y.; Sogo, K.; Kuwahara, Y.; Hirai, Y. Reproduction of the Morpho blue by nanocasting lithography. *Journal of Vacuum Science & Technology B: Microelectronics and Nanometer Structures* **2006**, *24*, 3248.

(42) Zhang, W.; Gu, J.; Liu, Q.; Su, H.; Fan, T.; Zhang, D. Butterfly effects: novel functional materials inspired from the wings scales. *Physical Chemistry Chemical Physics* **2014**, *16*, 19767.

(43) Dasgupta, N. P.; Lee, H.-B.-R.; Bent, S. F.; Weiss, P. S. Recent Advances in Atomic Layer Deposition. *Chemistry of Materials* **2016**, *28*, 1943–1947.

(44) Elam, J. W.; Routkevitch, D.; Mardilovich, P. P.; George, S. M. Conformal coating on ultrahigh-aspect-ratio nanopores of anodic alumina by atomic layer deposition. *Chemistry of Materials* **2003**, *15*, 3507–3517.

(45) Atomic Layer Deposition (ALD) Equipment Market segment is estimated to grow at CAGR of 26.3% due to varied applications, High growth opportunities with Top Countries Data and Forecast to 2026 - MarketWatch.

(46) George, S. M. Atomic Layer Deposition: An Overview. *Chemical Reviews* **2010**, *110*, 111–131.

(47) Leskelä, M.; Ritala, M. In *Thin Solid Films*, Elsevier: 2002; Vol. 409, pp 138–146.

(48) Wiegand, C. W.; Faust, R.; Meinhardt, A.; Blick, R. H.; Zierold, R.; Nielsch, K. Understanding the Growth Mechanisms of Multilayered Systems in Atomic Layer Deposition Process. *Chemistry of Materials* **2018**, *30*, 1971–1979.

(49) Puurunen, R. L.; Vandervorst, W. Island growth as a growth mode in atomic layer deposition: A phenomenological model. *Journal of Applied Physics* **2004**, *96*, 7686–7695.

(50) Baji, Z.; Lábadi, Z.; Horváth, Z. E.; Molnár, G.; Volk, J.; Bársony, I.; Barna, P. Nucleation and growth modes of ALD ZnO. *Crystal Growth and Design* **2012**, *12*, 5615–5620.

(51) Parmigiani, J. P.; Thouless, M. D. The roles of toughness and cohesive strength on crack deflection at interfaces. *Journal of the Mechanics and Physics of Solids* **2006**, *54*, 266–287.

(52) Martin, E.; Leguillon, D.; Lacroix, C. An energy criterion for the initiation of interface failure ahead of a matrix crack in brittle matrix composites. *Composite Interfaces* **2002**, *9*, 143–156.

(53) Zhang, S.; Liu, W.; Hao, L.; Jiao, W.; Yang, F.; Wang, R. Preparation of carbon nanotube/carbon fiber hybrid fiber by combining electrophoretic deposition and sizing process for enhancing interfacial strength in carbon fiber composites. *Composites Science and Technology* **2013**, *88*, 120–125.

(54) Montes-Morán, M. A.; Young, R. J. Raman spectroscopy study of HM carbon fibres: effect of plasma treatment on the interfacial properties of single fibre/epoxy composites. *Carbon* **2002**, *40*, 845–855.

(55) JONES, C. The chemistry of carbon fibre surfaces and its effect on interfacial phenomena in fibre/epoxy composites. *Composites Science and Technology* **1991**, *42*, 275–298.

(56) Nasser, J.; Lin, J.; Steinke, K.; Sodano, H. A. Enhanced interfacial strength of aramid fiber reinforced composites through adsorbed aramid nanofiber coatings. *Composites Science and Technology* **2019**, *174*, 125–133.

(57) Lin, T.; Kuo, B.; Shyu, S.; Hsiao, S. Improvement of the adhesion of Kevlar fiber to bismaleimide resin by surface chemical modification. *http://dx.doi.org/10.1163/156856199X00109* **2012**, *13*, 545–560.

(58) Proctor, A.; Sherwood, P. M. X-ray photoelectron spectroscopic studies of carbon fibre surfaces—II: The effect of electrochemical treatment. *Carbon* **1983**, *21*, 53–59.

(59) Ma, K.; Wang, B.; Chen, P.; Zhou, X. Plasma treatment of carbon fibers: Non-equilibrium dynamic adsorption and its effect on the mechanical properties of RTM fabricated composites. *Applied Surface Science* **2011**, *257*, 3824–3830.

(60) Donnet, J.; Brendle, M.; Dhami, T.; Bahl, O. Plasma treatment effect on the surface energy of carbon and carbon fibers. *Carbon* **1986**, *24*, 757–770.

(61) Sheu, G.; Shyu, S. Surface properties and interfacial adhesion studies of aramid fibres modified by gas plasmas. *Composites Science and Technology* **1994**, *52*, 489–497.

(62) Patterson, B. A.; Sodano, H. A. Enhanced Interfacial Strength and UV Shielding of Aramid Fiber Composites through ZnO Nanoparticle Sizing. *ACS Applied Materials and Interfaces* **2016**, *8*, 33963–33971.

(63) Tiwari, S.; Sharma, M.; Panier, S.; Mutel, B.; Mitschang, P.; Bijwe, J. Influence of cold remote nitrogen oxygen plasma treatment on carbon fabric and its composites with specialty polymers. *Journal of Materials Science* **2011**, *46*, 964–974.

(64) Pittman, C.; Jiang, W.; He, G.-R.; Gardner, S. Oxygen plasma and isobutylene plasma treatments of carbon fibers: Determination of surface functionality and effects on composite properties. *Carbon* **1998**, *36*, 25–37.

(65) Brown, J. R.; Chappell, P. J. C.; Mathys, Z. Plasma surface modification of advanced organic fibres. *Journal of Materials Science* **1991**, *26*, 4172–4178.

(66) BROWN, J. R.; MATHYS, Z. Plasma surface modification of advanced organic fibres: Part V Effects on the mechanical properties of aramid/phenolic composites. *Journal of Materials Science 1997 32:10* **1997**, *32*, 2599–2604.

(67) Tiwari, S.; Bijwe, J.; Panier, S. Tribological studies on polyetherimide composites based on carbon fabric with optimized oxidation treatment. *Wear* **2011**, *271*, 2252–2260.

(68) Li, G.; Zhang, C.; Wang, Y.; Li, P.; Yu, Y.; Jia, X.; Liu, H.; Yang, X.; Xue, Z.; Ryu, S. Interface correlation and toughness matching of phosphoric acid functionalized Kevlar fiber and epoxy matrix for filament winding composites. *Composites Science and Technology* **2008**, *68*, 3208–3214.

(69) Jang, J.; Yang, H. The effect of surface treatment on the performance improvement of carbon fiber/polybenzoxazine composites. *Journal of Materials Science 2000 35:9* **2000**, *35*, 2297–2303.

(70) Wu, Z.; Pittman, C. U.; Gardner, S. D. Nitric acid oxidation of carbon fibers and the effects of subsequent treatment in refluxing aqueous NaOH. *Carbon* **1995**, *33*, 597–605.

(71) Kozlowski, C.; Sherwood, P. M. A. X-ray photoelectron-spectroscopic studies of carbon-fibre surfaces. Part 5.—The effect of pH on surface oxidation. *Journal of the Chemical Society, Faraday Transactions 1: Physical Chemistry in Condensed Phases* **1985**, *81*, 2745.

(72) Mimeault, V. J. Carbon fiber composites: Effect of fiber oxidation on composite behavior. *Fibre Science and Technology* **1971**, *3*, 273–283.

(73) Wang, Z.; Huang, X.; Xian, G.; Li, H. Effects of surface treatment of carbon fiber: Tensile property, surface characteristics, and bonding to epoxy. *Polymer Composites* **2016**, *37*, 2921–2932.

(74) Wicks, B. J.; Coyle, R. A. Microstructural inhomogeneity in carbon fibres. *JOURNAL OF MATERIALS SCIENCE* **1976**, *11*, 376–383.

(75) Jones, F. R. A Review of Interphase Formation and Design in Fibre-Reinforced Composites. *Journal of Adhesion Science and Technology* **2010**, *24*, 171–202.

(76) Dai, Z.; Shi, F.; Zhang, B.; Li, M.; Zhang, Z. Erratum to "Effect of sizing on carbon fiber surface properties and fibers/epoxy interfacial adhesion" [Appl. Surf. Sci. 257 (2011) 6980–6985]. *Applied Surface Science* **2011**, *258*, 1894.

(77) Berg, J.; Jones, F. The role of sizing resins, coupling agents and their blends on the formation of the interphase in glass fibre composites. *Composites Part A: Applied Science and Manufacturing* **1998**, *29*, 1261–1272.

(78) Yuan, H.; Zhang, S.; Lu, C.; He, S.; An, F. Improved interfacial adhesion in carbon fiber/polyether sulfone composites through an organic solvent-free polyamic acid sizing. *Applied Surface Science* **2013**, *279*, 279–284.

(79) Gnädinger, F.; Middendorf, P.; Fox, B. Interfacial shear strength studies of experimental carbon fibres, novel thermosetting polyurethane and epoxy matrices and bespoke sizing agents. *Composites Science and Technology* **2016**, *133*, 104–110.

(80) Zhang, X.; Fan, X.; Yan, C.; Li, H.; Zhu, Y.; Li, X.; Yu, L. Interfacial microstructure and properties of carbon fiber composites modified with graphene oxide. *ACS Applied Materials and Interfaces* **2012**, *4*, 1543–1552.

(81) Tamrakar, S.; An, Q.; Thostenson, E. T.; Rider, A. N.; Haque, B. Z.; Gillespie, J. W. Tailoring Interfacial Properties by Controlling Carbon Nanotube Coating Thickness on Glass Fibers Using Electrophoretic Deposition. *ACS Applied Materials and Interfaces* **2016**, *8*, 1501–1510.

(82) Rider, A. N.; An, Q.; Brack, N.; Thostenson, E. T. A Comparison of Mechanical and Electrical Properties in Hierarchical Composites Prepared using Electrophoretic or Chemical Vapor Deposition of Carbon Nanotubes. *MRS Advances* **2016**, *1*, 785–790.

(83) Qian, H.; Bismarck, A.; Greenhalgh, E. S.; Kalinka, G.; Shaffer, M. S. Hierarchical composites reinforced with carbon nanotube grafted fibers: The potential assessed at the single fiber level. *Chemistry of Materials* **2008**, *20*, 1862–1869.

(84) Mogilevsky, P.; Boakye, E. E.; Key, T. S.; Parthasarathy, T. A.; Hay, R. S.; Cinibulk, M. K. In situ Y2Si2O7 coatings on SiC fibers: Thermodynamic analysis and processing. *Journal of the American Ceramic Society* **2019**, *102*, 167–177.

(85) Militzer, C.; Dill, P.; Goedel, W. A. Atomic layer deposition onto carbon fiber fabrics. *Journal of the American Ceramic Society* **2017**, *100*, 5409–5420.

(86) Daubert, J. S.; Mundy, J. Z.; Parsons, G. N. Kevlar-Based Supercapacitor Fibers with Conformal Pseudocapacitive Metal Oxide and Metal Formed by ALD. *Advanced Materials Interfaces* **2016**, *3*, 1600355.

(87) Gregorczyk, K. E.; Pickup, D. F.; Sanz, M. G.; Irakulis, I. A.; Rogero, C.; Knez, M. Tuning the Tensile Strength of Cellulose through Vapor-Phase Metalation. *Chemistry of Materials* **2015**, *27*, 181–188.

(88) Hyde, G. K.; Scarel, G.; Spagnola, J. C.; Peng, Q.; Lee, K.; Gong, B.; Roberts, K. G.; Roth, K. M.; Hanson, C. A.; Devine, C. K.; Stewart, S. M.; Hojo, D.; Na, J.-S.; Jur, J. S.; Parsons, G. N. Atomic Layer Deposition and Abrupt Wetting Transitions on Nonwoven Polypropylene and Woven Cotton Fabrics. *Langmuir* **2010**, *26*, 2550–2558.

(89) Jur, J. S.; Spagnola, J. C.; Lee, K.; Gong, B.; Peng, Q.; Parsons, G. N. Temperature-Dependent Subsurface Growth during Atomic Layer Deposition on Polypropylene and Cellulose Fibers. *Langmuir* **2010**, *26*, 8239–8244.

(90) Liang, X.; Yang, Y.; Lou, J.; Sheldon, B. W. The impact of core-shell nanotube structures on fracture in ceramic nanocomposites. *Acta Materialia* **2017**, *122*, 82–91.

(91) Vogel, S.; Dransfeld, C.; Fiedler, B.; Gobrecht, J. Protective effect of thin alumina layer on carbon fibre to preserve tensile strength during CNT growth by CVD. *16th European Conference on Composite Materials, ECCM 2014* **2014**, 22–26.

(92) Yamamoto, N.; Guzman de Villoria, R.; Wardle, B. L. Electrical and thermal property enhancement of fiber-reinforced polymer laminate composites through controlled implementation of multi-walled carbon nanotubes. *Composites Science and Technology* **2012**, *72*, 2009–2015.

(93) Lin, Y.; Shaffer, J. W.; Sodano, H. A. Electrolytic deposition of PZT on carbon fibers for fabricating multifunctional composites. *Smart Materials and Structures* **2010**, *19*, 124004.

(94) Lin, Y.; Sodano, H. A. Fabrication and Electromechanical Characterization of a Piezoelectric Structural Fiber for Multifunctional Composites. *Advanced Functional Materials* **2009**, *19*, 592–598.

(95) Rodríguez, R. E.; Agarwal, S. P.; An, S.; Kazyak, E.; Das, D.; Shang, W.; Skye, R.; Deng, T.; Dasgupta, N. P. Biotemplated Morpho Butterfly Wings for Tunable Structurally Colored Photocatalysts. *ACS Applied Materials and Interfaces* **2018**, *10*, 4614–4621.

(96) Miikkulainen, V.; Leskelä, M.; Ritala, M.; Puurunen, R. L. Crystallinity of inorganic films grown by atomic layer deposition: Overview and general trends. *Journal of Applied Physics* **2013**, *113*, 021301.

(97) Dasgupta, N. P.; Mack, J. F.; Langston, M. C.; Bousetta, A.; Prinz, F. B. Design of an atomic layer deposition reactor for hydrogen sulfide compatibility. *Review of Scientific Instruments* **2010**, *81*, 044102.

(98) Zeng, L.; Liu, X.; Chen, X.; Soutis, C. Surface Modification of Aramid Fibres with Graphene Oxide for Interface Improvement in Composites. *Applied Composite Materials* **2018**, *25*, 843–852.

(99) Ni, M.; Leung, M. K.; Leung, D. Y.; Sumathy, K. A review and recent developments in photocatalytic water-splitting using TiO2 for hydrogen production, 2007.

(100) Chong, M. N.; Jin, B.; Chow, C. W.; Saint, C. Recent developments in photocatalytic water treatment technology: A review, 2010.

(101) Fujishima, A.; Zhang, X.; Tryk, D. A. TiO2 photocatalysis and related surface phenomena, 2008.

(102) Carp, O.; Huisman, C. L.; Reller, A. Photoinduced reactivity of titanium dioxide, 2004.

(103) Katamreddy, R.; Omarjee, V.; Feist, B.; Dussarrat, C. Ti Source Precursors for Atomic Layer Deposition of TiO2, STO and BST. *ECS Transactions* **2019**, *16*, 113–122.

(104) Lim, G. T.; Kim, D. H. In *Thin Solid Films*, Elsevier: 2006; Vol. 498, pp 254–258.

(105) Reiners, M.; Xu, K.; Aslam, N.; Devi, A.; Waser, R.; Hoffmann-Eifert, S. Growth and crystallization of TiO2 thin films by atomic layer deposition using a novel amido guanidinate titanium source and tetrakis-dimethylamido-titanium. *Chemistry of Materials* **2013**, *25*, 2934–2943.

(106) Azpitarte, I.; Zuzuarregui, A.; Ablat, H.; Ruiz-Rubio, L.; López-Ortega, A.; Elliott, S. D.; Knez, M. Suppressing the Thermal and Ultraviolet Sensitivity of Kevlar by Infiltration and Hybridization with ZnO. *Chemistry of Materials* **2017**, *29*, 10068–10074.

(107) Sockalingam, S.; Nilakantan, G. Fiber-matrix interface characterization through the microbond test: A review. *International Journal of Aeronautical and Space Sciences* **2012**, *13*, 282–295.

(108) Nishikawa, M.; Okabe, T.; Hemmi, K.; Takeda, N. Micromechanical modeling of the microbond test to quantify the interfacial properties of fiber-reinforced composites. *International Journal of Solids and Structures* **2008**, *45*, 4098–4113.

(109) MILLER, B.; GAUR, U.; HIRT, D. Measurement and mechanical aspects of the microbond pull-out technique for obtaining fiber/resin interfacial shear strength. *Composites Science and Technology* **1991**, *42*, 207–219.

(110) Meretz, S.; Nowak, H.; Hampe, A.; Hinrichsen, G.; Schumacher, K.; Sernow, R. In *Interfacial Phenomena in Composite Materials '91*; Elsevier: 1991, pp 73–76.

(111) Wu, K.; Xu, Y.; Cheng, X. Simulation and analysis of single fiber pull-out tests through ANSYS and VC++. *International Journal of Advanced Manufacturing Technology* **2018**, *96*, 1591–1599.

(112) Feih, S.; Schwartz, P. FEM analysis and comparison of single fiber pull-out tests. *Advanced Composites Letters* **1997**, *6*, 99–102.

(113) KANG, S.; LEE, D.; CHOI, N. Fiber/epoxy interfacial shear strength measured by the microdroplet test. *Composites Science and Technology* **2009**, *69*, 245–251.

(114) Gu, X.; Young, R. J. Deformation Micromechanics in Model Carbon Fiber Reinforced Composites Part II: The Microbond Test. *Textile Research Journal* **1997**, *67*, 93–100.

(115) Day, R.; Rodrigez, J. Investigation of the micromechanics of the microbond test. *Composites Science and Technology* **1998**, *58*, 907–914.

(116) Zhandarov, S.; Mäder, E. Analysis of a pull-out test with real specimen geometry. Part I: Matrix droplet in the shape of a spherical segment. *Journal of Adhesion Science and Technology* **2013**, *27*, 430–465.

(117) Zhao, Q.; Qian, C. C.; Harper, L. T.; Warrior, N. A. Finite element study of the microdroplet test for interfacial shear strength: Effects of geometric parameters for a carbon fibre/epoxy system. *Journal of Composite Materials* **2018**, DOI: 10.1177/0021998317740943.

(118) Zhi, C.; Long, H.; Miao, M. Influence of microbond test parameters on interfacial shear strength of fiber reinforced polymer-matrix composites. *Composites Part A: Applied Science and Manufacturing* **2017**, *100*, 55–63.

(119) González, C.; Vilatela, J.; Molina-Aldareguía, J.; Lopes, C.; LLorca, J. Structural composites for multifunctional applications: Current challenges and future trends. *Progress in Materials Science* **2017**, *89*, 194–251.

(120) Xiao, Y.; Qiao, W.; Fukuda, H.; Hatta, H. The effect of embedded devices on structural integrity of composite laminates. *Composite Structures* **2016**, *153*, 21–29.

(121) Deka, B. K.; Hazarika, A.; Kim, J.; Park, Y.-B.; Park, H. W. Multifunctional CuO nanowire embodied structural supercapacitor based on woven carbon fiber/ionic liquid–polyester resin. *Composites Part A: Applied Science and Manufacturing* **2016**, *87*, 256–262.

(122) Wen, J.; Xia, Z.; Choy, F. Damage detection of carbon fiber reinforced polymer composites via electrical resistance measurement. *Composites Part B: Engineering* **2011**, *42*, 77–86.

(123) Alexopoulos, N.; Bartholome, C.; Poulin, P.; Marioli-Riga, Z. Structural health monitoring of glass fiber reinforced composites using embedded carbon nanotube (CNT) fibers. *Composites Science and Technology* **2010**, *70*, 260–271.

(124) Chung, D. D. L.; Wang, S. Carbon fiber polymer-matrix structural composite as a semiconductor and concept of optoelectronic and electronic devices made from it. *Smart Materials and Structures* **1999**, *8*, 161–166.

(125) Wu, J.; Chen, J.; Zhao, Y.; Liu, W.; Zhang, W. Effect of electrophoretic condition on the electromagnetic interference shielding performance of reduced graphene oxide-carbon fiber/epoxy resin composites. *Composites Part B: Engineering* **2016**, *105*, 167–175.

(126) Chen, J.; Wu, J.; Ge, H.; Zhao, D.; Liu, C.; Hong, X. Reduced graphene oxide deposited carbon fiber reinforced polymer composites for electromagnetic interference shielding. *Composites Part A: Applied Science and Manufacturing* **2016**, *82*, 141–150.

(127) BROWN, E.; WHITE, S.; SOTTOS, N. Retardation and repair of fatigue cracks in a microcapsule toughened epoxy composite—Part II: In situ self-healing. *Composites Science and Technology* **2005**, *65*, 2474–2480.

(128) Yin, T.; Rong, M. Z.; Zhang, M. Q.; Yang, G. C. Self-healing epoxy composites - Preparation and effect of the healant consisting of microencapsulated epoxy and latent curing agent. *Composites Science and Technology* **2007**, *67*, 201–212.

(129) Kessler, M.; Sottos, N.; White, S. Self-healing structural composite materials. *Composites Part A: Applied Science and Manufacturing* **2003**, *34*, 743–753.

(130) Vilatela, J. J.; Eder, D. Nanocarbon composites and hybrids in sustainability: A review, 2012.

(131) Zhang, D.; Ye, L.; Deng, S.; Zhang, J.; Tang, Y.; Chen, Y. CF/EP composite laminates with carbon black and copper chloride for improved electrical conductivity and interlaminar fracture toughness. *Composites Science and Technology* **2012**, *72*, 412–420.

(132) Gungor, S.; Bakis, C. E. Indentation damage detection in glass/epoxy composite laminates with electrically tailored conductive nanofiller. *Journal of Intelligent Material Systems and Structures* **2016**, *27*, 679–688.

(133) Müller, M.; Pötzsch, H.; Gohs, U.; Heinrich, G. Online Structural-Health Monitoring of Glass Fiber-Reinforced Thermoplastics Using Different Carbon Allotropes in the Interphase. *Materials* **2018**, *11*, 1075.

(134) Nasser, J.; Groo, L. A.; Zhang, L.; Sodano, H. Laser induced graphene fibers for multifunctional aramid fiber reinforced composite. *Carbon* **2020**, *158*, 146–156.

(135) Groo, L.; Nasser, J.; Inman, D.; Sodano, H. Laser induced graphene for in situ damage sensing in aramid fiber reinforced composites. *Composites Science and Technology* **2021**, *201*, 108541.

(136) Coleman, J. N.; Curran, S.; Dalton, A. B.; Davey, A. P.; McCarthy, B.; Blau, W.; Barklie, R. C. Percolation-dominated conductivity in a conjugated-polymer-carbon-nanotube composite. *Physical Review B* **1998**, *58*, R7492–R7495.

(137) Díez-Pascual, A. M.; Naffakh, M.; Marco, C.; Gómez-Fatou, M. A.; Ellis, G. J. Multiscale fiber-reinforced thermoplastic composites incorporating carbon nanotubes: A review. *Current Opinion in Solid State and Materials Science* **2014**, *18*, 62–80.

(138) Puch, F.; Hopmann, C. Morphology and tensile properties of unreinforced and short carbon fibre reinforced Nylon 6/multiwalled carbon nanotube-composites. *Polymer* **2014**, *55*, 3015–3025.

(139) Nguyen-Tran, H. D.; Hoang, V. T.; Do, V. T.; Chun, D. M.; Yum, Y. J. Effect of multiwalled carbon nanotubes on the mechanical properties of carbon fiber-reinforced polyamide-6/polypropylene composites for lightweight automotive parts. *Materials* **2018**, *11*, 429.

(140) Bai, J.; Allaoui, A. Effect of the length and the aggregate size of MWNTs on the improvement efficiency of the mechanical and electrical properties of nanocomposites—experimental investigation. *Composites Part A: Applied Science and Manufacturing* **2003**, *34*, 689–694.

(141) Sharma, S.; Lakkad, S. Effect of CNTs growth on carbon fibers on the tensile strength of CNTs grown carbon fiber-reinforced polymer matrix composites. *Composites Part A: Applied Science and Manufacturing* **2011**, *42*, 8–15.

(142) Sager, R. J.; Klein, P. J.; Lagoudas, D. C.; Zhang, Q.; Liu, J.; Dai, L.; Baur, J. W. Effect of carbon nanotubes on the interfacial shear strength of T650 carbon fiber in an epoxy matrix. *Composites Science and Technology* **2009**, *69*, 898–904.

(143) GARCIA, E.; WARDLE, B.; JOHNHART, A.; YAMAMOTO, N. Fabrication and multifunctional properties of a hybrid laminate with aligned carbon nanotubes grown In Situ. *Composites Science and Technology* **2008**, *68*, 2034–2041.

(144) Park, J. K.; Do, I. H.; Askeland, P.; Drzal, L. T. Electrodeposition of exfoliated graphite nanoplatelets onto carbon fibers and properties of their epoxy composites. *Composites Science and Technology* **2008**, *68*, 1734–1741.

(145) Rodríguez, R. E.; Cho, T. H.; Ravandi, M.; LePage, W. S.; Banu, M.; Thouless, M. D.; Dasgupta, N. P. In *Minerals, Metals and Materials Series*, Springer: 2020, pp 1513–1527.

(146) Xiao, X.; Cao, G.; Chen, F.; Tang, Y.; Liu, X.; Xu, W. Durable superhydrophobic wool fabrics coating with nanoscale Al2O3 layer by atomic layer deposition. *Applied Surface Science* **2015**, *349*, 876–879.

(147) Kim, G.-M.; Lee, S.-M.; Michler, G. H.; Roggendorf, H.; Gösele, U.; Knez, M. Nanostructured Pure Anatase Titania Tubes Replicated from Electrospun Polymer Fiber Templates by Atomic Layer Deposition. *Chemistry of Materials* **2008**, *20*, 3085–3091.

(148) Lee, S.-M.; Pippel, E.; Gosele, U.; Dresbach, C.; Qin, Y.; Chandran, C. V.; Brauniger, T.; Hause, G.; Knez, M. Greatly Increased Toughness of Infiltrated Spider Silk. *Science* **2009**, *324*, 488–492.

(149) Jur, J. S.; Sweet, W. J.; Oldham, C. J.; Parsons, G. N. Atomic Layer Deposition of Conductive Coatings on Cotton, Paper, and Synthetic Fibers: Conductivity Analysis and Functional Chemical Sensing Using "All-Fiber" Capacitors. *Advanced Functional Materials* **2011**, *21*, 1993–2002.

(150) Brozena, A. H.; Oldham, C. J.; Parsons, G. N. Atomic layer deposition on polymer fibers and fabrics for multifunctional and electronic textiles. *Journal of Vacuum Science & Technology A: Vacuum, Surfaces, and Films* **2016**, *34*, 010801.

(151) Mundy, J. Z.; Shafiefarhood, A.; Li, F.; Khan, S. A.; Parsons, G. N. Low temperature platinum atomic layer deposition on nylon-6 for highly conductive and cat-

alytic fiber mats. *Journal of Vacuum Science & Technology A: Vacuum, Surfaces, and Films* **2016**, *34*, 01A152.

(152) Senghor, F. D.; Wasselynck, G.; Bui, H. K.; Branchu, S.; Trichet, D.; Berthiau, G. Electrical Conductivity Tensor Modeling of Stratified Woven-Fabric Carbon Fiber Reinforced Polymer Composite Materials. *IEEE Transactions on Magnetics* **2017**, *53*, 1–4.

(153) Lu, L.; Xing, D.; Xie, Y.; Teh, K. S.; Zhang, B.; Chen, S.; Tang, Y. Electrical conductivity investigation of a nonwoven fabric composed of carbon fibers and polypropylene/polyethylene core/sheath bicomponent fibers. *Materials & Design* **2016**, *112*, 383–391.

(154) Banerjee, P.; Lee, W.-J.; Bae, K.-R.; Lee, S. B.; Rubloff, G. W. Structural, electrical, and optical properties of atomic layer deposition Al-doped ZnO films. *Journal of Applied Physics* **2010**, *108*, 043504.

(155) Dasgupta, N. P.; Neubert, S.; Lee, W.; Trejo, O.; Lee, J.-R.; Prinz, F. B. Atomic Layer Deposition of Al-doped ZnO Films: Effect of Grain Orientation on Conductivity. *Chemistry of Materials* **2010**, *22*, 4769–4775.

(156) Shah, M.; Chaudhary, V. In *IOP Conference Series: Materials Science and Engineering*, Institute of Physics Publishing: 2020; Vol. 872, p 012087.

(157) Miccoli, I.; Edler, F.; Pfnür, H.; Tegenkamp, C. The 100th anniversary of the four-point probe technique: the role of probe geometries in isotropic and anisotropic systems. *Journal of Physics: Condensed Matter* **2015**, *27*, 223201.

(158) Lord, J. D.; Roebuck, B.; Morrell, R.; Lube, T. 25 year perspective Aspects of strain and strength measurement in miniaturised testing for engineering metals and ceramics. *Materials Science and Technology* **2010**, *26*, 127–148.

(159) Bruno, L. Mechanical characterization of composite materials by optical techniques: A review. *Optics and Lasers in Engineering* **2018**, *104*, 192–203.

(160) Sause, M. G. R. In *Springer Series in Materials Science*; Springer Verlag: 2016; Vol. 242, pp 57–129.

(161) LePage, W.; Shaw, J.; Daly, S. Optimum Paint Sequence for Speckle Patterns in Digital Image Correlation. *Experimental Techniques* **2017**, *41*, 557–563.

(162) Andrianov, I. V.; Danishevs'kyy, V. V.; Kalamkarov, A. L. Analysis of the effective conductivity of composite materials in the entire range of volume fractions of inclusions up to the percolation threshold. *Composites Part B: Engineering* **2010**, *41*, 503–507.

(163) Haghgoo, M.; Ansari, R.; Hassanzadeh-Aghdam, M. Prediction of electrical conductivity of carbon fiber-carbon nanotube-reinforced polymer hybrid composites. *Composites Part B: Engineering* **2019**, *167*, 728–735.

(164) Pal, G.; Kumar, S. Multiscale modeling of effective electrical conductivity of short carbon fiber-carbon nanotube-polymer matrix hybrid composites. *Materials and Design* **2016**, *89*, 129–136.

(165) Haj-Ali, R.; Zemer, H.; El-Hajjar, R.; Aboudi, J. Piezoresistive fiber-reinforced composites: A coupled nonlinear micromechanical–microelectrical modeling approach. *International Journal of Solids and Structures* **2014**, *51*, 491–503.

(166) Hu, M.; Thouless, M.; Evans, A. The decohesion of thin films from brittle substrates. *Acta Metallurgica* **1988**, *36*, 1301–1307.

(167) Thouless, M. D. Crack Spacing in Brittle Films on Elastic Substrates. *Journal of the American Ceramic Society* **1990**, *73*, 2144–2146.

(168) Thouless, M.; Olsson, E.; Gupta, A. Cracking of brittle films on elastic substrates. *Acta Metallurgica et Materialia* **1992**, *40*, 1287–1292.

(169) Tapily, K.; Gu, D.; Baumgart, H.; Namkoong, G.; Stegall, D.; Elmustafa, A. A. Mechanical and structural characterization of atomic layer deposition-based ZnO films. *Semiconductor Science and Technology* **2011**, *26*, 115005–115012.

(170) Vukusic, P.; Sambles, J. R.; Lawrence, C. R.; Wootton, R. J. Quantified interference and diffraction in single Morpho butterfly scales. *Proceedings of the Royal Society B: Biological Sciences* **1999**, *266*, 1403–1411.

(171) Zhang, W.; Zhang, D.; Fan, T.; Gu, J.; Ding, J.; Wang, H.; Guo, Q.; Ogawa, H. Novel Photoanode Structure Templated from Butterfly Wing Scales. *Chemistry of Materials* **2009**, *21*, 33–40.

(172) Pris, A. D.; Utturkar, Y.; Surman, C.; Morris, W. G.; Vert, A.; Zalyubovskiy, S.; Deng, T.; Ghiradella, H. T.; Potyrailo, R. a. Towards high-speed imaging of infrared photons with bio-inspired nanoarchitectures. *Nature Photonics* **2012**, *6*, 564–564.

(173) Yin, C.; Zhu, S.; Chen, Z.; Zhang, W.; Gu, J.; Zhang, D. One step fabrication of C-doped BiVO4 with hierarchical structures for a high-performance photocatalyst under visible light irradiation. *J. Mater. Chem. A* **2013**, *1*, 8367–8378.

(174) Tan, Y.; Gu, J.; Zang, X.; Xu, W.; Shi, K.; Xu, L.; Zhang, D. Versatile fabrication of intact three-dimensional metallic butterfly wing scales with hierarchical sub-micrometer structures. *Angewandte Chemie - International Edition* **2011**, *50*, 8307–8311.

(175) Liu, C.; Dasgupta, N. P.; Yang, P. Semiconductor Nanowires for Artificial Photosynthesis. *Chemistry of Materials* **2014**, *26*, 415–422.

(176) Zhou, H.; Fan, T.; Zhang, D. Biotemplated materials for sustainable energy and environment: Current status and challenges. *ChemSusChem* **2011**, *4*, 1344–1387.

(177) Park, H. J.; Xu, T.; Lee, J. Y.; Ledbetter, A.; Guo, L. J. Photonic Color Filters Integrated with Organic Solar Cells for Energy Harvesting. *ACS Nano* **2011**, *5*, 7055–7060.

(178) Zhang, W.; Anaya, M.; Lozano, G.; Calvo, M. E.; Johnston, M. B.; Míguez, H.; Snaith, H. J. Highly Efficient Perovskite Solar Cells with Tunable Structural Color. *Nano Letters* **2015**, *15*, 1698–1702.

(179) Lee, K.-T.; Lee, J. Y.; Seo, S.; Guo, L. J. Colored ultrathin hybrid photovoltaics with high quantum efficiency. *Light: Science & Applications* **2014**, *3*, e215–e215.

(180) Zhang, L.; Knez, M., *Atomic Layer Deposition for Biomimicry*; Elsevier Inc.: 2013, pp 399–428.

(181) Knez, M.; Kadri, A.; Wege, C.; Gösele, U.; Jeske, H.; Nielsch, K. Atomic Layer Deposition on Biological Macromolecules: Metal Oxide Coating of Tobacco Mosaic Virus and Ferritin. *Nano Letters* **2006**, *6*, 1172–1177.

(182) Lu, Y.; Bangsaruntip, S.; Wang, X.; Zhang, L.; Nishi, Y.; Dai, H. DNA Functionalization of Carbon Nanotubes for Ultrathin Atomic Layer Deposition of High κ Dielectrics for Nanotube Transistors with 60 mV/Decade Switching. *Journal of the American Chemical Society* **2006**, *128*, 3518–3519.

(183) Han, T. H.; Moon, H.-S.; Hwang, J. O.; Seok, S. I.; Im, S. H.; Kim, S. O. Peptide-templating dye-sensitized solar cells. *Nanotechnology* **2010**, *21*, 185601.

(184) Tang, X.; Francis, L. A.; Simonis, P.; Haslinger, M.; Delamare, R.; Deschaume, O.; Flandre, D.; Defrance, P.; Jonas, A. M.; Vigneron, J. P.; Raskin, J. P. Room temperature atomic layer deposition of Al ¡sub¿2¡/sub¿ O ¡sub¿3¡/sub¿ and replication of butterfly wings for photovoltaic application. *Journal of Vacuum Science & Technology A: Vacuum, Surfaces, and Films* **2012**, *30*, 01A146.

(185) Zhao, Y.; Wei, M.; Lu, J.; Wang, Z. L.; Duan, X. Biotemplated hierarchical nanostructure of layered double hydroxides with improved photocatalysis performance. *ACS Nano* **2009**, *3*, 4009–4016.

(186) Huang, J.; Wang, X.; Wang, Z. L. Controlled Replication of Butterfly Wings for Achieving Tunable Photonic Properties. *Nano Letters* **2006**, *6*, 2325–2331.

(187) Kolle, M.; Salgard-Cunha, P. M.; Scherer, M. R. J.; Huang, F.; Vukusic, P.; Mahajan, S.; Baumberg, J. J.; Steiner, U. Mimicking the colourful wing scale structure of the Papilio blumei butterfly. *Nature Nanotechnology* **2010**, *5*, 511–515.

(188) Liu, F.; Shi, W.; Hu, X.; Dong, B. Hybrid structures and optical effects in Morpho scales with thin and thick coatings using an atomic layer deposition method. *Optics Communications* **2013**, *291*, 416–423.

(189) Liu, F.; Liu, Y.; Huang, L.; Hu, X.; Dong, B.; Shi, W.; Xie, Y.; Ye, X. Replication of homologous optical and hydrophobic features by templating wings of butterflies Morpho menelaus. *Optics Communications* **2011**, *284*, 2376–2381.

(190) Gaillot, D. P.; Deparis, O.; Welch, V.; Wagner, B. K.; Vigneron, J. P.; Summers, C. J. Composite organic-inorganic butterfly scales: Production of photonic structures with atomic layer deposition. *Physical Review E* **2008**, *78*, 031922.

(191) Guziewicz, E.; Kowalik, I. A.; Godlewski, M.; Kopalko, K.; Osinniy, V.; Wójcik, A.; Yatsunenko, S.; Łusakowska, E.; Paszkowicz, W.; Guziewicz, M. Extremely low temperature growth of ZnO by atomic layer deposition. *Journal of Applied Physics* **2008**, *103*, 033515.

(192) Langston, M. C.; Dasgupta, N. P.; Jung, H. J.; Logar, M.; Huang, Y.; Sinclair, R.; Prinz, F. B. In Situ Cycle-by-Cycle Flash Annealing of Atomic Layer Deposited Materials. *The Journal of Physical Chemistry C* **2012**, *116*, 24177–24183.

(193) Kumar, M. K.; Krishnamoorthy, S.; Tan, L. K.; Chiam, S. Y.; Tripathy, S.; Gao, H. Field Effects in Plasmonic Photocatalyst by Precise SiO 2 Thickness Control Using Atomic Layer Deposition. *ACS Catalysis* **2011**, *1*, 300–308.

(194) Zhu, S.; Yao, F.; Yin, C.; Li, Y.; Peng, W.; Ma, J.; Zhang, D. Fe2O3/TiO2 photocatalyst of hierarchical structure for H2 production from water under visible light irradiation. *Microporous and Mesoporous Materials* **2014**, *190*, 10–16.

(195) Chen, J.; Su, H.; Song, F.; Moon, W.-J.; Kim, Y.-S.; Zhang, D. Bioinspired Au/TiO2 photocatalyst derived from butterfly wing (Papilio Paris). *Journal of Colloid and Interface Science* **2012**, *370*, 117–123.

(196) Fox, M. A.; Dulay, M. T. Heterogeneous photocatalysis. *Chemical Reviews* **1993**, *93*, 341–357.

(197) Zhang, D.; Zhang, W.; Gu, J.; Fan, T.; Liu, Q.; Su, H.; Zhu, S. Inspiration from butterfly and moth wing scales: Characterization, modeling, and fabrication. *Progress in Materials Science* **2015**, *68*, 67–96.

(198) Kisch, H.; Bahnemann, D. Best Practice in Photocatalysis: Comparing Rates or Apparent Quantum Yields? *The Journal of Physical Chemistry Letters* **2015**, *6*, 1907–1910.

(199) Houas, A. Photocatalytic degradation pathway of methylene blue in water. *Applied Catalysis B: Environmental* **2001**, *31*, 145–157.

(200) Murphy, W.; Veerkamp, T.; Leland, T. Effect of ultraviolet radiation on zinc oxide catalysts. *Journal of Catalysis* **1976**, *43*, 304–321.

(201) Bielinski, A. R.; Gayle, A. J.; Lee, S.; Dasgupta, N. P. Geometric Optimization of Bismuth Vanadate Core–Shell Nanowire Photoanodes using Atomic Layer Deposition. *ACS Applied Materials & Interfaces* **2021**, DOI: 10.1021/ACSAMI.1C09236.

(202) Bledzki, A. K.; Gassan, J. Composites reinforced with cellulose based fibres, 1999.

(203) George, S. M.; Dameron, A. A.; Yoon, B. Surface chemistry for molecular layer deposition of organic and hybrid organic-inorganic polymers. *Accounts of Chemical Research* **2009**, *42*, 498–508.

(204) Sundberg, P.; Karppinen, M. Organic and inorganic-organic thin film structures by molecular layer deposition: A review, 2014.

(205) Yoon, B.; Lee, B. H.; George, S. M. Highly conductive and transparent hybrid organic-inorganic zincone thin films using atomic and molecular layer deposition. *Journal of Physical Chemistry C* **2012**, *116*, 24784–24791.

(206) Yoshikawa, H.; Adachi, S. Optical Constants of ZnO. *Japanese Journal of Applied Physics* **1997**, *36*, 6237–6243.